Ph.D. DISSERTATION

Nanostructured Heterojunction Photoelectrodes for Unassisted Photoelectrochemical Water Splitting

By

Jin Wook Yang

February 2023

DEPARTMENT OF MATERIALS SCIENCE AND ENGINEERING

COLLEGE OF ENGINEERING

SEOUL NATIONAL UNIVERSITY

Nanostructured Heterojunction Photoelectrodes for Unassisted Photoelectrochemical Water Splitting

Advisor: Prof. Ho Won Jang

by

Jin Wook Yang

A thesis submitted to the Graduate Faculty of Seoul National University in partial fulfillment of the requirements for the Degree of Doctor of Philosophy Department of Materials Science and Engineering

February 2023

Approved

By

Chairman of Advisory Committee: Jin Young Kim

Vice-Advisory Committee: Ho Won Jang

Advisory Committee: Hyejin Jang

Advisory Committee: Soo Young Kim

Advisory Committee: Sanghan Lee

Abstract

Hydrogen without carbon emission has been considered as an alternative fuel, and its demand is expected to increase as a future energy carrier. However, the present hydrogen is almost grey hydrogen, which releases CO_2 during production. So, for green hydrogen, renewable energy should be the energy source, and hydrogen production based on solar power with huge amounts has been actively studied. Photoelectrochemical water splitting has been regarded as a promising way to resolve the global energy crisis and environmental pollution.

Among the various materials for photoanodes, bismuth vanadate ($BiVO_4$) is promising material because of its suitable band edge position in that it has cathodic onset potential. However, $BiVO_4$ has a short hole diffusion length of 70 nm, which leads to charge recombination. Also, its sluggish kinetics causes photocorrosion by the hole accumulation at the surface. To overcome these drawbacks, the nanostructuring of photoanodes and the introduction of cocatalysts are necessary.

Silicon (Si) is also a promising candidate for solar hydrogen generation by water oxidation because of its multiple properties; the narrow bandgap

which can absorb a wide range of light, long carrier diffusion length to facilitate charge separation/transport, and earth-abundance. However, silicon has no catalytic activity, and its self-oxidation potential is relatively more negative than that of water oxidation potential, which leads to anodic corrosion in the electrolytes. Therefore, to address those challenges and utilize silicon as a highly efficient photoanode material, it is imperative to introduce oxygen evolution reaction catalysts and protection layers to prevent silicon corrosion.

In this respect, this doctoral dissertation proposes the utilization of bismuth vanadate and silicon as efficient water oxidation photoanodes by introducing nanostructure, heterojunction, and oxygen evolution cocatalysts. For unassisted solar water splitting, PV-PEC tandem cells comprising nanostructured heterojunction photoanodes and perovskite/Si solar cells are fabricated, and solar-to-hydrogen conversion efficiency is evaluated.

The first study reports the introduction of nanorod-type bottom layers maximizes the charge separation and PEC performances of $BiVO_4$. The optimal growth time of $BiVO_4$ tailors nanopores of $BiVO_4$ and mesopores of bottom layers. This vertical 1-d structure with a large specific surface area boosts the charge separation efficiency, and SnO_2 NRs are more beneficial to the effect than WO_3 NRs, according to the analysis of PL and UPS. The

synergistic effect on both surface structure and band structure makes BiVO$_4$/SnO$_2$ photoanode reach 84% of the theoretical photocurrent density (6.31 mA cm^{-2} at 1.23 V versus RHE), exhibiting near-complete charge separation efficiency of 97%. Upon loading NiFe OEC, the photoanode generates a high photocurrent density of 5.61 mA cm^{-2} at 1.23 V versus RHE in water oxidation without a hole scavenger. The PEC-PV tandem cell with NiFe/BiVO$_4$/SnO$_2$ photoanode and perovskite/Si tandem solar cell spontaneously causes water oxidation, delivering the operating photocurrent density of 5.90 mA cm^{-2} and STH conversion efficiency of 7.3% in zero-bias. This study provides strategies to design high-performance photoanode and fosters the development of spontaneous solar water oxidation.

The second study focuses on a novel configuration of TANF/BiVO$_4$/In$_2$O$_3$ NRs as an archetype to boost photoelectrochemical performance by exploiting the synergistic combination of heterojunction construction and morphology modification. It is discovered that the introduction of In$_2$O$_3$ NRs as the ETL creates an optimized type II heterojunction with BiVO$_4$, which enhances charge separation by enabling favorable electron transport and hole blocking. Also, the architectures of BiVO$_4$, such as nanodot structure and core-shell structure on In$_2$O$_3$ NRs, have a significant impact on PEC performances. These two engineering strategies of heterostructure and

nanostructuring are supported by analysis for charge carrier dynamics such as M-S, ECSA, and TRPL. Furthermore, as an OEC, uniform coating with TANF on $BiVO_4$/In_2O_3 NRs improves charge injection and expedited OER kinetics. The bespoke TANF/$BiVO_4$/In_2O_3 NRs photoanodes show remarkable photocurrent densities of 7.1 mA cm^{-2} in sulfite oxidation and 4.2 mA cm^{-2} in water oxidation. Finally, the unbiased PV-PEC tandem cell comprising TANF/$BiVO_4$/In_2O_3 NRs photoanode and perovskite/Si solar cell generates the STH conversion efficiency of 6.2% without any external bias. This study will pave the way for the next generation of renewable energy applications.

The third study demonstrates the interface engineering of MIS photoanodes and investigates their PEC water and urea oxidation performances. First, different insulating SiO_x layers controlled by chemical etching methods ($SiO_{x,RCA}$, $SiO_{x,BOE}$) affect the surface status and interface properties, influencing the PEC performances. Second, it is discovered that composition control of metallic Ni_xFe_{1-x} thin films shows opposite properties with electrochemical properties and photoelectrochemical properties, where Ni-rich films show lower overpotentials for EC water oxidation. However, Fe-rich films show lower onset potentials for PEC water oxidation. There is a trade-off between the stability and the onset potentials depending on the

4

presence of Fe. The optimized $Ni_{0.5}Fe_{0.5}/SiO_x/n$-Si photoanodes show a high photocurrent density of 33.3 mA cm^{-2} at 1.23 V vs. RHE. By introducing additional $Ni(OH)_2$ catalysts on $Ni_{0.5}Fe_{0.5}/SiO_x/n$-Si photoanodes, enhanced fill factor over 25% and external quantum efficiency of 90% are achieved. By introducing the perovskite/Si tandem solar cell as a voltage supplier, the wired tandem cell device generates an operating photocurrent density of 8.8 mA cm^{-2}, corresponding to the STH conversion efficiency of 10.8%. Lastly, PEC urea oxidation properties of Si photoanodes are investigated. The heterogeneous $Ni(OH)_2/Ni_{0.5}Fe_{0.5}/SiO_x/n$-Si photoanode shows a highly active urea oxidation property, showing the potential of Si photoanodes for an additional utility of anodic reactions. This work suggests the design of efficient MIS photoanodes to produce hydrogen in polluted water.

This doctoral dissertation suggests promising pathways toward the design of efficient energy conversion devices. Various strategies, such as nanostructure, heterojunction, and introducing oxygen evolution cocatalysts, are applied to deal with the challenges of photoanode materials. These findings imply the possibility of developing a self-operating water splitting system and propose a direction toward maximizing solar-to-hydrogen conversion efficiency.

Student Number: 2018-29728

Jin Wook Yang

Table of Contents

List of Tables

List of Figures

15

Chapter 1

Photoelectrochemical Water Splitting

1.1. Hydrogen as a future energy carrier

The use of fossil fuels over the past 300 years has caused energy and environmental problems such as global warming and air pollution. The accumulative change was directly related to the surge of CO_2 emission, and the climate issue appears all over the world. So, for the carbon neutrality, hydrogen has been actively researched since zero carbon in combustion, easy to store and transport, and high energy density of 142 kJ/g, four times higher than gasoline and three times higher than natural gases [1-3]. In this flow, hydrogen that does not emit CO_2 is attracting attention as n alternative to fossil fuel, and its demand as a future energy carrier has been increased.

The hydrogen is classified into grey, blue, and green hydrogen according to the energy source and CO_2 emission in the production process. As shown in Figure 1.1, the grey hydrogen from reforming fossil fuel (natural gas) is generated along with CO_2. On the other hand, green hydrogen enables net
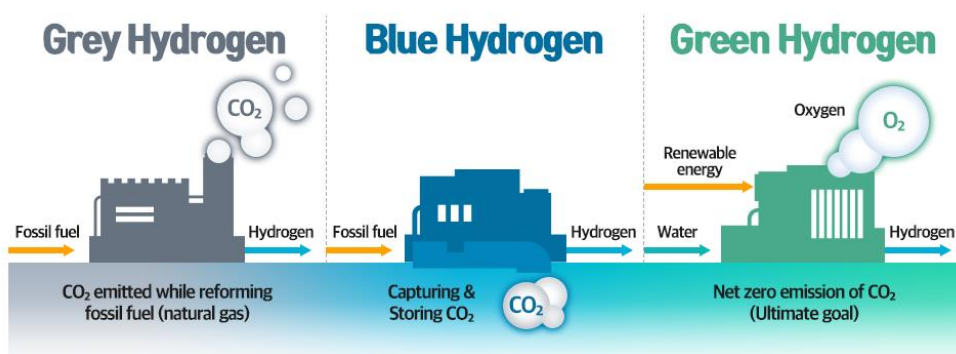
Figure 1.1 Grey hydrogen, blue hydrogen, and green hydrogen according to the energy source and CO2 emission in the production process.

zero emission of CO_2 by using renewable energy as an energy source. However, present hydrogen is almost grey hydrogen since 96% of feedstock are fossil fuels. So, for green hydrogen production, various renewable energy sources have been developed. Among them, the sun radiates a huge amount of energy, which is 9,600 times of the world energy consumption [4].

From the point of view of green hydrogen production, solar water splitting, which produces hydrogen by electrochemical reaction with solar energy, is the most ideal and sustainable method. As shown in Figure 1.2, there are three method of solar water splitting: photovoltaic (PV) – electrochemical (EC) method in which solar cells irradiated sunlight electrolyze water, photocatalyst (PC), and photoelectrode-based photoelectrochemical (PEC) method. In this respect, photoelectrochemical (PEC) water splitting, artificial photosynthesis, is a promising technology to convert solar energy into storable hydrogen energy without CO_2 emission. This doctoral dissertation mainly deals with PEC water splitting through engineering of various photoelectrodes.
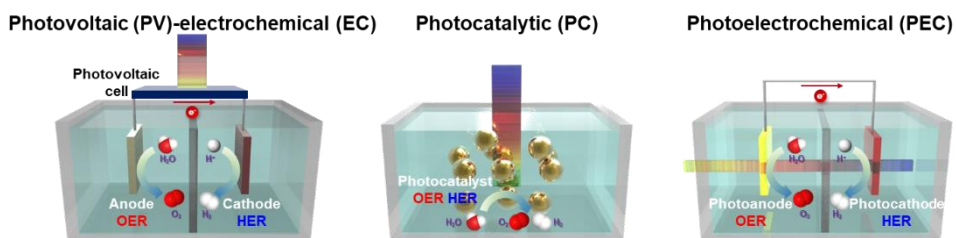
Figure 1.2 Three types of the solar water splitting.

1.2. Principles of PEC water splitting

To electrolyze water by solar energy, the photocathode for hydrogen evolution reaction (HER) or the photoanode for oxygen evolution reaction (OER) is necessary. In the view of thermodynamics of water splitting, the overall reaction is expressed as follows:

HER: $2H^+ + 2e^- \rightarrow H_2$ (g), $E^0_{red} = +0.00\ V_{NHE}$

OER: $2H_2O$ (l) $+ 4h^+ \rightarrow O_2(g) + 4H^+$, $E^0_{ox} = -1.23\ V_{NHE}$

Overall reaction: $2H_2O$ (l) $\rightarrow 2H_2(g) + O_2$ (g), $\Delta E^0_{cell} = -1.23\ V$
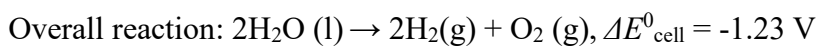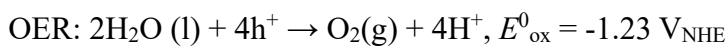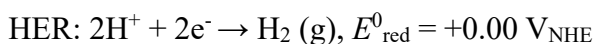
In the conversion of H_2O into H_2 and $1/2O_2$, Gibbs free energy change (ΔG) is 237.2 kJ mol^{-1}, and electrolysis voltage of 1.23 V is necessary. For the light absorption, the semiconductor having a band gap (E_g), which is energy difference between valence band maximum (VBM) and conduction band minimum (CBM). Band gap determines an absorbable wavelength range of sunlight. When the light is irradiated to the semiconductor, the electrons are excited from VBM to CBM, photo-generating electron-hole pairs. As shown in Figure 1.3, band gaps of various semiconductors determine the maximum absorption wavelength and the number of electron-hole pairs, resulting in different theoretical photocurrent density.
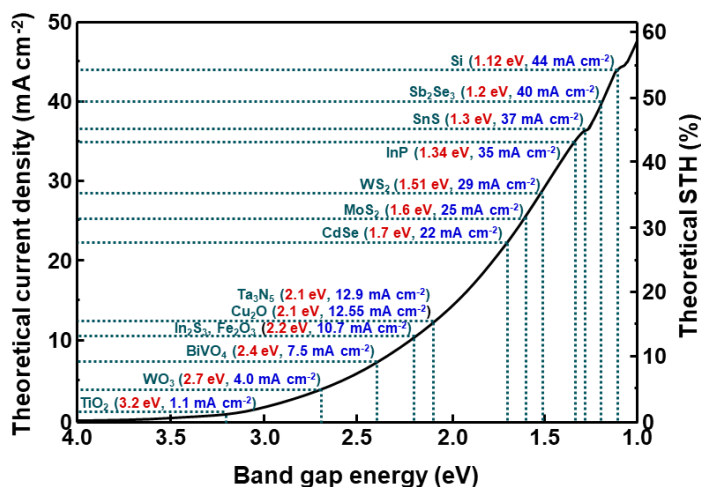
Figure 1.3 Theoretical photocurrent densities for semiconductors under one-sun illumination.

For single a single PEC system to generate HER and OER with single photoelectrode, CBM and VBM of photoelectrode must straddle the reduction potential (H^+/H_2) and oxidation potential (O_2/H_2O) of the water. Also, considering the kinetic overpotential at semiconductor/electrolyte interface, a band gap larger than the thermodynamic voltage of 1.23 V is required. However, there are few semiconductors that actually have a corresponding band edge position, and as the band gap increases, the absorption spectra decreases and the photocurrent decreases, so most studies have been focused on half-cell (photocathode/photoanode) development. In general, p-type semiconductor is used for photocathode, and n-type semiconductor is used for photoanode [5]. Since PEC water splitting reactions occur at the interface between photoelectrode and water, it is

23

important to understand a semiconductor-liquid (S-L) junction in the view of the energy diagram. Figure 1.4 shows the S-L junctions of n-type semiconductor for photoanode and p-type semiconduction for photocathode, respectively. In the case of photoanodes, electrons as the majority carrier move toward the electrolyte when n-type semiconductor contacts with the
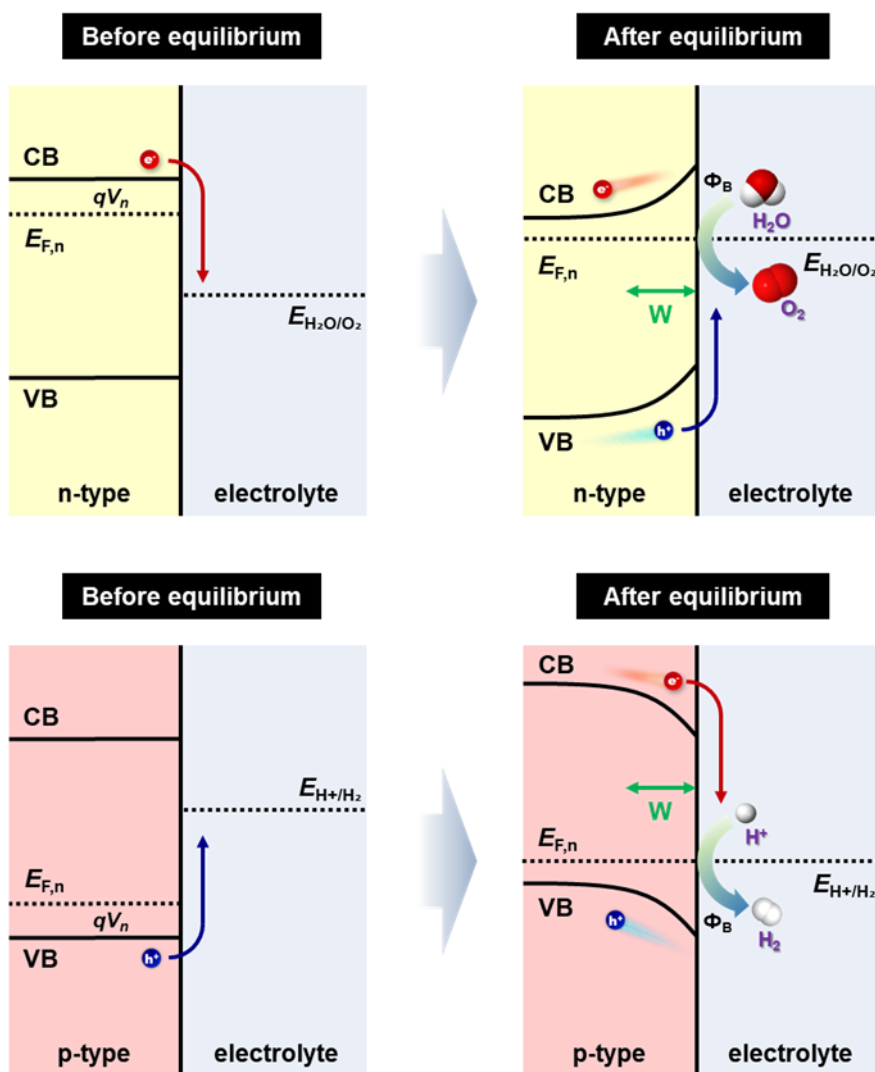
Figure 1.4 Semiconductor-liquid junction of photoanode and photocathode.

water. During the electron movement, the downward band bending occurs toward the interface. After the equilibrium state, the depletion region is formed, electrons are interrupted from the downward band bending toward the interface, and holes as minority carriers cause the water oxidation reaction [6]. On the contrary, holes as the majority carrier in the p-type semiconductors are injected into the water, forming the upward band bending toward the interface. After the equilibrium state, the depletion region is formed, the hole movement are suppressed from the upward band bending toward interfaces, and electrons as minority carriers participate in the water reduction [7]. Figure 1.5 summarizes the band edge positions of various n-type and p-type semiconductors. This doctoral dissertation mainly focusses on photoanodes for oxygen evolution reaction. Therefore, the following chapters will deal with the mechanism of PEC water splitting and materials selection in the view of photoanodes.
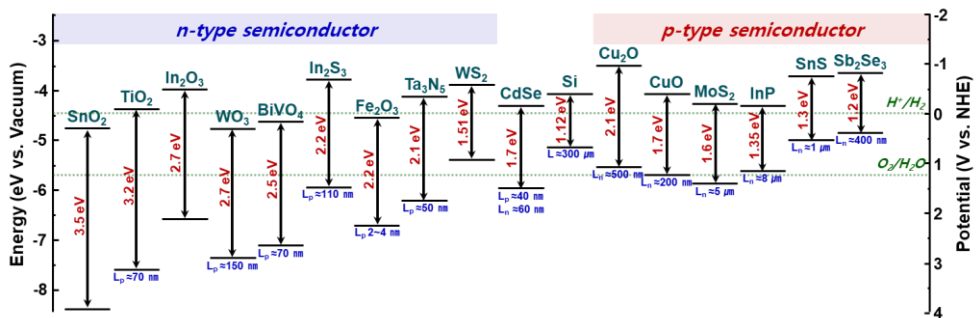
Figure 1.5 Band edge positions and carrier diffusion lengths of semiconductors.

1.3. Mechanisms of PEC water splitting (photoanode half cell)

Based on the understanding of the semiconductor-liquid junction, it is necessary to figure out the process by which a photoelectrode irradiated sunlight causes a water splitting reaction. The schematic in Figure 1.6 represents the details of the solar water splitting process in the view of the photoanode. The water splitting reaction proceeds three major physiochemical processes.

First, when the sunlight is irradiated into the n-type semiconductor, electron-hole pairs are photogenerated by absorbing the photons with energies larger than its band bap. The number of electron-hole pairs and theoretical photocurrent density are determined by the band gap of the material. When the photoanode is illuminated by sunlight, it becomes a non-
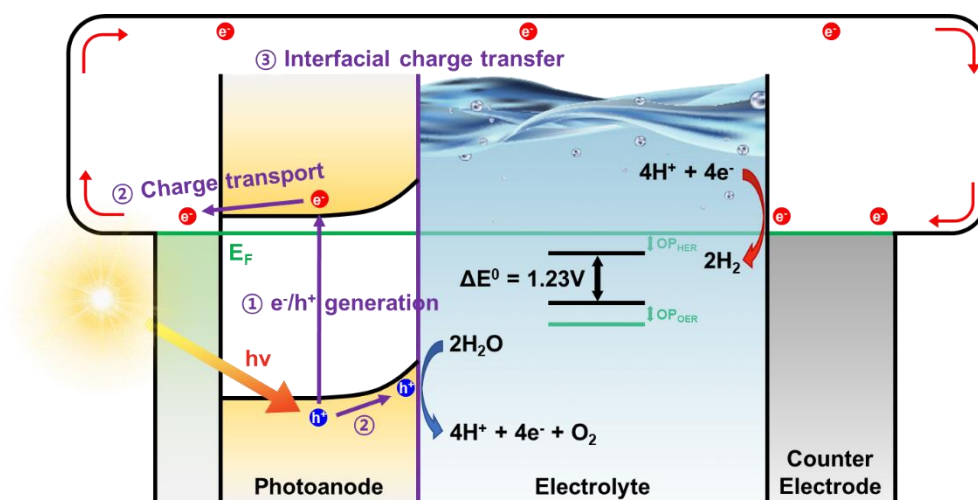
Figure 1.6 Schematic diagram of a simple PEC cell based on an n-type semiconducting photoanode electrically connected to a metal counter electrode.

equilibrium states according to the population change of electrons are holes, and quasi-Fermi levels are created. The quasi-Fermi level is indicative of the distribution of electron ($E_{F,n}$) and hole ($E_{F,p}$) under the non-equilibrium state. The quasi-Fermi level distribution induces an electric field near the semiconductor. The voltage generated by the built-in electric field of the semiconductor is called open-circuit voltage (V_{oc}) or photovoltage, which is the potential difference between $E_{F,n}$ and $E_{F,p}$. That is, the oxygen evolution reaction thermodynamically occurs at 1.23 V versus RHE, but the photovoltage of the photoanode pulls the reaction, and the performance of the photoanode are evaluated by photocurrent density at 1.23 V versus RHE. Absorption efficiency is affected by the surface morphology and reflectance, etc.

Second, photogenerated electron-hole pairs are separated. Electrons and holes are transported to electrical substrate and S-L interfaces, respectively. Charge separation efficiency is affected by the band bending, carrier mobility, and conductivity, etc. In particular, diffusion length, which determines carrier mobility, is a very important factor. The longer the diffusion length, the smaller the charge recombination and the larger the number of carriers participating in the water oxidation reaction (Figure 1.5).

Third, charge transfer reaction occurs at S-L interfaces. Holes as minority carriers of photoanode are injected into electrolyte, causing water oxidation. In this step, OER kinetics have a great influence on the water splitting performances. The surface states and corrosion level of photoanode are major factors determining the charge injection efficiency. In order to maximize the photoelectrochemical performances, various engineering strategies to lower the OER kinetic barrier are required.

The actual photocurrent density is expressed as the product of the theoretical photocurrent density and the three steps' efficiencies (absorption, separation, and injection efficiency). And, the limitation of the PEC system is low photocurrent density due to the drop of three steps' efficiency. Therefore, it is imperative to select the proper materials under the proper criteria and introduce promising engineering strategies to fabricate "efficient" photoanodes.

1.4. Unassisted PEC water splitting

Another limitation of PEC water splitting is the low photovoltage. In a single PEC system composed of one photoanode, the photovoltage is lower than the 1.23 V (+ overpotential) required for overall water splitting (Figure 1.7). It requires an additional external bias for water splitting, which is an nonspontaneous reaction. For unassisted water splitting that operates without external bias, it is necessary to introduce a tandem PEC system with two or more light absorbers. It includes PV-PEC tandem cell composed of photoanode and solar cell and PEC-PEC tandem cell comprising photoanode and photocathode. In these systems, the sum of the photovoltages of the two light absorbers is greater than 1.23 (+ overpotential), so they can be driven
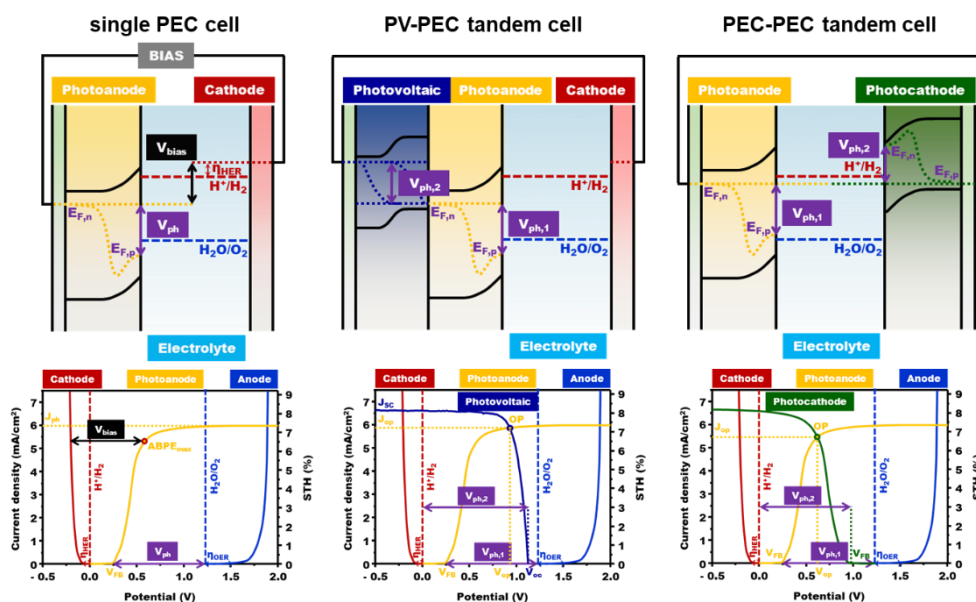
Figure 1.7 Schematics and *J-V* curves of single PEC cell, PV-PEC tandem cell, and PEC-PEC tandem cell.

without any external bias. Its solar-to-hydrogen (STH) conversion efficiency is calculated by multiplying the operating current density by 1.23 V. In this thesis, I mainly focus on the PV-PEC tandem cell.

The PV-PEC tandem cell is classified into mode T and mode P depending on the transmittance of the photoanode, as shown in Figure 1.8. In mode T, based on transparent photoanode materials (α-Fe$_2$O$_3$, BiVO$_4$, WO$_3$, TiO$_2$), short-wavelength-light is absorbed by the photoanode, and transmitted long-wavelength-light is absorbed by the solar cell. It has the principle in which the absorption wavelength ranges of the photoanode and solar cell are separated. And its operating current density is equal to the current density at the intersection of the solar cell and photoanode curves. In mode P, based on opaque photoanode materials (n-Si, Ta$_3$N$_5$), photoanode and solar cell side by side receive all wavelength light. It has the principle in which the absorption wavelength ranges of the photoanode and solar cell are separated. Here, instead of the wavelength range, the active area of light absorbers is halved. The operating current density is calculated by dividing the current density at the intersection by the active area ratio.

This doctoral thesis deals with an bismuth vanadate and n-type silicon as the photoanode material for mode T and mode P, respectively. In the

following chapter, the reasons for material selection according to physical properties and their advantages and drawbacks are discussed.
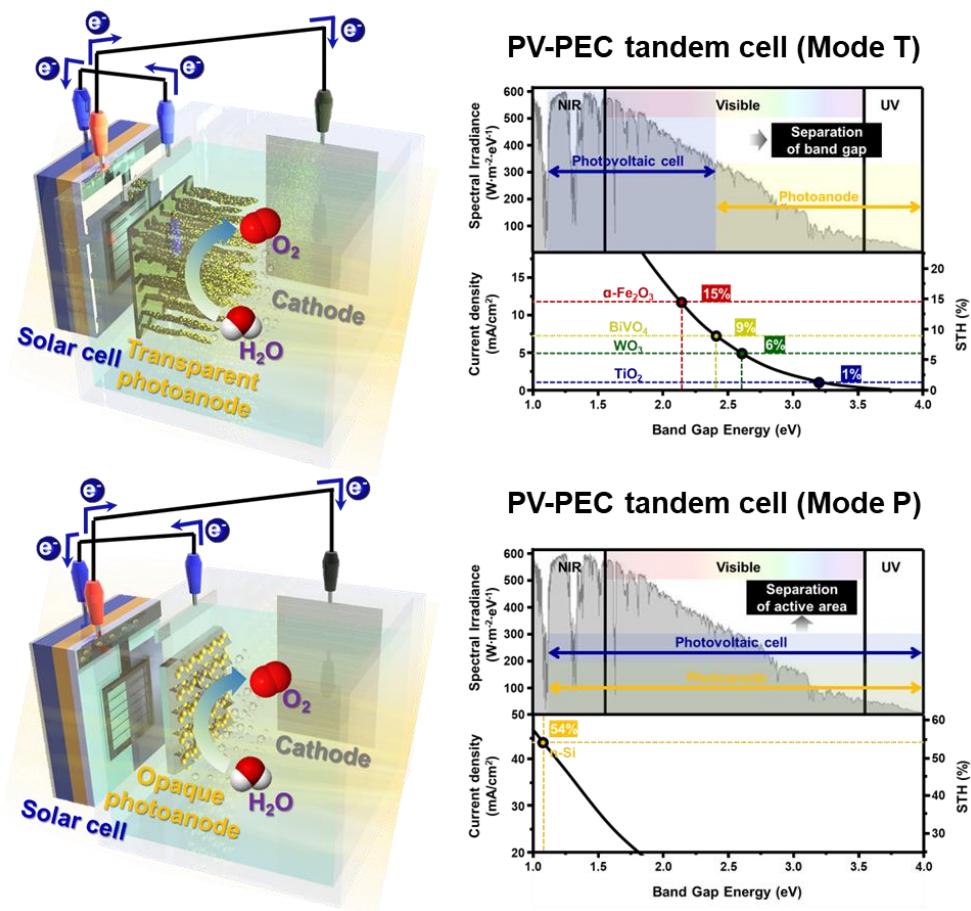
Figure 1.8 Schematics and absorption spectra of PV-PEC tandem cell (mode T, mode P).

1.5. Bismuth vanadate as a photoanode material

Bismuth vanadate (BiVO₄) is one of the most promising photoanode material because of its various characteristics. As shown in Figure 1.9, BiVO₄ has a moderate band gap of 2.4 eV, which corresponds a theoretical photocurrent density of 7.5 mA cm⁻². BiVO₄ has suitable band edge position for water oxidation, since its valence band edge is more positive than OER level. Also, its conduction band edge is relatively negative among various photoanode materials. It causes a more cathodic onset potential than other
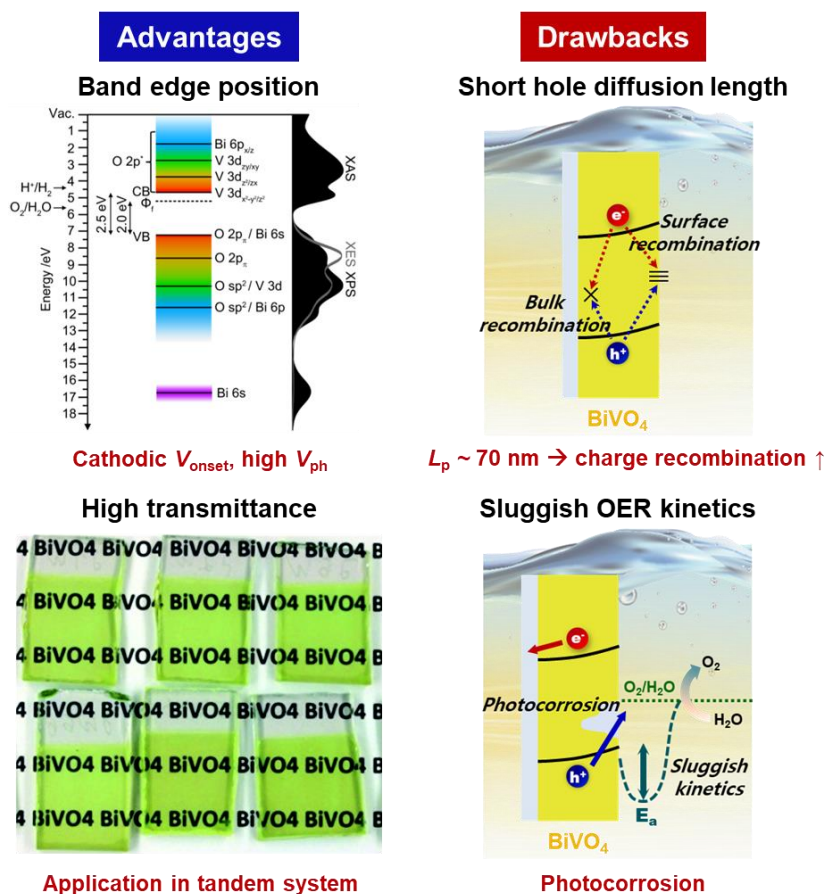
Figure 1.9 Advantages and drawbacks of BiVO₄.

materials. This makes it advantageous to construct tandem system due to the high photovoltage and low operating voltage. $BiVO_4$ also has high transmittance. So, it can be well applied to various mode T tandem devices. However, $BiVO_4$-based photoelectrodes have several issues to be solved to increase PEC performances. Since $BiVO_4$ has short hole diffusion length of 70 nm, generated charges are suffer from the bulk recombination and surface recombination [8]. It causes the reduction of charge separation efficiency. Also, $BiVO_4$ shows sluggish OER kinetics at the interface between photoelectrode and electrolyte. Holes reaching the surface cannot be injected to electrolytes and accumulated at the surface. The accumulated charges are used for self-oxidation of the photoanode, not water oxidation, a photocorrosion in which vanadium ions are eluted occurs. It reduces the stability of the $BiVO_4$-based photoanode [9]. Therefore, to address those challenges and fabricate highly efficient $BiVO_4$-based photoanodes, various strategies have been adjusted by numerous researchers.

1.6. Silicon as a photoanode material

Among many semiconducting materials, silicon is an attractive candidate for the photoelectrode because of its various characteristics. As shown in Figure 1.10, silicon has a narrow bandgap of 1.12 eV that can absorb a wide range of the solar spectrum from ultraviolet to near-infrared, resulting in high theoretical photocurrent density of 44 mA cm^{-2}. Even if the active area is reduced by half, it is advantageous to apply mode P tandem devices since it produces sufficient photocurrent density. Silicon also has a great carrier
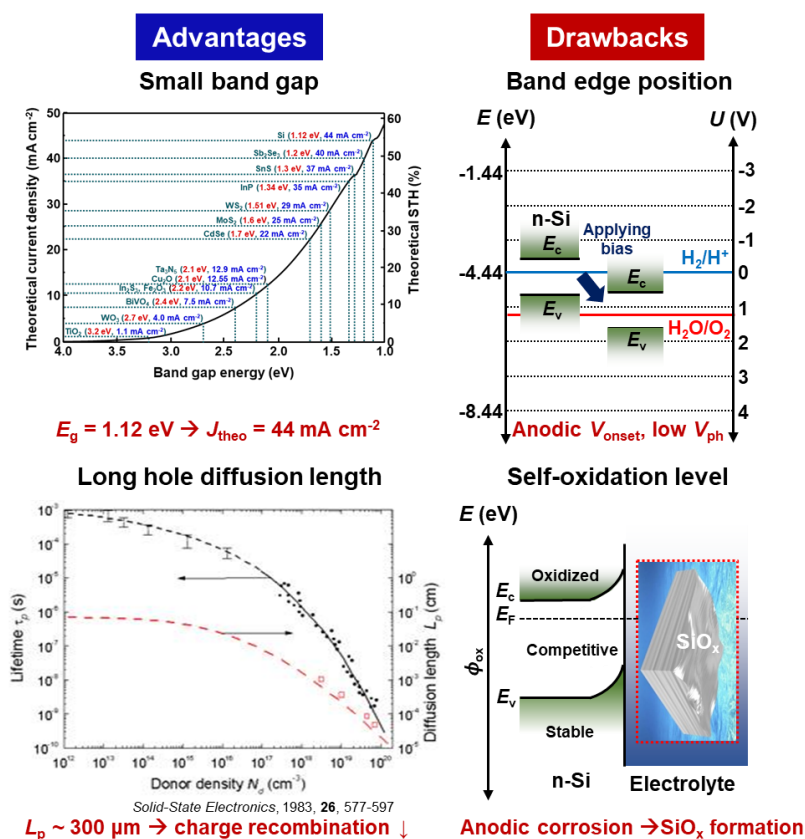
Figure 1.10 Advantages and drawbacks of n-Si.

mobility and high crystallinity [10]. Since it has very long hole diffusion length of 300 μm, less charge recombination evin in thin film structure without morphology engineering. However, developing silicon photoelectrodes is faced with the challenges to meet industrial needs for efficient hydrogen production. The representative drawbacks is silicon's unfavorable band position. The valence band edge position of silicon is quite negative than the oxygen evolution level. So, a large bias is required for the reaction, which appears as an anodic onset potential for OER. The instability of silicon in electrolytes is one of the most challenging issues for developing efficient Si-based photoanodes [11,12]. The self-oxidative level of silicon is also negative than the oxygen evolution level. Since an anodic corrosion occurs, insulating native silicon oxide are formed when exposed to the electrolyte, diminishing the charge transfer. Also, the Fermi level of silicon tends to be pinned, weakening band bending at the interfaces. Therefore, to address those challenges and fabricate highly efficient silicon-based photoanodes, various strategies have been adjusted by numerous researchers.

1.7. Reference

[1] Y. Yang, S. Niu, D. Han, T. Liu, G. Wang, Y. Li, *Adv. Energy Mater.*, **2017**, 7, 1700555.

[2] C. Jiang, S. J. A. Moniz, A. Wang, T. Zhang, J. Tang, *Chem. Soc. Rev.*, **2017**, 46, 4645.

[3] X. Li, J. Yu, J. Low, Y. Fang, J. Xiao, X. Chen, *J. Mater. Chem. A*, **2015**, 3, 2485.

[4] J. H. Kim, D. Hansora, P. Sharma, J. W. Jang, J. S. Lee, *Chem. Soc. Rev.*, **2019**, 48, 1908.

[5] M. G. Walter, E. L. Warren, J. R. KcKone, S. W. Boettcher, Q. Mi, E. A. Santori, N. S. Lewis, *Chem. Rev.*, **2010**, 110, 6446.

[6] M. Grätzel, *Nature*, **2001**, 414, 338.

[7] Z. Zhang, J. T. Yates, *Chem. Rev.*, **2012**, 112, 5520.

[8] K. T. Butler, B. J. Dringoli, L. Zhou, P. M. Rao, A. Walsh, L. V. Titova, *J. Mater. Chem. A*, **2016**, 4, 18516.

[9] Y. Ma, S. R. Pendlebury, A. Reynal, F. L. Formal, J. R. Durrant, *Chem. Sci.*, **2014**, 5, 2964.

[10] Z. Xing, F. Ren, H. Wu, L. Wu, X. Wang, J. Wang, D. Wan, G. Zhang, C. Jiang, *Sci. Rep.*, **2017**, 7, 43901.

[11] G. Loget, *Curr. Opin. Colloid Interface Sci.*, **2019**, 39, 40.

[12] J. Zhao, T. M. Gill, X. Zheng, *Nano Res.*, **2018**, 11, 3499.

Chapter 2

Near-Complete Charge Separation in Tailored BiVO$_4$-based

Heterostructure Photoanodes toward Artificial Leaf

2.1. Introduction

Photoelectrochemical (PEC) water splitting, which directly converts sunlight into hydrogen fuel, is one of the most sustainable solutions to stockpile solar energy. However, low solar-to-hydrogen (STH) conversion efficiency compared to its potential, has been a barrier to the commercialization, unlike a highly efficient photovoltaic (PV) system. The photovoltage generated by a single photoanode is insufficient to reach a required voltage (1.23 V + overpotential) for the water splitting reaction, resulting in a nonspontaneous reaction requiring external bias [1,2]. In this single absorber system, a trade-off between photovoltage generation and light absorption according to the bandgap limits improving PEC performances [3,4]. Thus, a tandem system consisting of dual absorbers with an optimal bandgap combination has been widely studied to maximize light harvesting by separating each absorption wavelength range [5–10]. A PEC-PV tandem system, especially, is favorable for spontaneous PEC water splitting in zero-bias due to the high STH conversion efficiency in terms of photovoltage production [2]. In this system, high photocurrent density in water oxidation of front photoanode is key to maximize the efficiency of the entire cell.

BiVO$_4$, which is one of the most promising photoanode materials, has a suitable band gap and band edge position for water oxidation, delivering a high theoretical photocurrent density of 7.5 mA cm^{-2} and STH conversion efficiency of 9.2% [11–13]. These PEC characteristics, however, markedly diminish under front-side illumination, and this issue hinders the implementation of PEC-PV tandem cell that requires high front PEC performance. Such a drawback is caused by the slow electron transport limiting the photocurrent generation of BiVO$_4$ [14,15]. Namely, the short carrier diffusion length (~70 nm) of BiVO$_4$ inhibits charge separation [16]. To enhance the charge separation efficiency of BiVO$_4$, two representative strategies are used; the first one is the nanostructuring of BiVO$_4$ [11,17,18]. Kim *et al.* fabricated a nanoporous BiVO$_4$ photoanode with charge separation efficiency of 90% [19], and Kuang *et al.* found an optimal average diameter (≈120 nm) of BiVO$_4$ to maximize PEC properties under front-side illumination [15]. The distance between the electrode inside and the electrolyte interface was structurally engineered as much the carrier diffusion length to make efficient charge transport without a reduction of light absorption. The second strategy is a heterojunction of BiVO$_4$ with bottom layer materials such as SnO$_2$ [20–23], WO$_3$ [24–29], and TiO$_2$ [30]. Lee *et al.* constructed a type II band structure by electrodepositing BiVO$_4$ on WO$_3$ nanorods (NRs) [24,25], and Baek *et al.* formed a ternary

heterojunction of $BiVO_4/WO_3/SnO_2$ film with charge separation efficiency of 93% [31]. These staggered band structures are energetically favorable for preventing charge recombination of $BiVO_4$. In this respect, the photoanode design for both surface structure and band structure is necessary to achieve higher front-side PEC performances. Another consideration to implement spontaneous solar water oxidation in zero-bias is the introducing PV cell, which serves a sufficient photovoltage with only light transmitted through the photoanode. A perovskite/Si tandem solar cell is suitable to obtain high STH conversion efficiency of PEC-PV tandem cell since it can supply high voltage by absorbing the light over 500 nm that $BiVO_4$ cannot absorb [32,33].

In this work, I demonstrate the charge separation of $BiVO_4$-based photoanode by evaluating front-side PEC performances with the introduction of bottom layers and implement spontaneous water oxidation in zero-bias by fabricating PEC-PV tandem cell. First, I design a new optimal surface structure, where nanopores of $BiVO_4$ and mesopores of nanorod-type bottom layers coexist by controlling the growth time of $BiVO_4$. Especially, the introduction of SnO_2 NRs makes the photoanode generate state-of-the-art photocurrent density of 6.31 mA cm^{-2} and charge separation efficiency of 97% at 1.23 V versus RHE. Systematic studies about charge carrier dynamics and band structures support the reason for high PEC

performances from a material point of view. I also explore NiFe oxygen evolution co-catalyst (OEC) for high photocurrent density in water oxidation (5.61 mA cm^{-2} at 1.23 V versus RHE). As an artificial leaf, I fabricate the PEC-PV tandem cell by combining a perovskite/Si tandem solar cell in the back of the NiFe/BiVO$_4$/SnO$_2$ photoanode. The artificial leaf causes spontaneous water oxidation with STH conversion efficiency of 7.3% in zero-bias, which is one of the best performance among previous reports about the BiVO$_4$-based tandem system.

2.2. Experimental procedures

2.2.1. Fabrication of SnO$_2$ and WO$_3$ nanorod arrays

Both SnO$_2$ and WO$_3$ NRs were formed by using GLAD through e-beam evaporation. The FTO glass substrate size was 1.5 cm × 1 cm, and the active region (1 cm × 1 cm) was adjusted with a shadow mask. The SnO$_2$ and WO$_3$ powder (Taewon Scientific Co., 99.99%) were placed in carbon crucibles and subjected e-beam evaporation. Prior to the fabrication of both SnO$_2$ and WO$_3$ NRs, a thin film (~ 50 nm) was deposited to improve the adhesion at 0° of glancing angle without rotation. Then, NRs were deposited at 85° of glancing angle with 80 rpm of rotation speed. To convert to crystalline phases, as-deposited SnO$_2$ samples were annealed in air at 550 °C for 2 h (2 °C min^{-1} of ramping rate), and WO$_3$ samples were annealed in air at 500 °C for 2 h (2 °C min^{-1} of ramping rate).

2.2.2. Electrochemical synthesis of BiVO₄

BiOI was electrodeposited on three different working electrodes (FTO, SnO₂ NRs/FTO, WO₃ NRs/FTO) in the three-electrode cell with Ag/AgCl (3 M NaCl) reference electrode and a mesh-type Pt counter electrode. The plating solution was based on 50 ml of an aqueous solution containing 400 mM KI (Daejung, 99.5%), 15 mM Bi(NO₃)₃·5H₂O (JUNSEI, 98%), 30 mM lactic acid (Sigma-Aldrich, 85%). The pH was adjusted to 1.8 by adding HNO₃ (JUNSEI, 60%) to dissolve the bismuth precursor. The 20 ml of ethanol (Daejung, 99.9%) containing 46 mM *p*-benzoquinone (JUNSEI, 98%) was slowly added to the aqueous solution. After the mixed solution was stirred for 30 min, the two-step electrodeposition was carried out. An initial deposition for 20 s was conducted at –0.35 V versus Ag/AgCl to make nucleation of BiOI, and the followed potential of –1.0 V versus Ag/AgCl was applied for growth. While the *p*-benzoquinone was reduced to hydroquinone in the process, the increased local pH at the working electrode causes the deposition of BiOI [11]. In addition, the lactic acid served to make the increase of the local pH more uniform by forming a lactate buffer [18]. To convert BiOI into BiVO₄, electrodes were annealed in air at 450 ℃ with a ramping rate of 2 ℃ min⁻¹ for 2 h after dropping the 0.05 ml of DMSO (Kanto, 98%) solution dissolving 200 mM VO(acac)₂ (Sigma-Aldrich, 98%). The as-annealed electrodes were soaked in a 1 M NaOH solution (Daejung,

2.2.2. Electrochemical synthesis of BiVO$_4$

BiOI was electrodeposited on three different working electrodes (FTO, SnO$_2$ NRs/FTO, WO$_3$ NRs/FTO) in the three-electrode cell with Ag/AgCl (3 M NaCl) reference electrode and a mesh-type Pt counter electrode. The plating solution was based on 50 ml of an aqueous solution containing 400 mM KI (Daejung, 99.5%), 15 mM Bi(NO$_3$)$_3$·5H$_2$O (JUNSEI, 98%), 30 mM lactic acid (Sigma-Aldrich, 85%). The pH was adjusted to 1.8 by adding HNO$_3$ (JUNSEI, 60%) to dissolve the bismuth precursor. The 20 ml of ethanol (Daejung, 99.9%) containing 46 mM *p*-benzoquinone (JUNSEI, 98%) was slowly added to the aqueous solution. After the mixed solution was stirred for 30 min, the two-step electrodeposition was carried out. An initial deposition for 20 s was conducted at –0.35 V versus Ag/AgCl to make nucleation of BiOI, and the followed potential of –1.0 V versus Ag/AgCl was applied for growth. While the *p*-benzoquinone was reduced to hydroquinone in the process, the increased local pH at the working electrode causes the deposition of BiOI [11]. In addition, the lactic acid served to make the increase of the local pH more uniform by forming a lactate buffer [18]. To convert BiOI into BiVO$_4$, electrodes were annealed in air at 450 ℃ with a ramping rate of 2 ℃ min^{-1} for 2 h after dropping the 0.05 ml of DMSO (Kanto, 98%) solution dissolving 200 mM VO(acac)$_2$ (Sigma-Aldrich, 98%). The as-annealed electrodes were soaked in a 1 M NaOH solution (Daejung,

99%) for 10 min with stirring for the removal of the excess V_2O_5. The electrodes were rinsed with deionized (DI) water and dried in air.

2.2.3. Deposition of NiFe co-catalyst on the BiVO$_4$/SnO$_2$ photoanode

NiFe OEC was deposited on the BiVO$_4$/SnO$_2$ electrode by using the e-beam evaporation. The active region (1 cm × 1 cm) of the BiVO$_4$/SnO$_2$ electrode was adjusted with a shadow mask. NiFe alloy pellets (50 wt% : 50 wt%) made by melting Ni pellets and Fe pellets (Taewon Scientific Co., 99.99%) in an arc furnace were placed in carbon crucibles and subjected e-beam evaporation. NiFe OEC (5-10 nm) was deposited with a deposition rate of 0.2 Å s^{-1} while maintaining an internal pressure of the chamber at 2.0 × 10^{-6} Torr.

2.2.4. Fabrication of monolithic perovskite/Si tandem solar cells

Double-polished n-type phosphor-doped Si wafers with 300 μm thickness prepared by a floating zone technique were cleaned using the RCA cleaning process after forming random pyramids at the rear-side. After immersed in a $HCl:H_2O_2$ and $H_2SO_4:H_2O_2$ solution to eliminate contaminants, the substrates were rinsed with DI water and dipped in the buffered oxide etching solution. Amorphous Si (a-Si) thin films were deposited using a plasma-enhanced chemical vapor deposition (PECVD) with a radio frequency of 13.56 MHz. a-Si:H films were doped by hydrogen-diluted PH_3 and B_2H_6 gases. A 20-nm-thick indium tin oxide (ITO) film was deposited as the recombination layer using radio frequency (RF) sputtering. After 80-nm-thick ITO film was deposited at the bottom of the Si cell, a 300-nm-thick Ag electrode was deposited using a thermal evaporator. Poly(triarylamine) (PTAA) solution was spin-coated on the ITO recombination layer at 6000 rpm for 25 s and annealed at 100 °C for 10 min. Perovskite solutions were prepared by dissolving formamidinium iodide (FAI), methylammonium bromide (MABr), CsI, PbI_2 (Alfa Aesar, 99.9985%), and $PbBr_2$ (Sigma-Aldrich, 99.999%), containing 2.5 mol% lead thiocyanate $(Pb(SCN)_2)$. In the mixed solvent system with *N,N*-dimethylformamide (DMF) and *N*-methyl-2-pyrrolidone (NMP), the stoichiometric $(FA_{0.65}MA_{0.20}Cs_{0.15})Pb(I_{0.8}Br_{0.15})_3$ was formed by adjusting their molar ratio.

46

To make a 2-d/3-d mixed perovskite solution, 1 mol% phenethylammonium iodide (PEAI) were added. The solution was spin-coated at 4000 rpm for 20 s on PTAA film, followed by immersing the spin-coated film in diethyl ether (DE) for 30 s. After annealing the film at 100 °C for 10 min, C_{60} layer was subsequently deposited by the thermal evaporator. A 0.2 wt% of polyethylenimine (PEIE, Sigma-Aldrich, 80% ethoxylated) solution in methanol was spin-coated at 6000 rpm for 30 s. ITO films were deposited on the C_{60}/PEIE layer using RF sputtering, and a 150 nm-thick Ag metal grid was deposited using a thermal evaporator on the ITO film.

2.2.5. Photoelectrochemical measurements

PEC measurements were carried out in three-electrode configuration using a potentiostat (Ivium-n-Stat, Ivium Technologies) with Ag/AgCl (Sat. KCl) reference electrode and the mesh-type Pt counter electrode. A Xe arc lamp (LS 150, Abet Technologies) was used as a light source, and the intensity of the solar simulator with AM 1.5G filter was calibrated to 1 sun (100 mW cm^{-2}) by using a reference photodiode (S300, McScience). All samples were measured under both front-side and back-side illumination conditions. Sulfite oxidation measurements were carried out in a 0.1 M K-P$_i$ buffer (pH 7.1) with 0.5 M Na$_2$SO$_3$ as a hole scavenger, and water oxidation measurements were carried out in a 1.0 M K-B$_i$ buffer (pH 9.5) without the hole scavenger. The measured potential ($E_{Ag/AgCl}$) versus Ag/AgCl reference electrode was converted to the reversible hydrogen electrode (RHE) by the Nernst equation:

$$E_{RHE} = E^{Ag/AgCl} + 0.059 \times pH + E^0_{Ag/AgCl}$$

, where E_{RHE} is the converted potential with RHE and $E^0_{Ag/AgCl} = 0.198$ V at 25 °C. For the *J-V* curves, the potential was swept toward an anodic direction with a scan rate of 20 mV s^{-1} under chopped illumination. The η_{sep} and η_{inj} values were calculated using the following equations:

$$J_{H_2O} = J_{abs} \times \eta_{sep} \times \eta_{inj}$$

$$J_{Na_2SO_3} = J_{abs} \times \eta_{sep}$$

, where J_{H_2O} and $J_{Na_2SO_3}$ are the observed photocurrent density in water oxidation and sulfite oxidation, respectively, and J_{abs} is the photocurrent density assuming that absorbed photons are wholly converted to the current. J_{abs} was derived by integrating the photon flux up to the wavelength (~ 525 nm) at which IPCE of BiVO₄ above zero is observed. The HC-STH was calculated based on J-V curves under non-chopped light using the following equation:

$$HC - STH\ (\%) = \frac{J_{ph}\ (1.23 - V_b)}{P_{in}}$$

, where J_{ph} is the observed photocurrent density, $P_{in} = 100$ mW cm⁻², and V_b is the applied potential versus RHE. The IPCE was measured using the light source with a monochromator at 1.23 V versus RHE. The EIS was recorded from 100 kHz to 0.1 Hz frequency with 10 mV of AC amplitude near the onset potential. The EIS data were fitted by the Z plot 2.x software. M-S measurement was conducted at 1 kHz frequency in the dark using the following equation:

$$C^{-2} = (2/\varepsilon\varepsilon_0 A^2 e N_D)[V - V_{FB} - (k_B T)/e]$$

, where C is the capacitance of the space charge layer, ε is the dielectric constant, ε_0 is the permittivity of vacuum (8.854×10^{-19} F m^{-1}), A is surface area, e is the electron charge (1.602×10^{-19} C), V is the applied potential versus RHE, V_{FB} is the flat band potential versus RHE, k_B is the Boltzmann constant (1.381×10^{-23} J K^{-1}), and T is the absolute temperature. The chronoamperometric curves were recorded at 1.23 V versus RHE. The Faradaic efficiency and oxygen evolution were calculated by the gas chromatography system (7890B, Agilent Technologies) in an air-tight cell at 1.23 V versus RHE.

2.2.6. PEC-PV tandem cell measurements

The PEC-PV tandem cell was fabricated by using NiFe/BiVO$_4$/SnO$_2$ photoanode and a perovskite/Si tandem solar cell as prepared. The *J-V* curve of the photoanode was recorded in a two-electrode configuration with the mesh-type Pt cathode in a 1.0 K-B$_i$ buffer (pH 9.5) under front-side 1 sun illumination (AM 1.5G). The *J-V* curve of the solar cell was measured behind the photoanode. After the photoanode was electrically connected by silver paste and copper sheet to the bottom electrode of the solar cell, the chronoamperometric measurement in zero-bias with the two-electrode system was carried out. The STH conversion efficiency of the PEC-PV tandem cell was calculated using the following equation:

$$STH\ (\%) = \frac{1.23 \times J_{op} \times \eta_F}{P_{in}} \times 100$$

, where J_{op} is the operating photocurrent density and η_F is the Faradaic efficiency.

2.2.7. Characterization

The crystal structure and phase of samples were identified by an XRD (D8 Advance, Bruker) with Cu Kα radiation. A field emission SEM (MERLIN Compact, JEISS) with an acceleration voltage of 5 kV and a working distance of 7 mm were employed to analyze the morphologies of $BiVO_4$-based photoanodes. HR-TEM images of $NiFe/BiVO_4/SnO_2$ photoanode were obtained using the TEM (JEM-2100F, JEOL) at an accelerating voltage of 200 kV, which was equipped with scanning TEM and EDS. UV-vis transmittance (T) and reflectance (R) spectra of the samples were recorded by a UV-vis spectrometer (Cary 5000, Agilent Technologies), and the absorption (A) was calculated from these measurements using the formula:

$$A = 100 - T - R$$

The absorption coefficient (α) was calculated using the formula:

$$\alpha = \frac{2.303 \times A}{100 \times t}$$

, where A is the absorption and t is a thickness of the sample. The Tauc plots for the calculation of direct bandgap (E_g) were fitted using the following equation:

$$\alpha h\nu = C(h\nu - E_g)^{1/2}$$

, where α is the absorption coefficient and C is a constant. The UPS were measured using X-ray photoelectron spectrometer (AXIS Nova, Kratos Analytical) with He I photon source of 21.22 eV. PL spectra were measured at room temperature on a fluorescence spectrophotometer (FlouTime 300, PicoQuant) with an excitation laser at 405 nm in the range from 405 nm to 700 nm. The TRPL was conducted at 550 nm.

2.3. Results and discussion

2.3.1. Materials synthesis and characterization

As shown in Figure 2.1(a), three $BiVO_4$-based photoanodes having different bottom layers were fabricated for the comparison of PEC properties. Among various metal oxide candidates, SnO_2 and WO_3 are representative materials that form a cascade type II band alignment with $BiVO_4$ [24]. For the property comparison of pristine $BiVO_4$ and heterostructure photoanodes, I introduced SnO_2 and WO_3 as the bottom layer. First, SnO_2 and WO_3 NRs were formed on the fluorine-doped tin oxide (FTO) by glancing angle
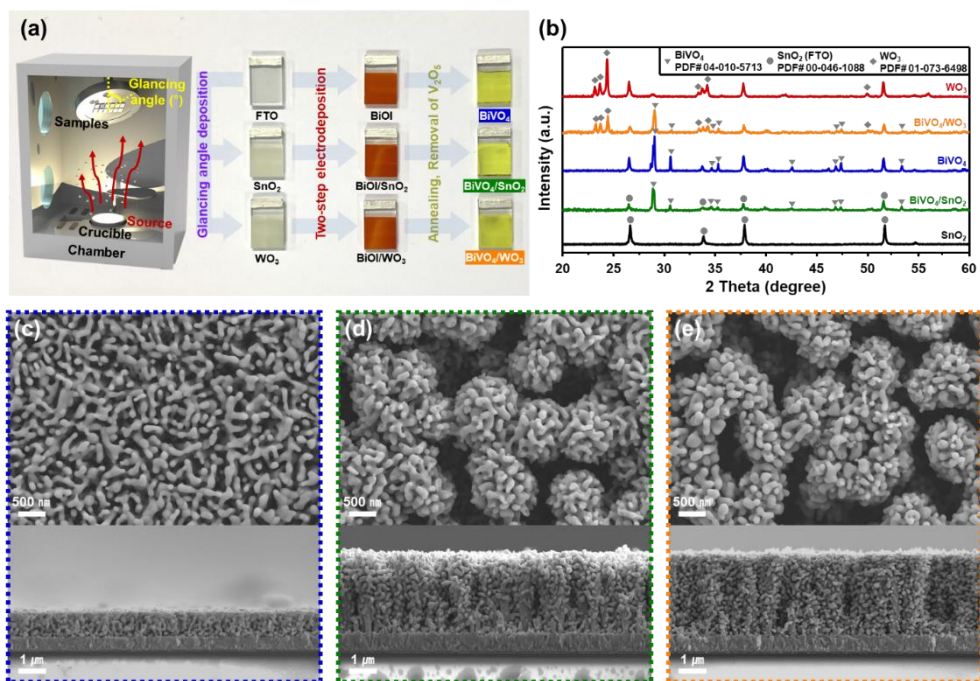
Figure 2.1 (a) Schematic of synthetic process and sample photograph. (b) XRD patterns of SnO_2, WO_3, $BiVO_4$, $BiVO_4/SnO_2$, and $BiVO_4/WO_3$. Top and cross-sectional SEM images of (c) $BiVO_4$, (d) $BiVO_4/SnO_2$, and (e) $BiVO_4/WO_3$.

deposition (GLAD) through e-beam evaporation. As the glancing angle increased, an average distance between the NRs increased from several nm to μm scale due to the shadowing effect [24]. I found an optimal glancing angle of 85° to well form several hundred nanometer-sized $BiVO_4$ between the NRs. After annealing for the crystallization, I confirmed both SnO_2 and WO_3 NRs with identical morphologies were well-formed with a length of 3 μm on the FTO, as shown in scanning electron microscopic (SEM) images (Figure 2.2(a)-(c)). The BiOI precursor was electrodeposited with a two-step (nucleation step and growth step) to make BiOI nanoplates more uniform and dense according to the reported method [18]. The higher deposition current of SnO_2 NRs and WO_3 NRs under the same potential, implies that the formation of NRs increased the specific surface area where BiOI can be generated (Figure 2.2(d)-(e)). As shown in Figure 2.2(f)-(h), BiOI nanoplates were uniformly formed throughout SnO_2 and WO_3 NRs, indicating that the NRs had adequate spacing for the formation of BiOI nanoplates. After annealing samples soaked by the V-based solution and removing the residual V_2O_5, I confirmed that $BiVO_4$, $BiVO_4/SnO_2$, and $BiVO_4/WO_3$ photoanodes were indexed to monoclinic $BiVO_4$ (PDF# 04-010-5713), tetragonal SnO_2 (PDF# 00-046-1088), and triclinic WO_3 (PDF# 01-073-6498) without impurities through X-ray diffraction (XRD) analysis (Figure 2.1(b)).

Top SEM images revealed that both nanopores and mesopores coexisted in BiVO$_4$/SnO$_2$ and BiVO$_4$/WO$_3$, whereas pristine BiVO$_4$ had only nanopores (Figure 2.1(c)-(e)). These mesopores formed by the NRs not only
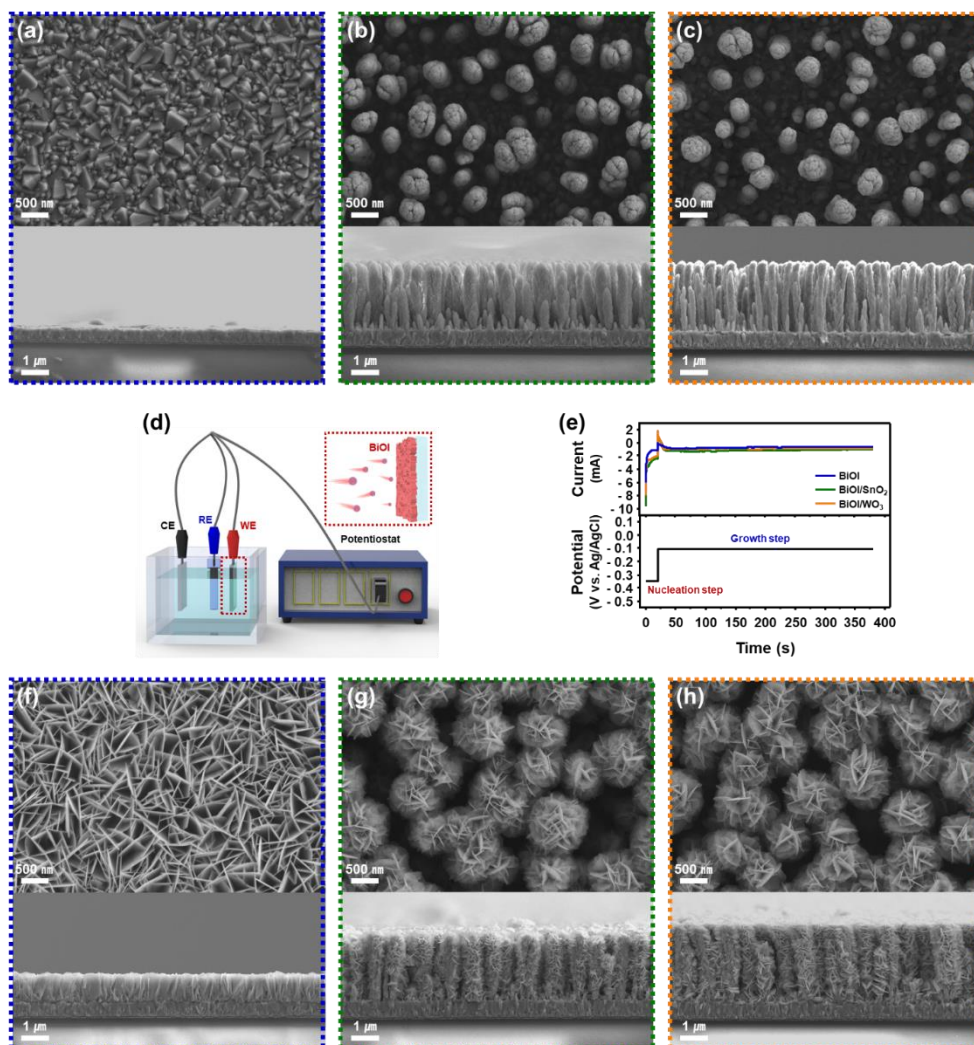
Figure 2.2 Top and cross-sectional SEM images of (a) fluorine-doped tin oxide (FTO), (b) SnO$_2$ NRs, and (c) WO$_3$ NRs. Schematic of the (d) two-step electrodeposition of BiOI in a three-electrode system. (e) Applied potential and current versus time graphs for two-step electrodeposition of BiOI, BiOI/SnO$_2$, and BiOI/WO$_3$. Top and cross-sectional SEM images of (f) BiOI, (g) BiOI/SnO$_2$, and (h) BiOI/WO$_3$.

allow the electrolyte to insert to the bottom of the photoanode better but also increase the specific surface area of the photoanode. Unlike pristine $BiVO_4$ with a thickness of 1 μm, $BiVO_4/SnO_2$ and $BiVO_4/WO_3$ had a vertical 1-dimensional (1-d) structure with a length of 3 μm, as shown in cross-sectional SEM images. The vertical 1-d structure acts as a path where photoelectrons generated from $BiVO_4$ exit to the back contact, also enhancing the light absorption by a light-trapping effect by scattered reflection [34]. To compare PEC properties by the amount of $BiVO_4$, three $BiVO_4$-based photoanode groups were synthesized with different growth times of BiOI, as shown in Figure 2.3. In the $BiVO_4$ group, the nanopore size of $BiVO_4$ increased as the growth time increased since BiOI grew
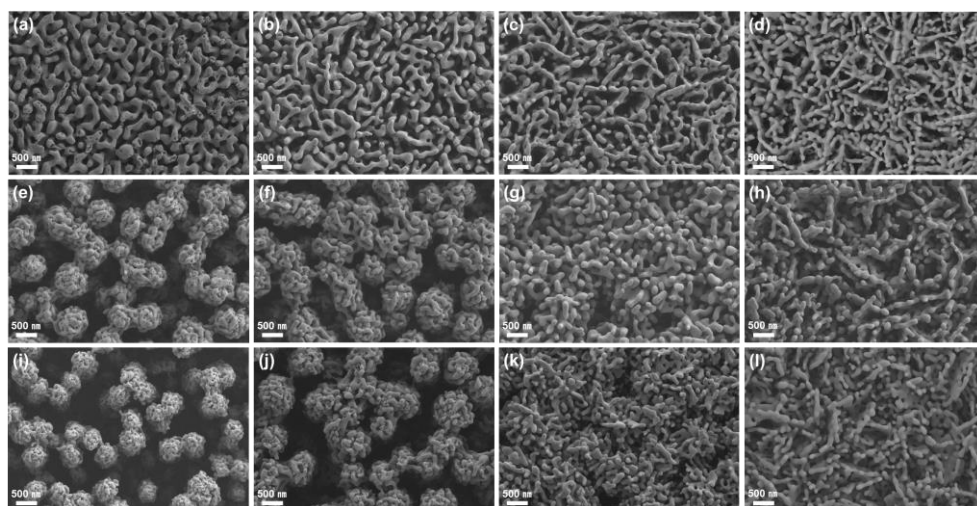
Figure 2.3 Top SEM images of $BiVO_4$ electrodeposited with growth time for (a) 180 s, (b) 360 s, (c) 540 s, and (d) 720 s. Top SEM images of $BiVO_4/SnO_2$ electrodeposited with growth time for (e) 180 s, (f) 360 s, (g) 540 s, and (h) 720 s. Top SEM images of $BiVO_4/WO_3$ electrodeposited with growth time for (i) 180 s, (j) 360 s, (k) 540 s, and (l) 720 s.

vertically from the FTO substrate. In the case of $BiVO_4/SnO_2$ and $BiVO_4/WO_3$ groups, however, the size of mesopores tended to decrease because BiOI grew from vertical NRs. After mesopores disappeared at the longer growth time, the nanopore size of $BiVO_4$ increased as in the $BiVO_4$ group.

I measured the linear sweep voltammetry (LSV) of three $BiVO_4$-based photoanode groups in a 0.1 M potassium phosphate (K-P_i) buffer (pH 7.1) with 0.5 M Na_2SO_3 under front-side and back-side 1 sun illumination (AM 1.5G). The photocurrent density versus applied potential (*J-V*) curves indicated the growth time of 360 s caused the highest photoactivity in all groups (Figure 2.4). As the growth time increased, the light absorption increased until the optimal time, but after $BiVO_4$ thickened and covered mesopores, the charge transport decreased, and benefits of the large specific surface area by mesopores disappeared. Interestingly, $BiVO_4$ photoanodes showed a higher photoactivity under back-side illumination, but $BiVO_4/SnO_2$ and $BiVO_4/WO_3$ photoanodes had higher photocurrent density at 1.23 V versus RHE under front-side illumination. This tendency shows that the introduction of SnO_2 and WO_3 bottom layers causes improvement in the electron transport of $BiVO_4$.
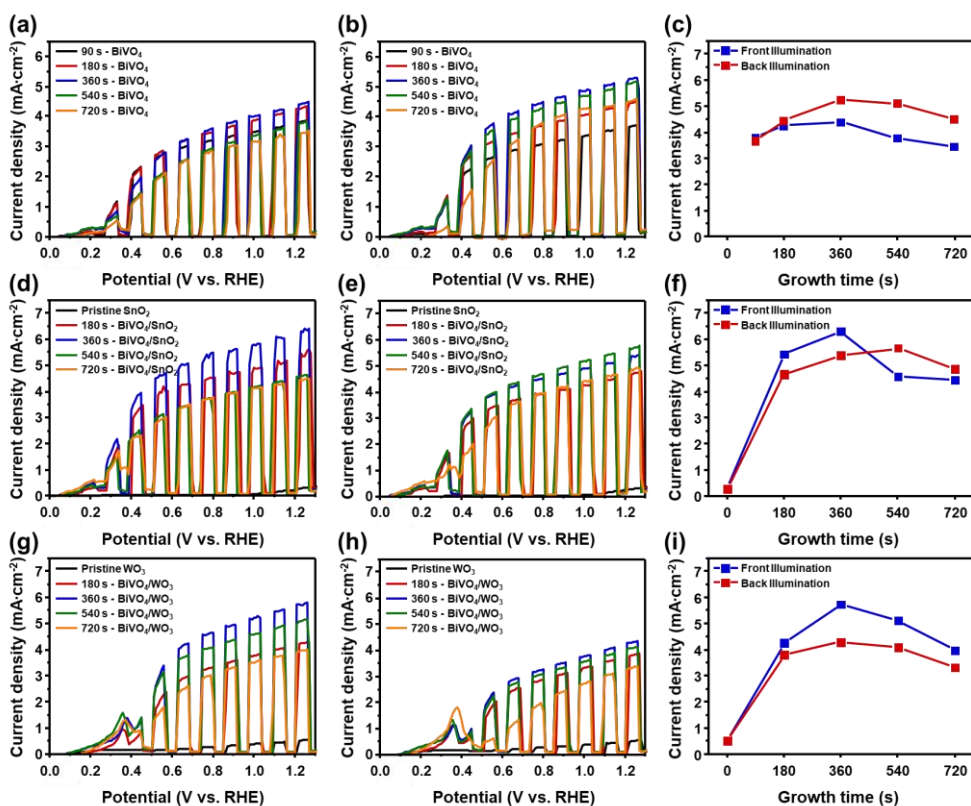
Figure 2.4 *J-V* curves under (a) front-side illumination and (b) back-side illumination and (c) photocurrent density at 1.23 V (versus RHE) of BiVO$_4$ with different growth time. *J-V* curves under (d) front-side illumination (e) and back-side illumination and (f) photocurrent density time at 1.23 V (versus RHE) of BiVO$_4$/SnO$_2$ with different growth time. *J-V* curves under (g) front-side illumination and (h) back-side illumination and (i) photocurrent density at 1.23 V (versus RHE) of BiVO$_4$/WO$_3$ with different growth time. All measurements were carried out in a 0.1 M potassium phosphate (K-P$_i$) buffer (pH 7.1) with 0.5 M Na$_2$SO$_3$ under front-side 1 sun illumination (AM 1.5G).

2.3.2. Photoelectrochemical performances and TEM analysis

PEC measurements of three $BiVO_4$-based photoanodes were conducted in a 0.1 M K-P_i buffer (pH 7.1) with 0.5 M Na_2SO_3 under front-side 1 sun illumination (AM 1.5G). The photocorrosion by sluggish oxygen evolution reaction (OER) kinetics of $BiVO_4$ causes performance degradation during measurements [35]. For the accurate comparison according to bottom layers, Na_2SO_3 was used as a hole scavenger preventing surface recombination [36]. As shown in *J-V* curves (Figure 2.5(a)), the photocurrent density of $BiVO_4$ at 1.23 V versus RHE was 4.39 mA cm^{-2}, $BiVO_4$/SnO_2 of 6.31 mA cm^{-2}, and $BiVO_4$/WO_3 of 5.72 mA cm^{-2}. The values of $BiVO_4$/SnO_2 and $BiVO_4$/WO_3 is an increase of 44% and 30%, respectively, compared to $BiVO_4$. To elucidate the enhancement of PEC performances, I calculated charge separation efficiency (η_{sep}) and charge injection efficiency (η_{inj}) at 1.23 V versus RHE, by measuring *J-V* curves for water oxidation in a 0.1 M K-P_i buffer without hole scavenger (Figure 2.6(a)). The water oxidation photocurrent density of $BiVO_4$ at 1.23 V versus RHE was 2.31 mA cm^{-2}, $BiVO_4$/SnO_2 of 3.19 mA cm^{-2}, and $BiVO_4$/WO_3 of 3.12 mA cm^{-2}. As shown in Figure 2.5(b), the η_{inj} values of $BiVO_4$ (~53%), $BiVO_4$/SnO_2 (~51%), and $BiVO_4$/WO_3 (~54%) were quite similar to each other since the ability to inject charges into the electrolyte is more dependent on the surface catalytic activity of $BiVO_4$ [31]. On the other hand, the η_{sep} value of $BiVO_4$/SnO_2

(~97%) was highest, compared with that of $BiVO_4$ (~68%) and $BiVO_4/WO_3$ (~88%). These results demonstrate that the difference of PEC characteristics originated from the charge separation at the interface between $BiVO_4$ and bottom layers. Besides, it was found that SnO_2 NRs are more effective in transporting electrons and holes of $BiVO_4$ than WO_3 NRs.
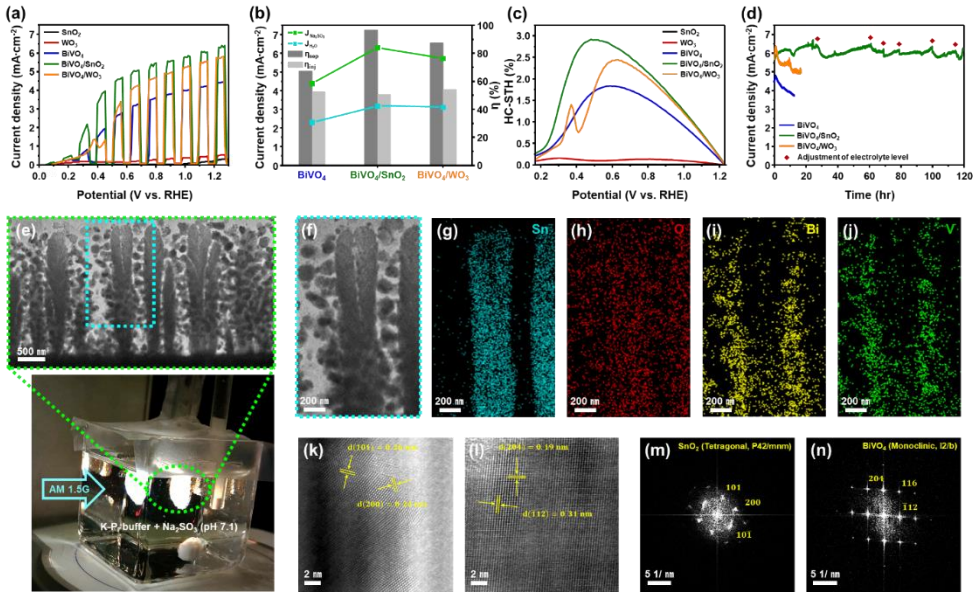
Figure 2.5 (a) Photocurrent density versus applied potential (*J-V*) curves of SnO_2, WO_3, $BiVO_4$, $BiVO_4/SnO_2$, and $BiVO_4/WO_3$ photoanodes. (b) Charge separation efficiencies (η_{sep}) and injection efficiencies (η_{inj}) of $BiVO_4$, $BiVO_4/SnO_2$, and $BiVO_4/WO_3$ photoanodes at 1.23 V (versus RHE). (c) Half-cell solar-to hydrogen conversion efficiency (HC-STH) curves of photoanodes. (d) Chronoamperometric curves of photoanodes at 1.23 V (versus RHE). All measurements were carried out in a 0.1 M potassium phosphate (K-P_i) buffer (pH 7.1) with 0.5 M Na_2SO_3 under front-side 1 sun illumination (AM 1.5G) (e) TEM image of $BiVO_4/SnO_2$ nanorod arrays. (f) Expanded TEM image of nanorod region. EDS mappings of (g) Sn, (h) O, (i) Bi, and (j) V. High-resolution TEM (HR-TEM) images of (k) tetragonal SnO_2 and (l) monoclinic $BiVO_4$. Fast Fourier transform (FFT) patterns of (m) tetragonal SnO_2 and (n) monoclinic $BiVO_4$.

As shown in Figure 2.5(c), I calculated the half-cell solar-to-hydrogen conversion efficiency (HC-STH) of BiVO$_4$ (1.85%), BiVO$_4$/SnO$_2$ (2.92%), and BiVO$_4$/WO$_3$ (2.45%), verifying the NRs played a major role in improving the light absorption and charge transport of BiVO$_4$. The oxidation
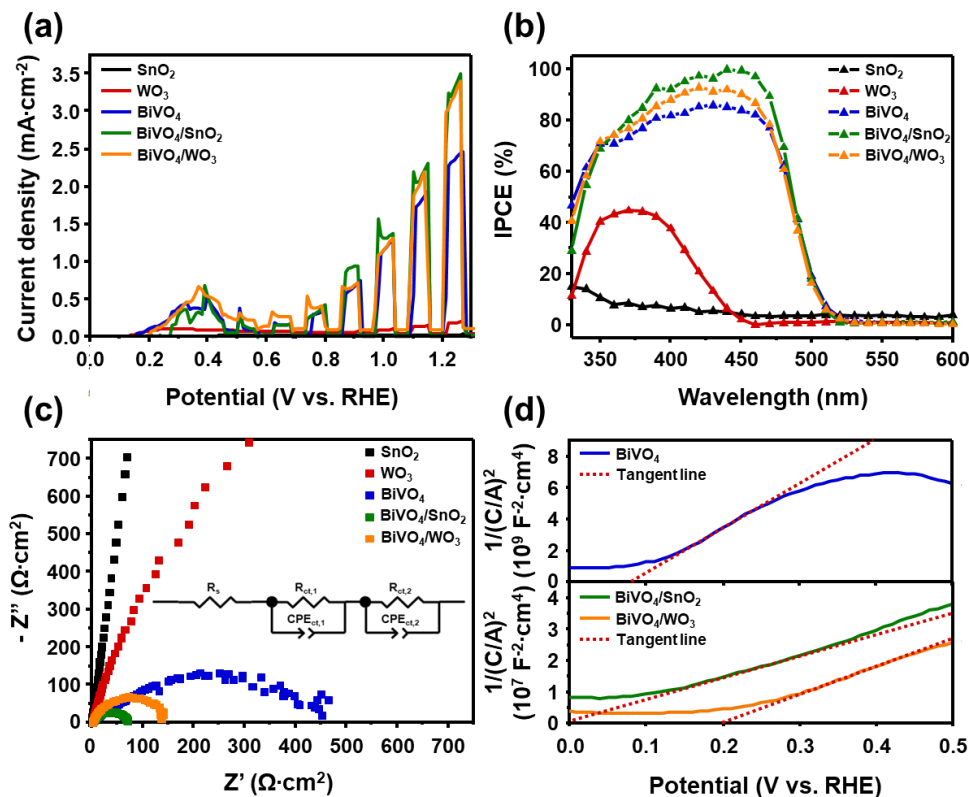
Figure 2.6 (a) *J-V* curves of SnO$_2$, WO$_3$, BiVO$_4$, BiVO$_4$/SnO$_2$, and BiVO$_4$/WO$_3$ photoanodes in a 0.1 M K-P$_i$ buffer (pH 7.1) without Na$_2$SO$_3$ under front-side 1 sun illumination (AM 1.5G). (b) IPCE spectra of SnO$_2$, WO$_3$, BiVO$_4$, BiVO$_4$/SnO$_2$, and BiVO$_4$/WO$_3$ photoanodes at 1.23 V (versus RHE) in a 0.1 M K-P$_i$ buffer (pH 7.1) with 0.5 M Na$_2$SO$_3$ under front-side 1 sun illumination (AM 1.5G). (c) EIS curves of SnO$_2$, WO$_3$, BiVO$_4$, BiVO$_4$/SnO$_2$, and BiVO$_4$/WO$_3$ photoanodes at 0.30 V (versus RHE) in a 0.1 M K-P$_i$ buffer (pH 7.1) with 0.5 M Na$_2$SO$_3$ under front-side 1 sun illumination (AM 1.5G). (d) Mott-Schottky (M-S) plots of BiVO$_4$, BiVO$_4$/SnO$_2$, and BiVO$_4$/WO$_3$ photoanodes in a 0.1 M K-P$_i$ buffer (pH 7.1) with 0.5 M Na$_2$SO$_3$.

62

of surface hydroxyl groups of WO_3 and water/hydroxide to peroxides caused the formation of peroxo-species, which appeared the residual peak near 0.4 V versus RHE in the $BiVO_4/WO_3$ photoanode [24]. The maximum HC-STH of $BiVO_4/SnO_2$ was obtained at a more cathodic applied potential compared to $BiVO_4/WO_3$, which represents, in the same surface structures, $BiVO_4/SnO_2$ shows better charge separation than $BiVO_4/WO_3$. For more investigation of the photoactivity of each photoanode, incident photon-to-current conversion efficiency (IPCE) was measured at 1.23 V versus RHE (Figure 2.6(b)). Compared with the pristine $BiVO_4$, the maximum IPCE of both $BiVO_4/SnO_2$ and $BiVO_4/WO_3$ exceeded 90% at a wavelength of up to 450 nm, showing a similar trend as the photocurrent density at 1.23 V versus RHE. To investigate the charge transfer dynamics of photoanodes, the electrochemical impedance spectroscopy (EIS) was performed at 0.30 V versus RHE, which is near the onset potential to exclude any possible complicated factors [37,38]. I obtained the series resistance (R_s) and charge transfer resistance ($R_{ct,1}$, $R_{ct,2}$) based on Nyquist plots and equivalent Randles circuit (Figure 2.6(c)). In Nyquist plots, the lower charge transfer resistance, the smaller size of the semicircle. As listed in Table 2.1, for the bulk resistance in the photoanode ($R_{ct,1}$), $BiVO_4/SnO_2$ had the lowest $R_{ct,1}$ of 69.48 Ω cm^2, compared to that of $BiVO_4$ (411.68 Ω cm^2) and $BiVO_4/WO_3$ (92.90 Ω cm^2). It can be said that the charge transport enhancement of $BiVO_4$

Table 2.1 Fitted series resistance (R_s) and charge transfer resistance ($R_{ct,1}$, $R_{ct,2}$) of photoanodes.

Photoanodes	R_s [Ω cm^2]	$R_{ct,1}$ [Ω cm^2]	$R_{ct,2}$ [Ω cm^2]
SnO$_2$	2.46	14136.80	5.07E11
WO$_3$	2.63	4183.80	207.98
BiVO$_4$	2.44	411.68	32.52
BiVO$_4$/SnO$_2$	2.55	69.48	39.47
BiVO$_4$/WO$_3$	2.55	92.90	46.88

by the introduction of the NRs suppressed the bulk charge recombination in the photoanode near the onset potential. Also, this effect is more efficient in SnO$_2$ NRs. On the other hand, for the interfacial resistance between photoanode and electrolyte ($R_{ct,2}$), the values of BiVO$_4$ (32.52 Ω cm^2), BiVO$_4$/SnO$_2$ (39.47 Ω cm^2), BiVO$_4$/WO$_3$ (46.88 Ω cm^2) did not show a significant difference. Because the outermost material of all three photoanodes is BiVO$_4$, the ability to inject holes at the photoanode/electrolyte interface is similar. These results are directly related that all three photoanodes have similar charge injection efficiency values (Figure 2.5(b)).

To investigate the flat band potential and donor concentration of each photoanode, Mott-Schottky (M-S) analysis was conducted at 1 kHz frequency in the dark. If some assumptions are fulfilled, the x-intercept of the tangent line (dashed line) in the M-S plot represents a flat band potential of the photoanode [25]. As shown in Figure 2.6(d), the flat band potential of $BiVO_4/SnO_2$ was near 0 V, and that of $BiVO_4/WO_3$ was 0.19 V, indicating the conduction band edge of $BiVO_4$ is more positive when forming a heterojunction with SnO_2 NRs than WO_3 NRs. The slopes of M-S plots for both $BiVO_4/SnO_2$ and $BiVO_4/WO_3$ were much flatter than that of $BiVO_4$, which represents that the donor concentration of $BiVO_4$ surges up when it forms a heterojunction with the bottom layer. It means that NRs prevent the charge recombination and strengthen the charge transport of $BiVO_4$. To figure out the photoanode generating the most stable photocurrent, the chronoamperometric curves were recorded at 1.23 V versus RHE (Figure 2.5(d)). Unlike $BiVO_4$ and $BiVO_4/WO_3$, which tended to decrease the photocurrent density after the start of the measurement, $BiVO_4/SnO_2$ showed highly stable PEC performance for 120 hours. SnO_2 NRs, which are more chemically stable in the electrolyte than WO_3 NRs, can continuously extract the electrons of $BiVO_4$ to the back contact. Also, the efficient charge separation at the interface between $BiVO_4$ and SnO_2 NRs (Figure 2.5(b)) enables the long-term photostability.

A transmission electron microscope (TEM) equipped with an energy dispersive spectroscope (EDS) was used to examine the detailed surface morphologies and elemental distributions of $BiVO_4/SnO_2$. The cross-sectional TEM image (Figure 2.5(e)) shows $BiVO_4$ uniformly covered SnO_2 nanorod arrays, maximizing the specific surface area. The expanded TEM image and EDS mapping of the NRs region (Figure 2.5(f)-(j)) reveal well-synthesized $BiVO_4$ around SnO_2 NRs without hindering the path of the electrolyte. $BiVO_4$ has a favorable size (<200 nm) in overcoming short hole diffusion length (~100 nm), and SnO_2 NRs with a length of 3 μm are suitable as electron paths. The high-resolution TEM (HR-TEM) image (Figure 2.5(k)) and fast Fourier transform (FFT) patterns (Figure 2.5(m)) of SnO_2 verify the crystalline tetragonal phase with d-spacings of 0.26 nm and 0.24 nm, corresponding to (101) and (200) planes, respectively. Also, the HR-TEM image (Figure 2.5(l)) and FFT patterns (Figure 2.5(n)) of $BiVO_4$ show the crystalline monoclinic phase with d-spacings of 0.19 nm and 0.31 nm, corresponding to (204) and (-112) planes, respectively. These results are well-matched with the XRD analysis and identify monoclinic $BiVO_4$ suitable for PEC water oxidation [14].

2.3.3. Studies of charge carrier dynamics and band structures

I employed the photoluminescence (PL) spectroscopy to further examine charge recombination behaviors of three $BiVO_4$-based photoanodes shown in the PEC characteristics. As a result of measuring steady-state PL spectra (Figure 2.7(a)), peaks were observed at 550 nm, which originates from radiative charge recombination [39]. $BiVO_4/SnO_2$ exhibited the lowest PL intensity by the increase of the PL quenching, implying that the adoption of SnO_2 NRs was effective in suppressing the charge recombination. As shown in Figure 2.7(b), a further study of the charge transport dynamics was conducted by the time-resolved photoluminescence (TRPL) analysis. TRPL
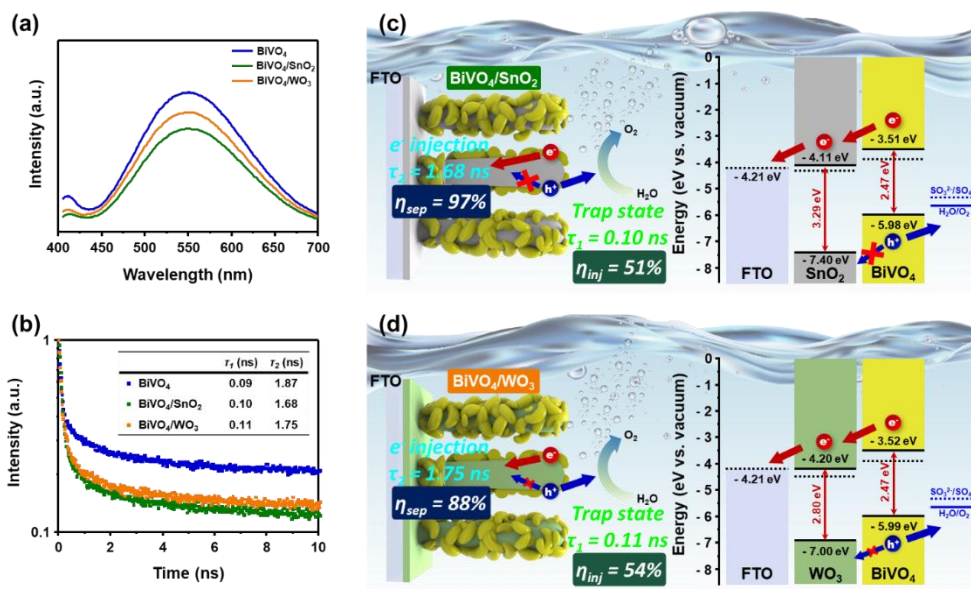
Figure 2.7 (a) Steady-state photoluminescence (PL) spectra and (b) time-resolved photoluminescence (TRPL) at 550 nm of $BiVO_4$, $BiVO_4/SnO_2$, $BiVO_4/WO_3$ photoanodes. Schematics of charge carrier dynamics and flat band structures of (c) $BiVO_4/SnO_2$ and (d) $BiVO_4/WO_3$ photoanodes.

was measured at the PL peak point of 550 nm, and the PL lifetime was analyzed as represented in the inset of Figure 2.7(b). The values of the fast lifetime (τ_1) were similar between samples (0.09-0.11 ns). It means that τ_1, which is originated from the non-radiative decay by trap states, is relatively independent of the bottom layer [40]. However, the values of the slow lifetime (τ_2) for $BiVO_4/SnO_2$ (1.68 ns) was shortest, compared with that for $BiVO_4$ (1.87 ns) and $BiVO_4/WO_3$ (1.75 ns). The better the photoexcited electrons are injected into the bottom layer, the shorter the lifetime (τ_2) of the charge carriers [40]. In this regard, the shortest lifetime of $BiVO_4/SnO_2$ denotes the most-efficient extraction of photoexcited electrons by SnO_2 NRs as a quenching layer. These are consistent with the charge separation efficiency (Figure 2.5(b)). As presented in Figure 2.7(c)-(d), the difference of the η_{sep} between $BiVO_4/SnO_2$ and $BiVO_4/WO_3$, which is larger than that of the η_{inj}, is derived from the electron injection effect due to the bottom layer, and is revealed as the difference in the slow lifetime (τ_2). These results provide the basis for what $BiVO_4/SnO_2$ showed remarkable front-side PEC performances.

It was anticipated that differences in the photoactivity and the charge carrier dynamic between $BiVO_4/SnO_2$ and $BiVO_4/WO_3$ sprang from the band structures. First, UV-vis spectroscopy measurements were carried out

to investigate the optical bandgap (E_g) of SnO_2, WO_3, and $BiVO_4$. As shown in Figure 2.8, the absorption coefficients (α) were calculated using UV-vis absorption spectra obtained by the transmittance and reflectance spectra, and I measured the E_g of SnO_2 (3.29 eV), WO_3 (2.80 eV), and $BiVO_4$ (2.47 eV) through Tauc plots. To reveal work functions and band edge positions, ultraviolet photoelectron spectroscopy (UPS) was measured. As shown in Figure 2.9, secondary electron emission (SEE) spectra are observed in the high binding energy region of the UPS. The work function of SnO_2 (4.32
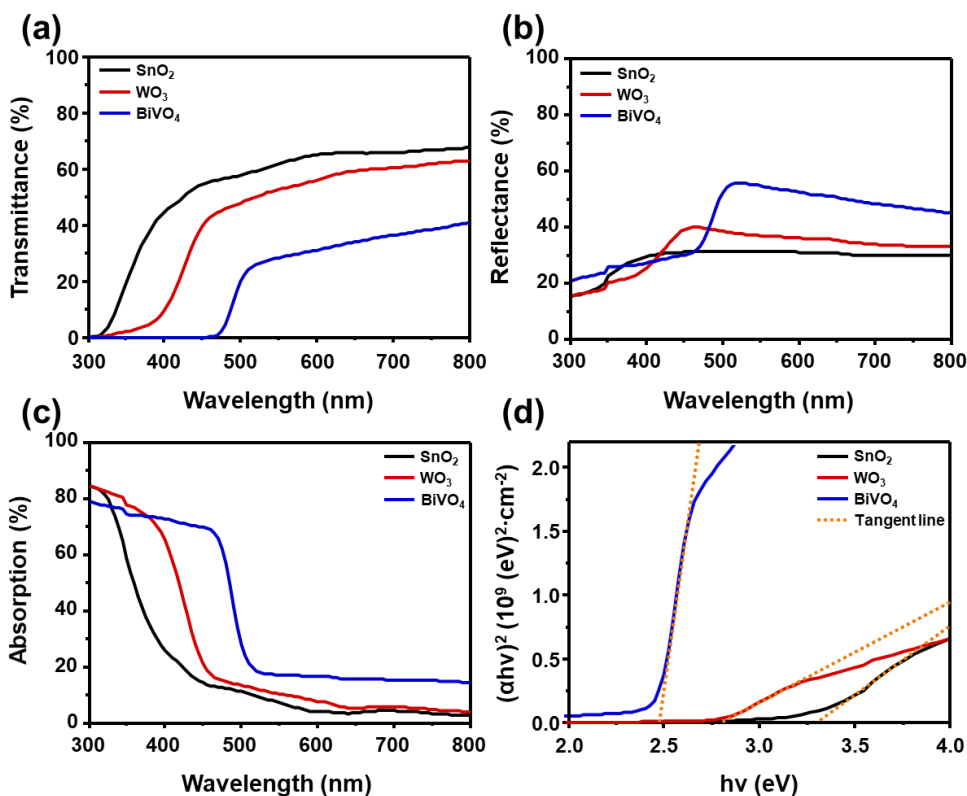
Figure 2.8 (a) UV-vis transmittance, (b) reflectance, (c) absorption spectra, and (d) Tauc plots of SnO_2, WO_3, and $BiVO_4$.

eV), WO$_3$ (4.49 eV), BiVO$_4$/SnO$_2$ (3.96 eV), and BiVO$_4$/WO$_3$ (3.90 eV) was calculated from the difference between the cut-off energy of SEE spectra and He I photon source energy (21.22 eV). Figure 2.10 shows the valence band (VB) spectra in the low binding energy region of the UPS, and the energy difference between the Fermi level and valence band maximum (E_F–E_{VBM}) can be computed. In photochemical processes, electrons at the valence band edge are involved, so the first-derivative method is used to determine the energy that the first electron can be photoexcited [41]. The values of E_F–E_{VBM} for SnO$_2$ (3.08 eV), WO$_3$ (2.51 eV), BiVO$_4$/SnO$_2$ (2.02 eV), and BiVO$_4$/WO$_3$ (2.09 eV) was obtained from the first-derivative method of the VB spectra. I worked the conduction band minimum energy (E_{CBM}) out from
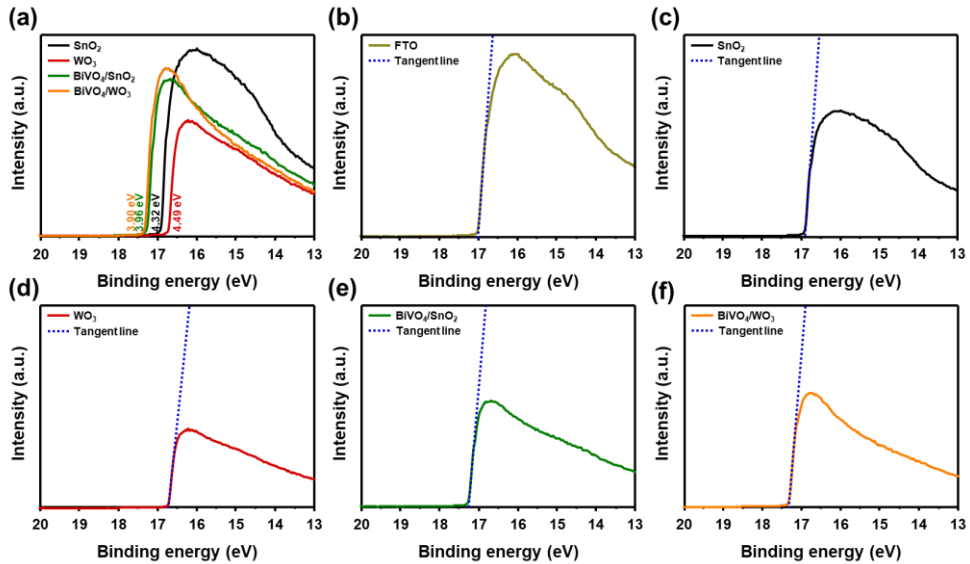
Figure 2.9 (a) The secondary electron emission (SEE) spectra of photoanodes and cut-off energy of (b) FTO, (c) SnO$_3$, (d) WO$_3$, (e) BiVO$_4$/SnO$_2$, and (f) BiVO$_4$/WO$_3$. $E_F = E_{cut\text{-}off}$ -21.22 eV (He I photon source).

the sum of E_{VBM} and E_g, and derived band energy diagrams for BiVO$_4$/SnO$_2$ and BiVO$_4$/WO$_3$. As shown in Figure 2.7(c)-(d), both photoanode systems consisted of a type II heterojunction with a staggered band alignment, which reinforces the charge transport of BiVO$_4$ [20–29]. It can support the introduction of SnO$_2$ and WO$_3$ NRs greatly enhanced the photoactivity of BiVO$_4$. Since the E_{VBM} of SnO$_2$ NRs is more negative than that of WO$_3$ NRs, the BiVO$_4$/SnO$_2$ photoanode system is more energetically favorable for the hole blocking to the bottom layer and the injection of photoexcited electrons into the bottom layer [31,42].
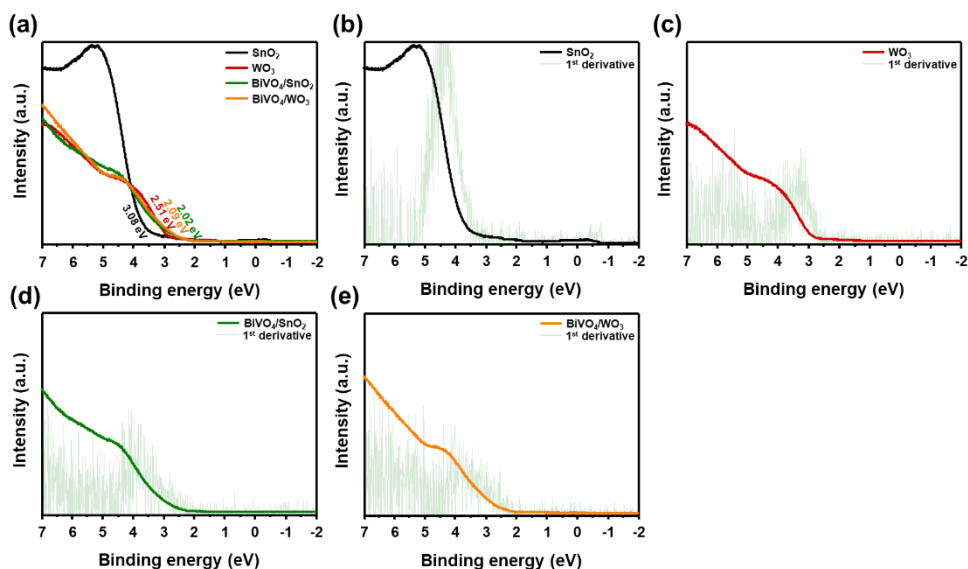
Figure 2.10 (a) The valence band (VB) spectra of photoanodes and first derivatives of (b) SnO$_2$, (c) WO$_3$, (d) BiVO$_4$/SnO$_2$, and (e) BiVO$_4$/WO$_3$. E_{VBM} = E_F–E_{edge}.

71

2.3.4. PEC water oxidation performances and TEM analysis

By combining the result of PEC characteristics and band structure analysis, I adopted the $BiVO_4/SnO_2$ photoanode for the PEC-PV tandem system. In water oxidation without the hole scavenger, various PEC degradation such as an anodic shift of onset potential, low photocurrent density, and photocorrosion appears due to poor OER kinetics of $BiVO_4$ [43-47]. To expedite the interfacial hole transfer of $BiVO_4$ into the water, I introduced NiFe oxygen evolution co-catalyst (OEC) which consists of earth-abundant elements and has high catalytic activities. NiFe OEC was deposited on $BiVO_4/SnO_2$ using e-beam evaporation of NiFe alloy pellet. As shown in
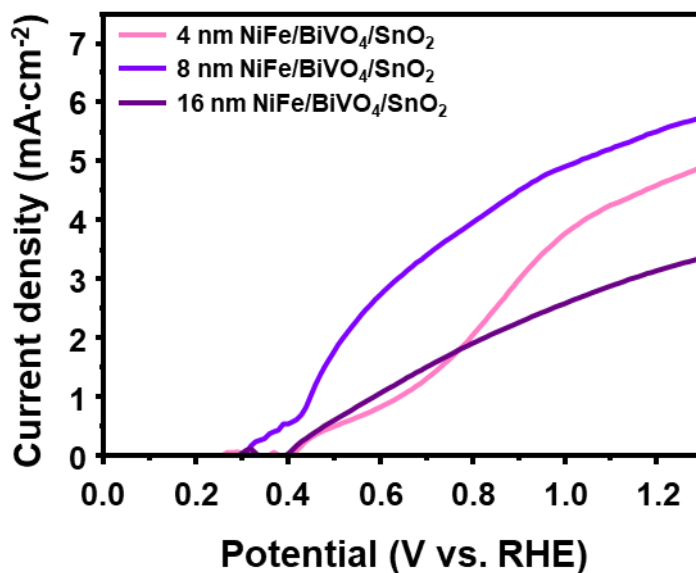
Figure 2.11 *J-V* curves of $NiFe/BiVO_4/SnO_2$ photoanodes with different thickness of NiFe catalyst at 1.23 V (versus RHE) in a 1.0 M K-B$_i$ buffer (pH 9.5) under front-side 1 sun illumination (AM 1.5G).

Figure 2.11, I measured J-V curves of NiFe/BiVO$_4$/SnO$_2$ photoanodes with different thickness of NiFe OEC, and found an optimal thickness of 8 nm. Hole transfer and surface reaction kinetics were slow at the thickness of 4 nm, and photocurrent density decreased at the thickness of 16 nm due to the increased light reflection by the metallic NiFe. To observe the morphologies and elemental distribution of NiFe OEC, I analyzed the TEM and EDS of NiFe/BiVO$_4$/SnO$_2$. As displayed in the expanded TEM image and EDS mapping of the BiVO$_4$ region (Figure 2.12(a)-(c)), NiFe OEC with an optimal thickness of 8 nm is intimately coated on the surface of the BiVO$_4$, indicating the evenly distributed Ni and Fe elements.

PEC water oxidation performances of NiFe/BiVO$_4$/SnO$_2$ photoanode were further studied in a 1.0 M potassium borate (K-B$_i$) buffer (pH 9.5) without the hole scavenger under front-side 1 sun illumination (AM 1.5G). For a catalytic activation of NiFe OEC, the photoanode was linearly swept several times in a potential range of 0 V to 1.4 V versus RHE before measurement (Figure 2.13(a)-(b)). As the number of sweeping increased, the photoactivity of the photoanode was enhanced, but the thickness of NiFe remained similar. According to J-V curves for the photoanode with and without NiFe OEC (Figure 2.12(d)), NiFe/BiVO$_4$/SnO$_2$ generated a high photocurrent density of 5.61 mA cm^{-2} at 1.23 V versus RHE, which is an

enhancement of 65% compared to that of $BiVO_4/SnO_2$ (3.39 mA cm^{-2}). A

cathodic onset potential shift of 400 mV means that NiFe OEC expedites the

hole transfer into the electrolyte and improves the surface kinetics for the
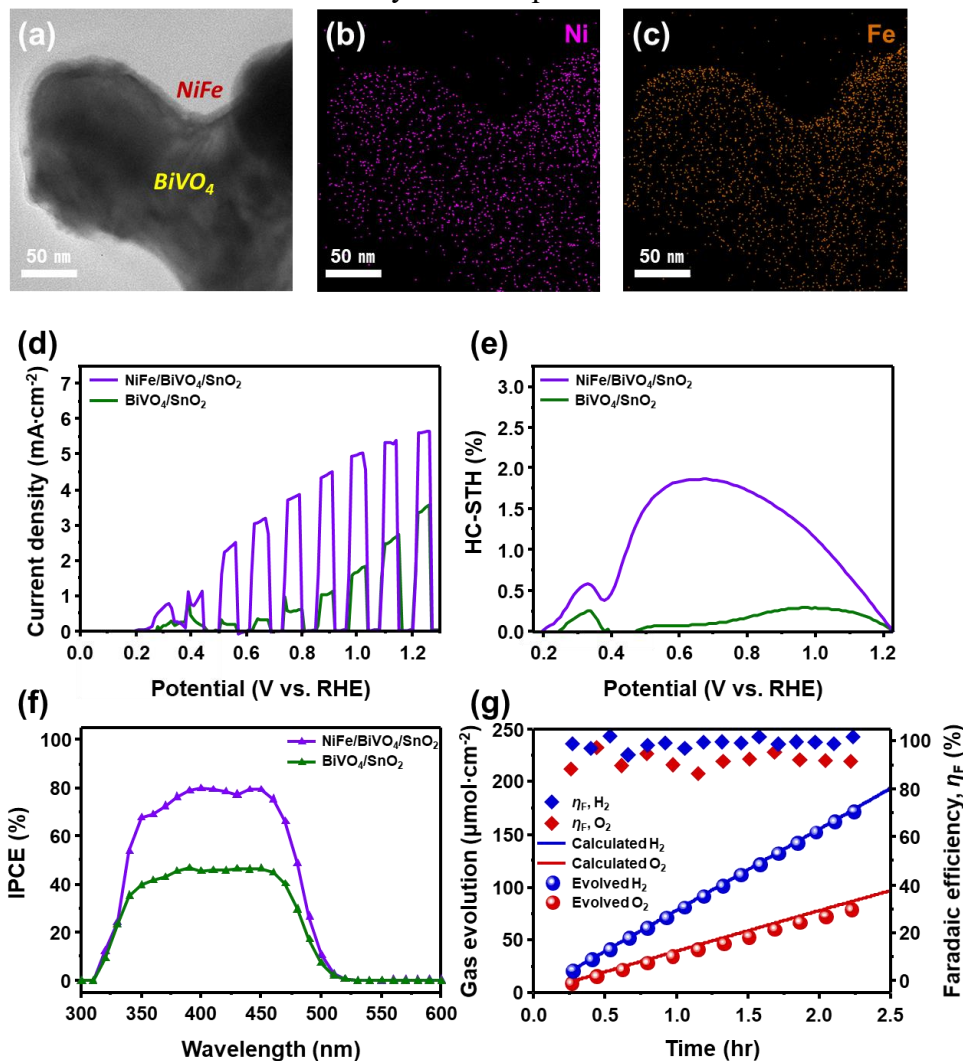
Figure 2.12 (a) Expanded TEM image of $BiVO_4$ region. EDS mappings of (b) Ni, (c) Fe. (d) *J-V* curves, (e) HC-STH curves, (f) IPCE spectra at 1.23 V (versus RHE) of $NiFe/BiVO_4/SnO_2$ and $BiVO_4/SnO_2$ photoanodes. (g) Gas evolution and Faradaic efficiency of $NiFe/BiVO_4/SnO_2$ photoanode. All measurements were carried out in a 1.0 M potassium borate (K-B$_i$) buffer (pH 9.5) without the hole scavenger under front-side 1 sun illumination (AM 1.5G).

water oxidation. As shown in Figure 2.12(e), both high photocurrent density and onset potential shift of NiFe/BiVO$_4$/SnO$_2$ caused a remarkable increase in HC-STH although the peak was observed near the 0.4 V versus RHE due to charge recombination of BiVO$_4$. The maximum HC-STH of
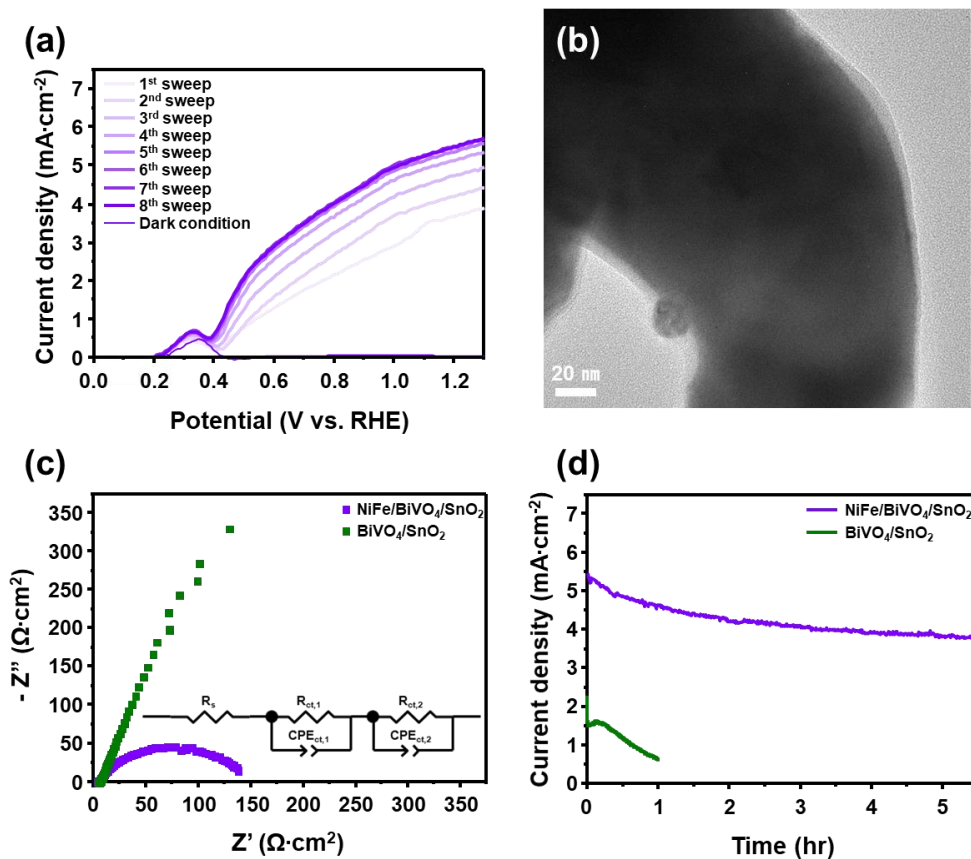
Figure 2.13 (a) *J-V* curves of NiFe/BiVO$_4$/SnO$_2$ photoanode with the number of sweep. (b) TEM image of NiFe/BiVO$_4$/SnO$_2$ after catalytic activation of NiFe OEC. (c) EIS curves of NiFe/BiVO$_4$/SnO$_2$ and BiVO$_4$/SnO$_2$ photoanodes at 0.60 V (versus RHE) in a 1.0 M K-B$_i$ buffer (pH 9.5) without the hole scavenger under front-side 1 sun illumination (AM 1.5G). (d) Chronoamperometric curves of NiFe/BiVO$_4$/SnO$_2$ and BiVO$_4$/SnO$_2$ photoanodes at 1.23 V (versus RHE) in a 1.0 M K-B$_i$ buffer (pH 9.5) without the hole scavenger under front-side 1 sun illumination (AM 1.5G).

NiFe/BiVO$_4$/SnO$_2$ (1.87% at 0.68 V versus RHE) was 4.5 times higher than that of BiVO$_4$/SnO$_2$ (0.34% at 1.0 V versus RHE). According to IPCE measurements to identify the effects of NiFe OEC (Figure 2.12(f)), NiFe/BiVO$_4$/SnO$_2$ exhibited a maximum IPCE of around 80% at a wavelength of up to 450 nm, whereas that of BiVO$_4$/SnO$_2$ was lower than 50% at the same wavelength range. The EIS analysis for the photoanode with or without NiFe OEC was carried out at 0.60 V versus RHE, which is near the onset potential of BiVO$_4$/SnO$_2$ (Figure 2.13(c)). As listed in Table 2.2, the fitted $R_{ct,1}$ and $R_{ct,2}$ value of NiFe/BiVO$_4$/SnO$_2$ (115.43 Ω cm^2, 26.47 Ω cm^2) was much smaller than that of BiVO$_4$/SnO$_2$ (3066.68 Ω cm^2, 1024.94 Ω cm^2), verifying the effect of NiFe OEC with respect to the charge transfer kinetics. As shown in chronoamperometric curves at 1.23 V versus RHE (Figure 2.13(d)), the photocurrent density of BiVO$_4$/SnO$_2$ was decayed by 72% for 1 hour, while that of NiFe/BiVO$_4$/SnO$_2$ decreased only 15%. The anodic photocorrosion of BiVO$_4$, which was originated from accumulated holes and photo-induced dissolution of V^{5+} to the electrolyte, cause the poor photostability [18,46,47]. NiFe OEC makes BiVO$_4$ be continuously separated with the electrolyte during water oxidation, enabling an operation duration of 5.5 hours for NiFe/BiVO$_4$/SnO$_2$ with 70% performance maintenance. Oxygen and hydrogen evolution by the NiFe/BiVO$_4$/SnO$_2$ photoanode and Pt cathode were detected using gas chromatography (GC)

at 1.23 V versus RHE, as shown in Figure 2.12(g). Faradaic efficiencies were recorded nearly 100%, indicating that most of the photogenerated are consumed for oxygen and hydrogen evolution.

Table 2.2 Fitted series resistance (R_s) and charge transfer resistance ($R_{ct,1}$, $R_{ct,2}$) of photoanodes.

Photoanodes	R_s [Ω cm^2]	$R_{ct,1}$ [Ω cm^2]	$R_{ct,2}$ [Ω cm^2]
BiVO$_4$/SnO$_2$	6.51	3066.68	1024.94
NiFe/BiVO$_4$/SnO$_2$	5.54	115.43	26.47

2.3.5. Spontaneous water oxidation of the PEC-PV tandem cell in zero-bias

Finally, as illustrated in Figure 2.14(a), I fabricated a PEC-PV tandem cell by combining NiFe/BiVO$_4$/SnO$_2$ photoanode and a perovskite/Si tandem solar cell to implement zero-bias PEC water splitting. As recently reported [32], the perovskite/Si tandem solar cell generated a short-circuit current
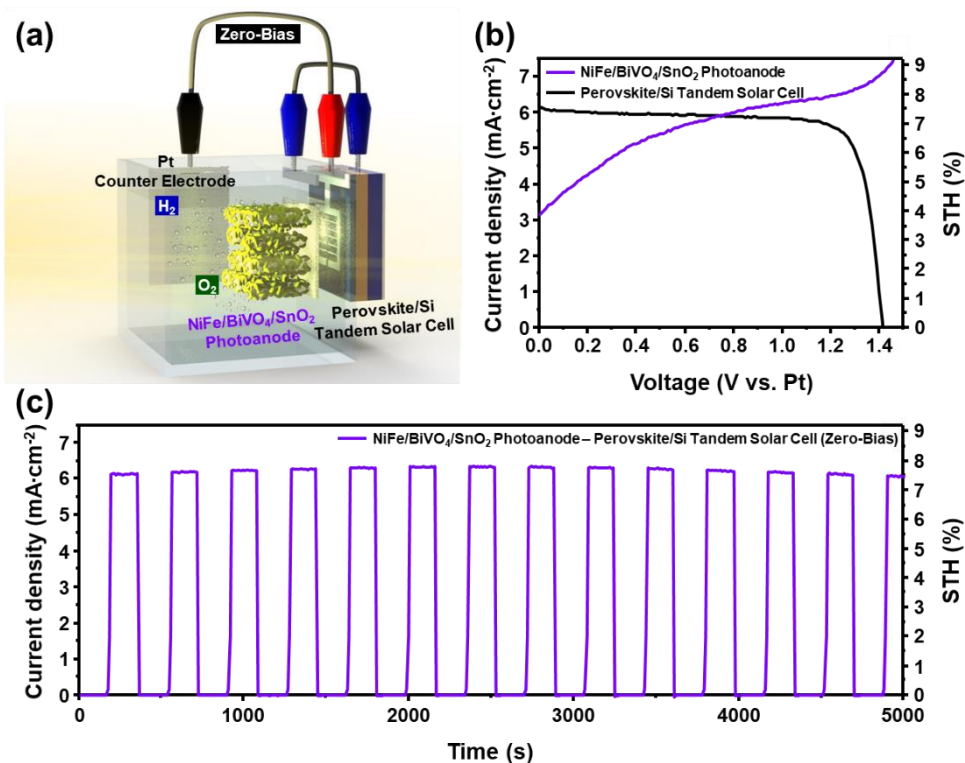
Figure 2.14 (a) Schematic of the PEC-PV tandem cell with NiFe/BiVO$_4$/SnO$_2$ photoanode and perovskite/Si tandem solar cell. (b) Two electrode *J-V* curves of NiFe/BiVO$_4$/SnO$_2$ photoanode and perovskite/Si tandem solar cell (behind photoanode). (c) Chronoamperometric curve of PEC-PV tandem cell in zero-biased two-electrode system. All measurements were carried out in zero-bias in a 1.0 M K-B$_i$ buffer (pH 9.5) without the hole scavenger under front-side 1 sun illumination (AM 1.5G).

density (J_{sc}) of 19.53 mA cm^{-2} and an open-circuit potential (V_{oc}) of 1.80 V with a fill factor (FF) of 0.76, exhibiting a power-conversion efficiency (η) of 26.75% (Figure 2.15). As shown in Figure 2.14(b), I recorded the two-electrode J-V curve between NiFe/BiVO$_4$/SnO$_2$ photoanode and Pt cathode in a 1.0 M K-B$_i$ buffer (pH 9.5) without the hole scavenger under the front-side 1 sun illumination (AM 1.5G). Also, that of perovskite/Si tandem solar cell was independently obtained under the illumination filtered by the front photoanode. Since there is no reference electrode in the two-electrode system, the potential of the counter electrode changes during the measurement, and it showed a difference in the photocurrent density with the three-electrode system [48–50]. The intersection defines operating photocurrent density (J_{op}) and voltage (V_{op}) of the PEC-PV tandem cell [31,48–53]. High J_{op} of 5.90 mA cm^{-2} was identified at the V_{op} of 0.75 V, which is attributed to great PEC performances of NiFe/BiVO$_4$/SnO$_2$ under front-side illumination. Also, as the light absorption wavelength range of the
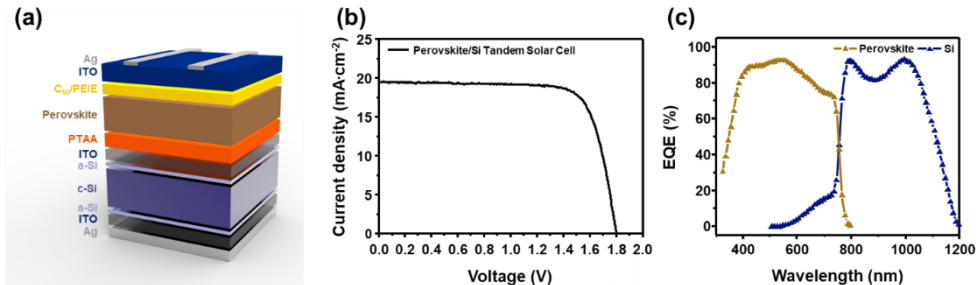
Figure 2.15 (a) Schematic of the perovskite/Si tandem solar cell. (b) J-V curve and (c) EQE spectra of the perovskite/Si tandem solar cell in a two-electrode system under 1 sun illumination (AM 1.5G).

solar cell does not overlap much with the photoanode, it can supply a sufficient voltage by using the light transmitted through the photoanode [32,33]. In other words, as shown in IPCE of the photoanode (Figure 2.12(f)) and EQE of the solar cell (Figure 2.15(c)), the short wavelength light ($\lambda < 500$ nm) is absorbed by the $NiFe/BiVO_4/SnO_2$ photoanode, and the passed long wavelength light ($\lambda > 500$ nm) is absorbed by the perovskite/Si tandem solar cell. If the interfacial charge transfer rate of the photoanode is improved beyond the charge recombination rate at higher cell temperature conditions, more increased operating photocurrent density can be generated by the PEC-PV tandem system under higher light intensity [54]. The chronoamperometric measurement of the PEC-PV tandem cell was conducted in zero-bias under chopped light for 5000 seconds (Figure 2.14(c)). The current density was well-matched with the J_{op} of 5.90 mA cm^{-2} without any external bias, indicating a corresponding STH conversion efficiency of 7.3%.

2.4. Conclusion

For the maximization of the charge separation of BiVO$_4$, I harnessed nanorod-type bottom layers and demonstrated PEC performances under front-side illumination. I discovered the optimal growth time of BiVO$_4$ so that nanopores of BiVO$_4$ and mesopores of bottom layers coexist. This vertical 1-d structure with a large specific surface area boosted the charge separation efficiency, and SnO$_2$ NRs were more beneficial to the effect than WO$_3$ NRs, according to the analysis of PL and UPS. The synergistic effect on both surface structure and band structure made BiVO$_4$/SnO$_2$ photoanode reach 84% of the theoretical photocurrent density (6.31 mA cm^{-2} at 1.23 V versus RHE), exhibiting near-complete charge separation efficiency of 97%. Upon loading NiFe OEC, the photoanode generated a high photocurrent density of 5.61 mA cm^{-2} at 1.23 V versus RHE in water oxidation without a hole scavenger. The PEC-PV tandem cell with NiFe/BiVO$_4$/SnO$_2$ photoanode and perovskite/Si tandem solar cell spontaneously caused water oxidation, delivering the operating photocurrent density of 5.90 mA cm^{-2} and STH conversion efficiency of 7.3% in zero-bias. This study provides strategies to design high-performance photoanode and fosters the development of spontaneous solar water oxidation.

2.5. References

[1]   M. G. Walter, E. L. Warren, J. R. McKone, S. W. Boettcher, Q. Mi, E. A. Santori, N. S. Lewis, *Chem. Rev.*, **2010**, 110, 6446.

[2]   J. H. Kim, D. Hansora, P. Sharma, J. W. Jang, J. S. Lee, *Chem. Soc. Rev.*, **2019**, 48, 1908.

[3]   J. L. Young, M. A. Steiner, H. Döscher, R. M. France, J. A. Turner, T. G. Deutsch, *Nat. Energy*, **2017**, 2, 17028.

[4]   W. Yang, R. R. Prabhakar, J. Tan, S. D. Tilley, J. Moon, *Chem. Soc. Rev.*, **2019**, 48, 4979.

[5]   L. Pan, J. H. Kim, M. T. Mayer, M. K. Son, A. Ummadisingu, J. S. Lee, A. Hagfeldt, J. Luo, M. Grätzel, *Nat. Catal.*, **2018**, 1, 412.

[6]   J. H. Kim, J. W. Jang, Y. H. Jo, F. F. Abdi, Y. H. Lee, R. Van De Krol, J. S. Lee, *Nat. Commun.*, **2016**, 7, 13380.

[7]   J. H. Kim, Y. Jo, J. H. Kim, J. W. Jang, H. J. Kang, Y. H. Lee, D. S. Kim, Y. Jun, J. S. Lee, *ACS Nano*, **2015**, 9, 11820.

[8]   P. Dias, M. Schreier, S.D. Tilley, J. Luo, J. Azevedo, L. Andrade, D. Bi, A. Hagfeldt, A. Mendes, M. Grätzel, M. T. Mayer, *Adv. Energy Mater.*, **2015**, 5, 1501537.

[9]   Y. S. Chen, J. S. Manser, P. V. Kamat, *J. Am. Chem. Soc.*, **2015**, 137, 974.

[10]   S. Xiao, C. Hu, H. Lin, X. Meng, Y. Bai, T. Zhang, Y. Yang, Y. Qu, K. Yan, J. Xu, Y. Qiu, S. Yang, *J. Mater. Chem. A*, **2017**, 5, 19091.

[11]   K. J. McDonald, K. S. Choi, *Energy Environ. Sci.*, **2012**, 5, 8553.

[12]   Z. F. Huang, L. Pan, J. J. Zou, X. Zhang, L. Wang, *Nanoscale*, **2014**, 6, 14044.

[13]   J. H. Kim, J. S. Lee, *Adv. Mater.*, **2019**, 31, 1806938.

[14]   Y. Park, K. J. Mc Donald, K. S. Choi, *Chem. Soc. Rev.*, **2013**, 42, 2321.

[15]   Y. Kuang, Q. Jia, H. Nishiyama, T. Yamada, A. Kudo, K. Domen, *Adv. Energy Mater.*, **2016**, 6, 1501645.

[16]   J. A. Seabold, K. Zhu, N. R. Neale, *Phys. Chem. Chem. Phys.*, **2014**, 16, 1121.

[17]   T. W. Kim, Y. Ping, G. A. Galli, K. S. Choi, *Nat. Commun.*, **2015**, 6, 8769.

[18]   D. K. Lee, K. S. Choi, *Nat. Energy*, **2018**, 3, 53.

[19]   W. Kim, K. S. Choi, *Science*, **2014**, 343, 990.

[20]   S. S. M. Bhat, J. M. Suh, S. Choi, S. P. Hong, S. A. Lee, C. Kim, C. W. Moon, M. G. Lee, H. W. Jang, *J. Mater. Chem. A*, **2018**, 6, 14633.

[21]   L. Zhou, C. Zhao, B. Giri, P. Allen, X. Xu, H. Joshi, Y. Fan, L. V. Titova, P. M. Rao, *Nano Lett.*, **2016**, 16, 3463.

[22]   S. Byun, B. Kim, S. Jeon, B. Shin, *J. Mater. Chem. A*, **2017**, 5, 6905.

[23]   S. Bera, S. A. Lee, C. M. Kim, H. Khan, H. W. Jang, S. H. Kwon, 2018, *Chem. Mater.*, 30, 8501.

[24]   M. G. Lee, D. H. Kim, W. Sohn, C. W. Moon, H. Park, S. Lee, H. W. Jang, *Nano Energy*, **2016**, 28, 250.

[25]   M. G. Lee, K. Jin, K. C. Kwon, W. Sohn, H. Park, K. S. Choi, Y. K. Go, H. Seo, J. S. Hong, K. T. Nam, H. W. Jang, *Adv. Sci.*, **2018**, 5, 1800727.

[26]   B. R. Lee, M. G. Lee, H. Park, T. H. Lee, S. A. Lee, S. S. M. Bhat, C. Kim, S. Lee, H. W. Jang, *ACS Appl. Mater. Interfaces*, **2019**, 11, 20004.

[27]   J. H. Kim, D. H. Kim, J. W. Yoon, Z. Dai, J. H. Lee, *ACS Appl. Energy Mater.*, **2019**, 2, 4535.

[28]   P.M. Rao, L. Cai, C. Liu, I. S. Cho, C. H. Lee, J. M. Weisse, P. Yang, X. Zheng, *Nano Lett.*, **2014**, 14, 1099.

[29]   X. Shi, I. Y. Choi, K. Zhang, J. Kwon, D. Y. Kim, J. K. Lee, S. H. Oh, J. K. Kim, J. H. Park, *Nat. Commun.*, **2014**, 5, 4775.

[30]   J. Resasco, H. Zhang, N. Kornienko, N. Becknell, H. Lee, J. Guo, A. L. Briseno, P. Yang, *ACS Cent. Sci.*, **2016**, 2, 80.

[31]   J. H. Baek, B. J. Kim, G. S. Han, S. W. Hwang, D. R. Kim, I. S. Cho, H. S. Jung, *ACS Appl. Mater. Interfaces*, **2017**, 9, 1479.

[32]   D. Kim, H. J. Jung, I. J. Park, B. W. Larson, S. P. Dunfield, C. Xiao, J. Kim, J. Tong, P. Boonmongkolras, S. G. Ji, F. Zhang, S. R. Pae, M. Kim, S. B. Kang, V. Dravid, J. J. Berry, J. Y. Kim, K. Zhu, D. H. Kim, B. Shin, *Science*, **2020**, 368, 155.

[33]   I. J. Park, J. H. Park, S. G. Ji, M. A. Park, J. H. Jang, J. Y. Kim, *Joule*, **2019**, 3, 807.

[34]   R. E. Nowak, M. Vehse, O. Sergeev, K. Von Maydell, C. Agert, *Sol. Energy Mater. Sol. Cells*, 2014, 125, 305.

[35]   Y. Ma, S. R. Pendlebury, A. Reynal, F. Le Formal, J. R. Durrant, *Chem. Sci.*, **2014**, 5, 2964.

[36]   K. H. Ye, H. Li, D. Huang, S. Xiao, W. Qiu, M. Li, Y. Hu, W. Mai, H. Ji, S. Yang, *Nat. Commun.*, **2019**, 10, 3687.

[37] S. A. Lee, T. H. Lee, C. Kim, M. G. Lee, M. J. Choi, H. Park, S. Choi, J. Oh, H. W. Jang, *ACS Catal.*, **2018**, 8, 7261.

[38] S. A. Lee, T. H. Lee, C. Kim, M. J. Choi, H. Park, S. Choi, J. Lee, J. Oh, S. Y. Kim, H. W. Jang, *ACS Catal.*, **2020**, 10, 420.

[39] D. Kim, Z. Zhang, K. Yong, *Nanoscale*, **2018**, 10, 20256.

[40] L. Zhang, Y. Li, C. Li, Q. Chen, Z. Zhen, X. Jiang, M. Zhong, F. Zhang, H. Zhu, *ACS Nano*, **2017**, 11, 12753.

[41] C. Maheu, L. Cardenas, E. Puzenat, P. Afanasiev, C. Geantet, *Phys. Chem. Chem. Phys.*, **2018**, 20, 25629.

[42] Q. Jiang, X. Zhang, J. You, *Small*, **2018**, 14, 1801154.

[43] W. Liu, H. Liu, L. Dang, H. Zhang, X. Wu, B. Yang, Z. Li, X. Zhang, L. Lei, S. Jin, *Adv. Funct. Mater.*, **2017**, 27, 1603904.

[44] S. Wang, T. He, J. H. Yun, Y. Hu, M. Xiao, A. Du, L. Wang, *Adv. Funct. Mater.*, **2018**, 28, 1802685.

[45] B. Moss, F. S. Hegner, S. Corby, S. Selim, L. Francàs, N. López, S. Giménez, J. R. Galán-Mascarós, J. R. Durrant, *ACS Energy Lett.*, **2019**, 4, 337.

[46]   Y. Shi, Y. Yu, Y. Yu, Y. Huang, B. Zhao, B. Zhang, *ACS Energy Lett.*, **2018**, 3, 1648.

[47]   Y. Kuang, Q. Jia, G. Ma, T. Hisatomi, T. Minegishi, H. Nishiyama, M. Nakabayashi, N. Shibata, T. Yamada, A. Kudo, K. Domen, *Nat. Energy*, **2017**, 2, 16191.

[48]   X. Shi, H. Jeong, S. J. Oh, M. Ma, K. Zhang, J. Kwon, I. T. Choi, I. Y. Choi, H. K. Kim, J. K. Kim, J. H. Park, *Nat. Commun.*, **2016**, 7, 11943.

[49]   F. F. Abdi, L. Han, A. H. M. Smets, M. Zeman, B. Dam, R. Van De Krol, *Nat. Commun.*, **2013**, 4, 2195.

[50]   D. Xue, M. Kan, X. Qian, Y. Zhao, *ACS Sustainable Chem. Eng.*, **2018**, 6, 16228.

[51]   S. Wang, P. Chen, Y. Bai, J. H. Yun, G. Liu, L. Wang, *Adv. Mater.*, **2018**, 30, 1800486.

[52]   M. Kim, B. Lee, H. Ju, J. Y. Kim, J. Kim, S. W. Lee, *Adv. Mater.*, **2019**, 31, 1903316.

[53]   X. Shi, K. Zhang, K. Shin, M. Ma, J. Kwon, I. T. Choi, J. K. Kim, H. K. Kim, D. H. Wang, J. H. Park, *Nano Energy*, **2015**, 13, 182.

[54]   Y. Pihosh, I. Turkevych, K. Mawatari, J. Uemura, Y. Kazoe, S. Kosar, K. Makita, T. Sugaya, T. Matsui, D. Fujita, M. Tosa, M. Kondo, T. Kitamori, *Sci. Rep.*, **2015**, 5, 11141.

Chapter 3

Tailored BiVO$_4$/In$_2$O$_3$ nanostructures with boosted charge separation ability toward unassisted water splitting

3.1. Introduction

Photoelectrochemical (PEC) water splitting is one of the most desirable routes for sustainable hydrogen production, which is an ideal energy carrier. It can make a completely carbon-free energy economy because it utilizes the unlimited energy source of solar light and does not emit carbon dioxide [1]. However, this technology still has many hurdles to surmount, such as low solar-to-hydrogen (STH) conversion efficiency than 10% for practical stand-alone PEC water splitting devices [2-5]. Thus, deliberate consideration of materials is very important to improving the sluggish, multistep, and proton-coupled electron transfer kinetics of limited water oxidation on the photoanodes' surface [6,7]. In addition, the construction of tandem systems comprising the PEC and photovoltaic (PV) cells is another attractive route to maximize the STH conversion efficiency through enhanced light harvesting [1,8-10].

Bismuth vanadate ($BiVO_4$) has received great attention on account of the relatively narrow band gap of 2.4 eV for visible light absorption and favorable conduction band edge position (0.1–0.2 V versus normal hydrogen electrode) for hydrogen evolution [11-12]. However, the demonstrated STH conversion efficiency and photocurrent density of the $BiVO_4$-based photoanode to date are considerably low compared to theoretical values (photocurrent density of 7.5 mA cm^{-2} and STH conversion efficiency of 9.2%

at 1.23 V versus reversible hydrogen electrode (V_{RHE})) [2,4,13-16]. The representative reasons for the current limitation are a short carrier diffusion length (~70 nm) and stagnant oxygen evolution reaction (OER) kinetics of $BiVO_4$, which reduce the charge separation efficiency (η_{sep}) and charge injection efficiency (η_{inj}), respectively [11,17]. Various strategies have been widely employed to improve the efficiencies, including doping [4,18], nanostructuring [13,15,19], heterojunction [17,20-22], and surface modifications such as passivation layer and oxygen evolution catalyst (OEC) [23-25]. Despite worldwide intensive research over the past decades, current state-of-the-art PV-PEC tandem cell systems based on the $NiOOH/FeOOH/Mo,W:BiVO_4/WO_3$ photoanode showed a benchmark STH conversion efficiency of 7% (photocurrent density of 4.2 mA cm^{-2} at 1.23 V_{RHE}) by Park *et al*. [2]. Thus, the exploration for a new configuration of $BiVO_4$-based photoelectrodes is indispensable to making a breakthrough for realizing the practical solar-driven water splitting. Also, introducing a proper PV cell, which can provide a sufficiently large photovoltage with only light transmitted through the $BiVO_4$-based photoanode, is essential to driving bias-free PEC water splitting and achieving high STH conversion efficiency [6,10,26,27].

Herein, I endeavor to explore new BiVO$_4$-based heterostructures exceeding previous best records of NiFeO$_x$/BiVO$_4$/WO$_3$ photoanodes [2,15,28-30] and implement unbiased water splitting via PV-PEC tandem cell. I firstly introduces indium oxide (In$_2$O$_3$) nanorods (NRs) with high electrical conductivity as an effective electron transport layer (ETL) to overcome limitations of WO$_3$ such as relatively positive flat band potential of about 0.4 V$_{RHE}$, causing potential energy losses for electrons and limiting the photovoltage of the total photoelectrodes [31-35]. As a result, the optimal nanodot BiVO$_4$/In$_2$O$_3$ NRs photoanode generates a photocurrent density of 6.1 mA cm^{-2} and η_{sep} of 98% at 1.23 V$_{RHE}$ in sulfite oxidation reaction (SOR). Based on the various analysis of the charge carrier dynamics, I can confirm that the PEC results originated from the better charge separation of nanodot BiVO$_4$/In$_2$O$_3$ NRs compared to core-shell BiVO$_4$/In$_2$O$_3$ NRs. Then, a tannin-nickel-iron complex (TANF) is uniformly coated on BiVO$_4$/In$_2$O$_3$ NRs as an OEC to expedite the charge transfer. Based on the novel triple heterojunction of TANF/BiVO$_4$/In$_2$O$_3$ NRs, I obtains a high photocurrent density of 7.1 mA cm^{-2} at 1.23 V$_{RHE}$ in sulfite oxidation. Also, in water oxidation, the TANF/BiVO$_4$/In$_2$O$_3$ NRs photoanode records a photocurrent density of 4.2 mA cm^{-2} at 1.23 V$_{RHE}$, which is a 16.6 times improvement over that of BiVO$_4$/In$_2$O$_3$ NRs photoanode. Finally, by combining a perovskite/silicon (Si) solar cell behind the TANF/BiVO$_4$/In$_2$O$_3$ NRs photoanode, I developes

an unbiased PV-PEC tandem cell generating a STH conversion efficiency of

6.2% in spontaneous water oxidation.

3.2. Experimental procedures

3.2.1. Preparation of In$_2$O$_3$ NRs

Fluorine-doped tin oxide (FTO) glass substrates (1.5×1 cm^2 in size) were employed as a substrate, and glancing angle deposition (GLAD) of e-beam evaporator was used to fabricate In$_2$O$_3$ NRs. As a starting material, In$_2$O$_3$ sources (99.99%, Taewon Scientific Co.) were filled in carbon crucibles, and the chamber was evacuated to a pressure of 2×10^{-6} torr. To enhance adhesion between FTO and NRs, 50-nm-thick In$_2$O$_3$ thin film was deposited on FTO with a deposition rate of 1 Å s^{-1}. With a glancing angle of 82.5° and a rotation speed of 80 rpm, 3-μm-thick In$_2$O$_3$ NRs were deposited on the In$_2$O$_3$ thin film. After the deposition, black-colored In$_2$O$_3$ NRs precursors were annealed in air at 600 °C for 2 h (ramping rate of 2 °C min^{-1}), and the color was changed into light gray.

3.2.2. Preparation of BiVO$_4$/In$_2$O$_3$ NRs

Pulsed electrodeposition was employed to synthesize BiVO$_4$ on In$_2$O$_3$ NRs. The three-electrode cell was composed of In$_2$O$_3$ NRs working electrode, Pt counter electrode, and Ag/AgCl reference electrode.[17] A aqueous solution dissolving 30 mM bismuth nitrate pentahydrate (Bi(NO$_3$)$_3$·5H$_2$O, 98%, Junsei) and 27 mM vanadium oxide sulfate hydrate (VOSO$_4$·xH$_2$O, 99.99%, Aldrich) at pH < 0.5 with nitric acid (HNO$_3$, 60%, Junsei) was prepared. The plating solution was adjusted to pH 5.1 with sodium acetate (CH$_3$COONa, 99%, Aldrich), followed by adjusting to pH 4.7 with nitric acid to form vanadium (IV) precipitates. The pulsed electrodeposition of BiVO$_4$ was carried out under alternatively applied potentials of 0 V and 1.95 V at a temperature of 80 °C. After the deposition, brown-colored BiVO$_4$ precursors were annealed in air at 500 °C for 6 h (ramping rate of 2 °C min^{-1}), and the color was changed into yellow.

3.2.3. Preparation of TANF/BiVO₄/In₂O₃ NRs

Dip coating of TANF on $BiVO_4$/In_2O_3 NRs is devised by previously reported methods [24]. A $BiVO_4$/In_2O_3 NRs sample was put in an empty 20 mL vessel. The soaking solution containing 2.5 mL of 10 mM iron (III) chloride hexahydrate ($FeCl_3 \cdot 6H_2O$, 98%, Daejung) and 7.5 mL of 10 mM nickel chloride hexahydrate ($NiCl_2 \cdot 6H_2O$, 96%, Daejung) was poured into the vessel. After 15 min, 10 mL of 9 mg L^{-1} tannic acid (Aldrich) solution was added, followed by quickly adjusting the pH to ~8 with 2 M sodium hydroxide (NaOH, 97%, Daejung). After 2 hours without any disturbance, TANF/$BiVO_4$/In_2O_3 NRs photoanode was rinsed with deionized water and dried naturally.

3.2.4. Fabrication of perovskite/Si solar cell

At the rear side of double-polished n-type Si wafers with 300 μm thickness, random pyramids were formed and it was cleaned using the RCA process (immersion in $HCl:H_2O_2$ and $H_2SO_4:H_2O_2$ solution and buffered oxide etching solution). Amorphous Si (a-Si) films were deposited using a plasma-enhanced chemical vapor deposition (PECVD) and doped by hydrogen-diluted PH_3 and B_2H_6 gases. Indium tin oxide (ITO) films with thicknesses of 20 nm and 80 nm were deposited at the top and bottom of the Si cell, respectively, using radio frequency (RF) sputtering. A 300-nm-thick Ag film was deposited as an bottom electrode using a thermal evaporator. On the recombination layer, poly(triarylamine) (PTAA) solution was spin-coated at 6000 rpm for 25 s, followed by annealing at 100 °C for 10 min. The stoichiometric perovskite $(FA_{0.70}MA_{0.15}Cs_{0.15})Pb(I_{0.85}Br_{0.15})_3$ was dissolved in the mixed solvent with *N,N*-dimethylformamide (DMF) and *N*-methyl-2-pyrrolidone (NMP) (FA: formamidinium, MA: methylammonium). After 1 mol% phenethylammonium iodide (PEAI) was added, the perovskite solution was spin-coated at 4000 rpm for 20 s on the PTAA film. After immersing the spin-coated film in diethyl ether (DE) for 30 s, the film was annealed at 100 °C for 10 min. C_{60} layer was subsequently deposited by the thermal evaporator, and 0.2 wt% of polyethylenimine (PEIE) in methanol was spin-coated at 6000 rpm for 30 s. After depositing an ITO film on the

C_{60}/PEIE layer using RF sputtering, a top Ag metal grid with a thickness of 150 nm was deposited using a thermal evaporator on the ITO film.

3.2.5. Characterization

The crystal structures were identified by an X-ray diffractometer (D8 Advance, Bruker) with Cu Kα radiation. The surface morphologies of photoanodes were characterized by the field emission scanning electron microscopy (FESEM) (MERLIN Compact, JEISS). The transmission electron microscopy (TEM) (JEM-2100F, JEOL) equipped with energy-dispersive spectroscopy (EDS) was employed to obtain high-resolution TEM (HRTEM) images and elemental distributions. A fluorescence spectrometer (FlouTime 300, PicoQuant) with an excitation laser of 405 nm was used to measure photoluminescence (PL) spectra in the range from 405 nm to 700 nm and time-resolved photoluminescence (TRPL) at 543 nm. The transmittance (T) and reflectance (R) were measured by ultraviolet-visible light (UV-vis) spectrometer (V-770, JASCO), and the optical band gaps were analyzed by the absorption $(100 - T - R)$. The secondary electron emission (SEE) and valence band (VB) spectra were measured by the ultraviolet photoelectron spectroscopy (UPS) (AXIS Nova, Kratos Analytical) with a UV source of He I photon energy (21.22 eV).

3.2.6. PEC and electrochemical measurements

All of the PEC and electrochemical measurements were conducted in a three-electrode cell with a flat quartz window. Fabricated photoanodes, Pt electrode, and Ag/AgCl electrode were used as working electrodes, counter electrode, and reference electrode, respectively. During the measurements, the recorded potentials were converted into RHE using the Nernst equation below.

$$E_{RHE} = E_{Ag/AgCl} + 0.059 \times pH + E^0_{Ag/AgCl}$$

, where E_{RHE} is the potential versus RHE and $E^0_{Ag/AgCl}$ = 0.198 V at 25 °C.

A solar simulator (LS 150, Abet Technologies) equipped xenon arc lamp with AM 1.5G filter was used as a light source and calibrated to 1 sun (100 mW cm^{-2}) with a reference photodiode (S300, McScience) in the air. The PEC measurements were carried out by putting the samples as close to the front of the quartz cell as possible in order to reduce the influence of light intensity by water. The *J-V* curves were obtained under both front-side and back-side illumination. The PEC sulfite oxidation measurements were conducted in a 0.5 M potassium phosphate (K-P$_i$) buffer (pH 7.1) with 1 M Na$_2$SO$_3$ as a hole scavenger, and water oxidation measurements were conducted in a 1 M potassium borate (K-B$_i$) buffer (pH 9.5).

The incident photon-to-current conversion efficiency (IPCE) was measured at 1.23 V_{RHE} and calculated using the following equation.

$$IPCE\ (\%) = \frac{1240 \times J_{ph}}{\lambda \times P_{in}} \times 100$$

, where J_{ph} is the photocurrent density, λ is the wavelength of the monochromatic incident light, and P_{in} is the power of the incident light.

The η_{sep} and η_{inj} were calculated using the following equations.

$$J_{H_2O} = J_{abs} \times \eta_{sep} \times \eta_{inj}$$

$$J_{Na_2SO_3} = J_{abs} \times \eta_{sep}$$

, where J_{abs}, J_{H_2O}, and $J_{Na_2SO_3}$ are absorption photocurrent density and the photocurrent density in water oxidation and sulfite oxidation, respectively. The Mott-Schottky (M-S) plots were recorded at a frequency of 1 kHz under the light-off using the following equation, and I calculated the carrier concentration (N_D) by the slope of the plot.

$$C^{-2} = (2/\varepsilon\varepsilon_0 A^2 e N_D)[V - V_{FB} - (k_B T)/e]$$

, where C is the capacitance of the space charge layer, ε is the dielectric constant, ε_0 is the permittivity of vacuum (8.854×10^{-12} F m^{-1}), A is the surface area, e is the electron charge (1.602×10^{-19} C), V (versus RHE) is the applied potential, V_{FB} (versus RHE) is the flat band potential, k_B is the

101

Boltzmann constant (1.381×10^{-23} J K^{-1}), and T is the temperature (298 K). The cyclic voltammetry (CV) measurements were conducted with different scan rates under the light-off, and I obtained the electrochemically active surface area (ECSA) by analyzing the linearity between the current density difference at 0.65 V$_{RHE}$ and the scan rate in the CV.

The applied bias photon-to-current conversion efficiency (ABPE) was calculated from the J-V curve in two-electrode water oxidation measurements using the equation below.

$$ABPE\ (\%) = \frac{J_{ph} \times \left[1.23 - V_{app}\right] \times \eta_F}{P_{in}} \times 100$$

, where V_{app} is the applied bias, and η_F is the Faradaic efficiency. The electrochemical impedance spectroscopy (EIS) was measured with an AC voltage amplitude of 10 mV and a frequency range from 100 kHz to 0.1 kHz at 1.23 V$_{RHE}$, and the Nyquist plot was fitted by the Z plot 2.x software. The Faradaic efficiency and oxygen evolution were measured at 1.23 V$_{RHE}$ by connecting an air-tight cell to the gas chromatography system (7890B, Agilent Technologies).

3.2.7. PV-PEC tandem cell measurement

The PV-PEC tandem cell measurements were carried out in a two-electrode cell with Pt counter electrode in 1 M K-B$_i$ buffer (water oxidation). The *J-V* curves of the TANF/BiVO$_4$/In$_2$O$_3$ NRs photoanode and perovskite/Si solar cell behind the photoanode were measured, and the operating point was determined at their intersection. The region other than the active area of the photoanode was thickly covered with dark epoxy in order to make the active area of the photoanode and solar cell the same. The light can only enter the solar cell exactly as much as the active area of the photoanode. After electrically connecting the photoanode with the solar cell, unbiased chronoamperometric measurement in the two-electrode system was carried out. Because of the bias-free condition, the STH conversion efficiency of the PV-PEC tandem cell was calculated by setting V_{app} to zero in the ABPE equation of the photoanode as follows.

$$\eta_{STH} \ (\%) = \frac{J_{OP} \times 1.23 \times \eta_F}{P_{in}} \times 100$$

, where J_{OP} is the operating photocurrent density in the chronoamperometry.

3.3. Results and discussion

3.3.1. Preparation and structural characterization of $BiVO_4/In_2O_3$ NRs photoanodes

First, one-dimensional (1D) In_2O_3 NRs with a length of 3 µm were formed on the FTO by a glancing angle deposition (GLAD) via e-beam evaporation. For the crystallization of the In_2O_3 NRs precursor, I annealed at different temperatures of 400 °C, 500 °C, and 600 °C. As shown in Figure 3.1, the FESEM images show that porous 1D nanorod structures are well-formed, and there is no difference in the surface morphology by the annealing temperatures. Also, we confirmed that In_2O_3 NRs had a cubic phase without impurities regardless of annealing temperatures through X-ray diffraction (XRD) (Figure 3.2). To select the most photoactive In_2O_3 NRs as the ETL for $BiVO_4$, I measured the linear sweep voltammetry (LSV) of In_2O_3 NRs photoanodes in 0.5 M K-P_i buffer with 1 M Na_2SO_3, as shown in Figure 3.3. At 600 °C, the In_2O_3 NRs photoanode showed the highest photocurrent
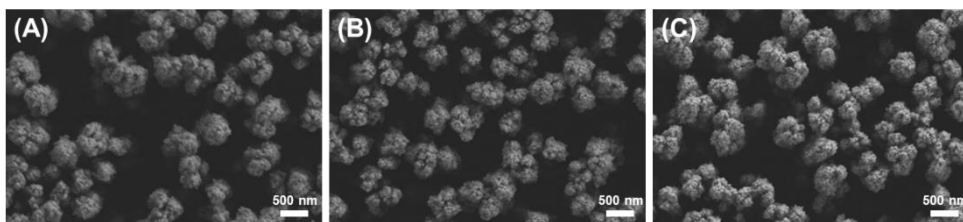
Figure 3.1 Structural characterization of pristine In_2O_3 NRs according to annealing temperatures. Top SEM images of In_2O_3 NRs with annealing temperatures of (A) 400 °C, (B) 500 °C, and (C) 600 °C.

density of 0.9 mA cm^{-2} at 1.23 V$_{RHE}$, which came from high crystallinity and

good adhesion to substrate.
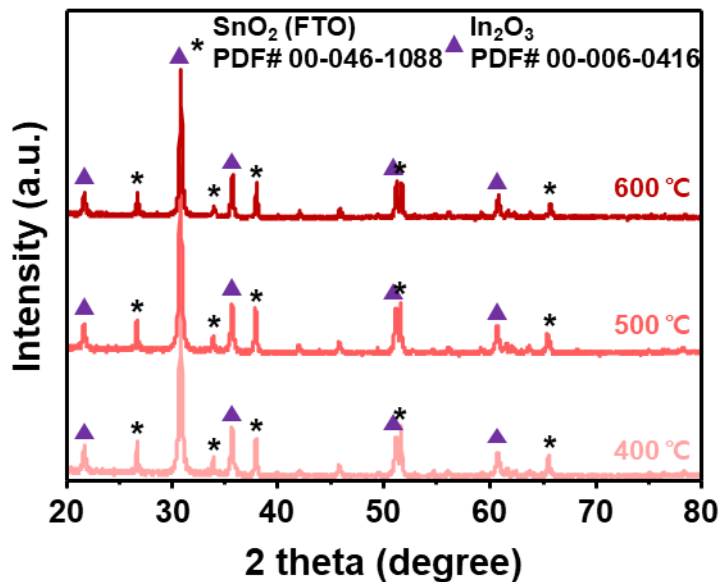
Figure 3.2 XRD of In$_2$O$_3$ NRs with different annealing temperatures.
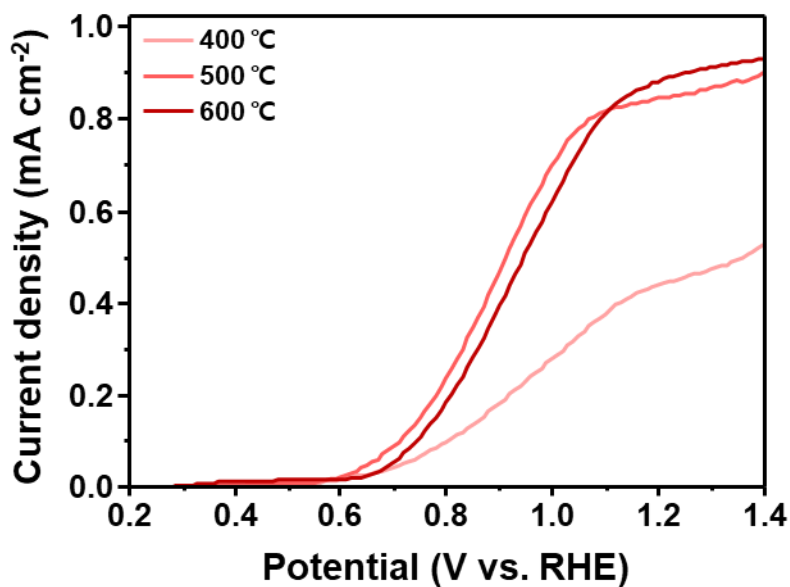
Figure 3.3 *J-V* curves of In$_2$O$_3$ NRs with different annealing temperatures in
0.5 M K-P$_i$ buffer with 1 M Na$_2$SO$_3$ under 1 sun illumination.

After that, I synthesized $BiVO_4$ on the In_2O_3 NRs annealed at 600 °C through pulsed electrodeposition to construct $BiVO_4/In_2O_3$ NRs heterojunction. In the pulsed electrodeposition, by adjusting the deposition cycle, more elaborate morphology control is possible. To adjust the coverage of $BiVO_4$, I electrodeposited $BiVO_4$ with different deposition cycles from 0 to 36 (i.e., $nBiVO_4$ = n-cycle-electrodeposited $BiVO_4$). After annealing them at 500 °C, I compared the surface morphologies of $BiVO_4/In_2O_3$ NRs with different electrodeposition cycles. As shown in Figure 3.4, from 1 to 5 cycles, nanodot structured $BiVO_4$ was formed, and rough and bumpy In_2O_3 NRs remained. By increasing the cycle from 12 to 36 cycles, the surface of In_2O_3 NRs was entirely covered with $BiVO_4$, and core-shell structured $BiVO_4$ was formed. As shown in Figure 3.5, I designated $3BiVO_4/In_2O_3$ and
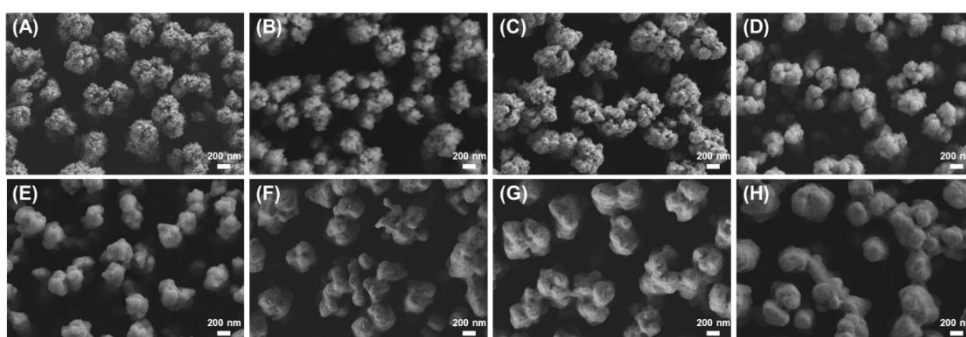
Figure 3.4 Structural characterization of In_2O_3 NRs and $BiVO_4/In_2O_3$ NRs according to electrodeposition cycles of $BiVO_4$. Top SEM images of (A) In_2O_3 NRs, (B) $1BiVO_4/In_2O_3$, (C) $3BiVO_4/In_2O_3$, (D) $5BiVO_4/In_2O_3$, (E) $12BiVO_4/In_2O_3$, (F) $18BiVO_4/In_2O_3$, (G) $24BiVO_4/In_2O_3$, and (H) $36BiVO_4/In_2O_3$.

106

18BiVO$_4$/In$_2$O$_3$ as representatives of nanodot and core-shell BiVO$_4$/In$_2$O$_3$
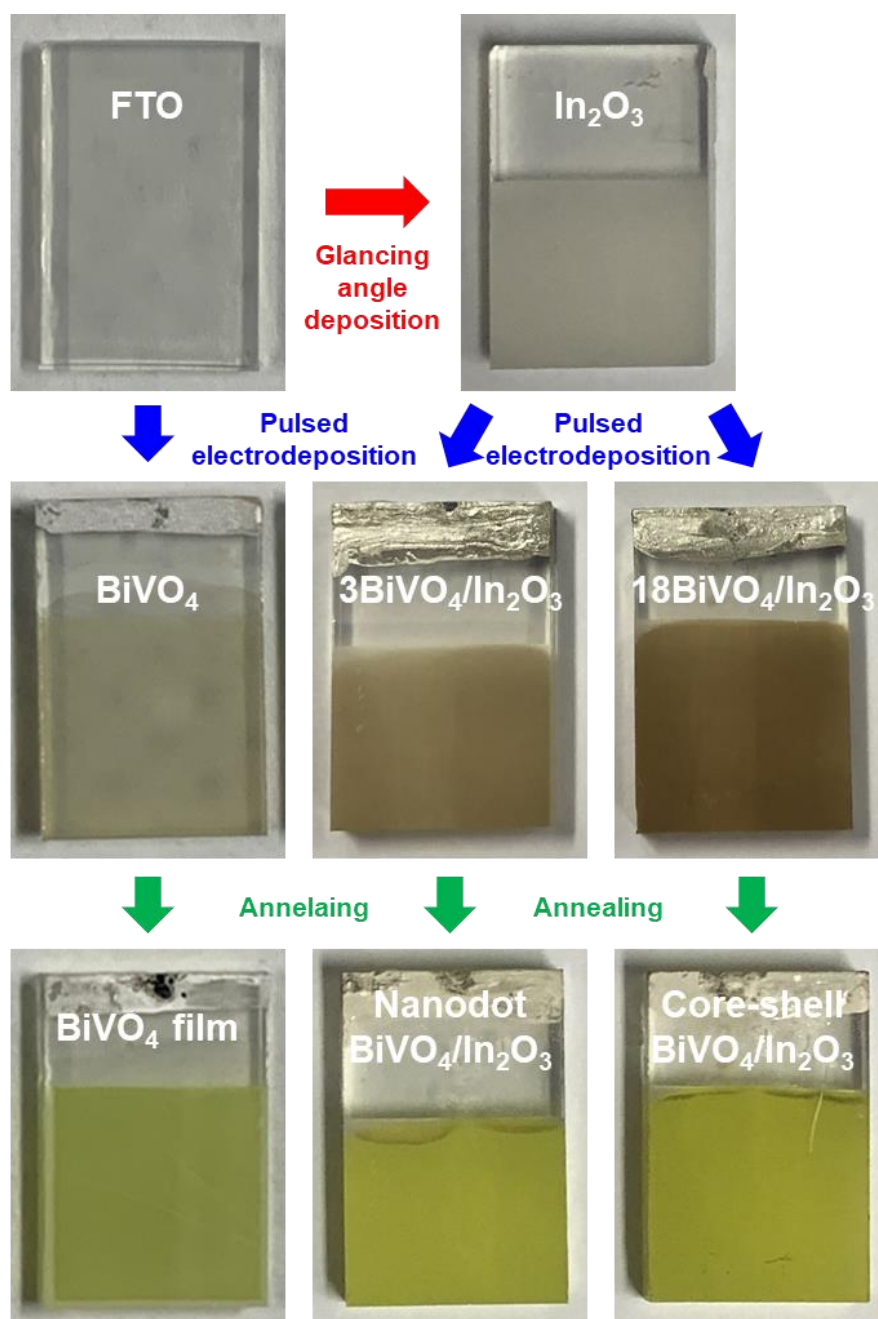
Figure 3.5 Synthetic process and sample photographs of In$_2$O$_3$, BiVO$_4$, and BiVO$_4$/In$_2$O$_3$.

NRs, respectively. Also, as a control group, I fabricated a $BiVO_4$ photoanode through the pulsed electrodeposition with 600 cycles on FTO.

As shown in top SEM images (Figures 3.6A-B), mesopores formed by the GLAD of In_2O_3 are observed in $BiVO_4/In_2O_3$ NRs. In contrast, a dense morphology is shown in the $BiVO_4$ film without nanorods at the bottom (Figure 3.6C). The vertical 1D structures expand the specific surface area,
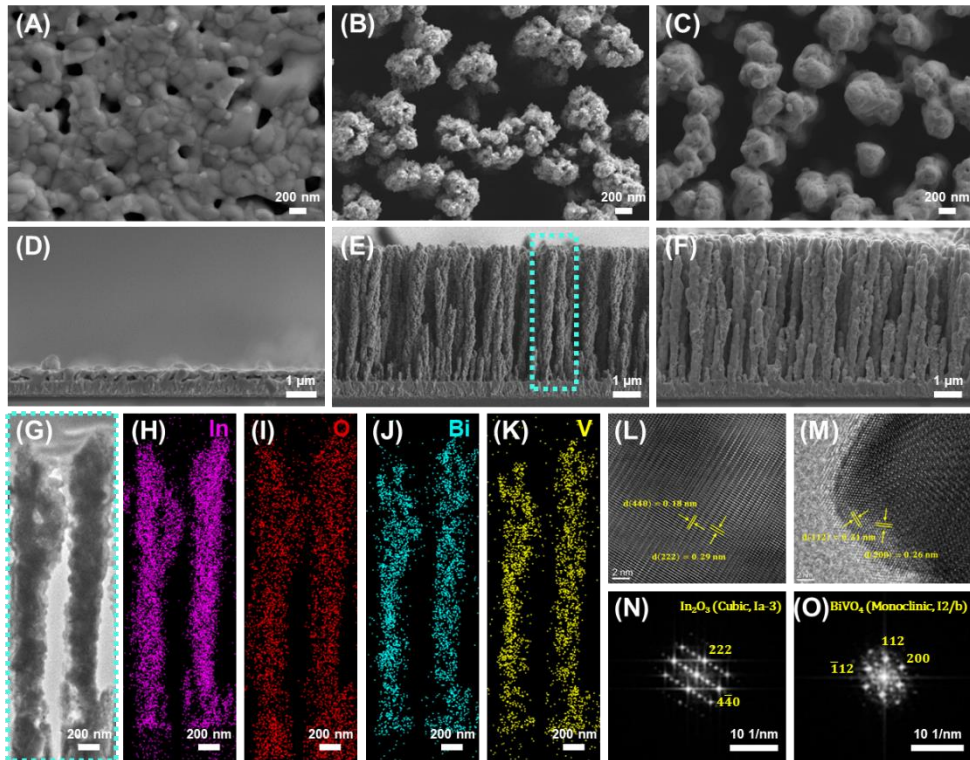
Figure 3.6 Structural characterization. Top SEM images of (A) $BiVO_4$ film, (B) nanodot $BiVO_4/In_2O_3$ NRs, and (C) core-shell $BiVO_4/In_2O_3$ NRs. Cross-sectional SEM images of (D) $BiVO_4$ film, (E) nanodot $BiVO_4/In_2O_3$ NRs, and (F) core-shell $BiVO_4/In_2O_3$ NRs. (G) STEM image of nanodot $BiVO_4/In_2O_3$ NRs. EDS mappings of (H) In, (I) O, (J) Bi, and (K) V. HRTEM images of (L) cubic In_2O_3 and (M) monoclinic $BiVO_4$. FFT patterns of (N) cubic In_2O_3 and (O) monoclinic $BiVO_4$.

and the mesopores facilitate access of the electrolyte to the bottom of the electrode. In the cross-sectional SEM images (Figures 3.6D-F), I confirmed that nanodot $BiVO_4$ was conformally formed on the In_2O_3 NRs and that the bumpy surface of In_2O_3 NRs became smooth when the $BiVO_4$ coverage increased to form a core-shell structure. I emphasize that pulsed electrodeposition easily facilitates to modify the nanoarchitecture of the $BiVO_4/In_2O_3$ NRs through the pulse cycle control. The structure characterization of nanodot $BiVO_4/In_2O_3$ NRs was further conducted by the TEM. The scanning TEM (STEM) image (Figure 3.6G) indicates that nanodot $BiVO_4$ uniformly covers the surface of In_2O_3 NRs. The EDS mappings (Figures 3.6H-K) also showed elemental distributions and the well-synthesized $BiVO_4$ around In_2O_3 NRs. HRTEM images and fast Fourier transform (FFT) patterns are shown in Figures. 3.6L-O. The HR-TEM images and electron diffraction patterns showed d-spacing of 0.18 nm and 0.29 nm, corresponding to the ($4\bar{4}0$) and (222) planes of cubic In_2O_3, respectively, and d-spacing of 0.31 nm and 0.26 nm, which can be assigned to the (112) and (200) planes of monoclinic $BiVO_4$, respectively. These results are well-matched with the XRD analysis, as shown in Figure 3.7.

Both nanodot and core-shell $BiVO_4/In_2O_3$ NRs have cubic In_2O_3 and monoclinic $BiVO_4$ without phase separations.
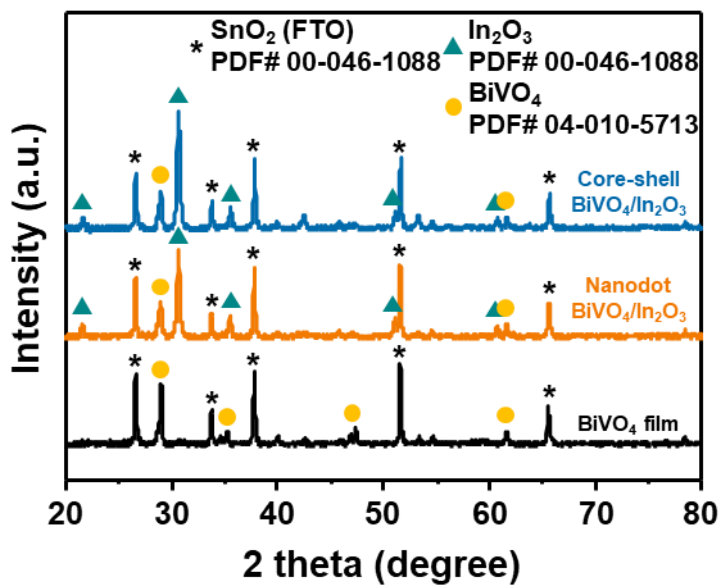
Figure 3.7 XRD of $BiVO_4$ film and $BiVO_4/In_2O_3$ NRs with different morphologies.

3.3.2. Photoelectrochemical performances of BiVO₄/In₂O₃ NRs photoanodes

To closely investigate PEC properties according to the coverage of $BiVO_4$, I measured the LSV of $BiVO_4/In_2O_3$ NRs with different deposition cycles in 0.5 M K-P_i buffer with 1 M Na_2SO_3 under both back-side and front-side 1 sun illumination. As shown in Figure 3.8, photocurrent densities under back-side (J_{back}) and front-side illumination (J_{front}) were recorded as the light was incident on the FTO-side and the $BiVO_4$-side, respectively. Then, as shown
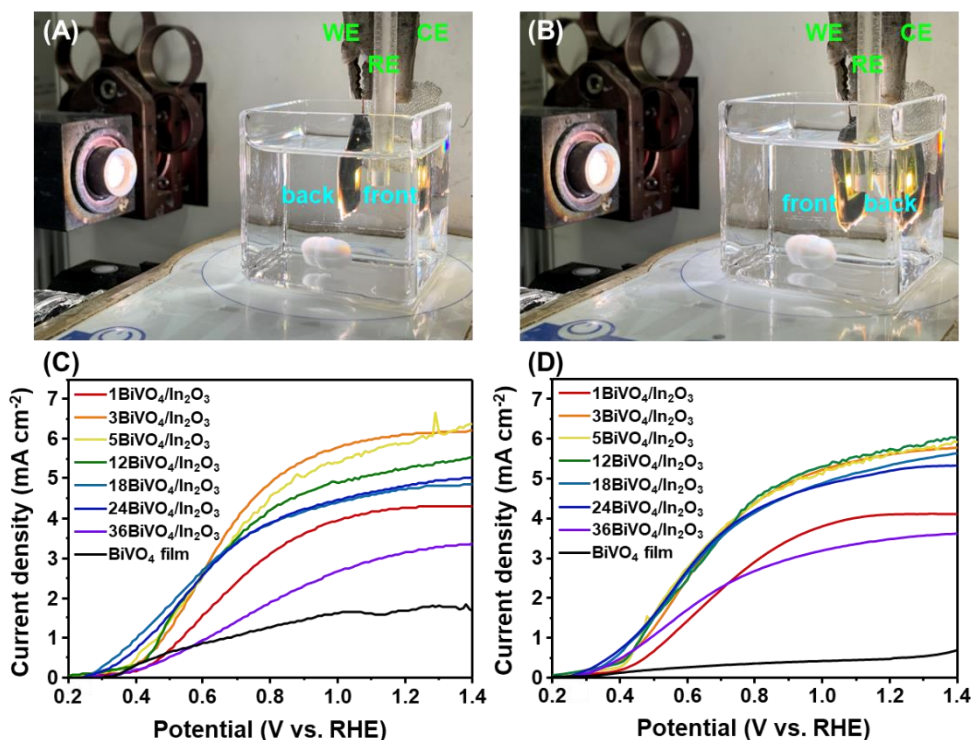
Figure 3.8 *J-V* curves of $BiVO_4/In_2O_3$ NRs with different deposition cycles in 0.5 M K-P_i buffer with 1 M Na_2SO_3 under (A) back-side and (B) front-side 1 sun illumination. Photographs of PEC measurements under (C) back-side and (D) front-side 1 sun illumination.

in Figure 3.9A, I evaluated the J_{back}, J_{front}, and their ratio (J_{back}/J_{front}) at 1.23 V_{RHE} and confirmed 3BiVO$_4$/In$_2$O$_3$ had the highest photoactivity. The J_{back} of the BiVO$_4$/In$_2$O$_3$ NRs increases up to 3 cycles, and then it starts to decrease. Unlike that, the J_{front} was nearly consistent from 3 to 12 cycles, and then it began to decline. In general, the photoactivity difference according to the direction of light irradiation is determined by the mobility and diffusion path of electrons and holes. Under back-side illumination, the photocurrent density is more affected by the diffusion path change of electrons and holes according to the coverage of BiVO$_4$. However, the correlation is weak under front-side illumination, although the morphology transition occurs between 5 cycles and 12 cycles. Through the J_{Back}/J_{Front} ratio and surface morphology in Figure 3.4, I can establish the relationship between the structural distinction and PEC performance. The noticeable point is that nanodot BiVO$_4$/In$_2$O$_3$ NRs from 1 to 5 cycles represented higher photoactivity under back-side illumination, and the J_{Back}/J_{Front} ratio below 1 appeared in the core-shell BiVO$_4$/In$_2$O$_3$ NRs from 12 to 36 cycles. Also, the high J_{Back}/J_{Front} ratio of the BiVO$_4$ film indicates the poor electron diffusion ability of BiVO$_4$ in the film structure since the electron diffusion path becomes shorter under back-side illumination.
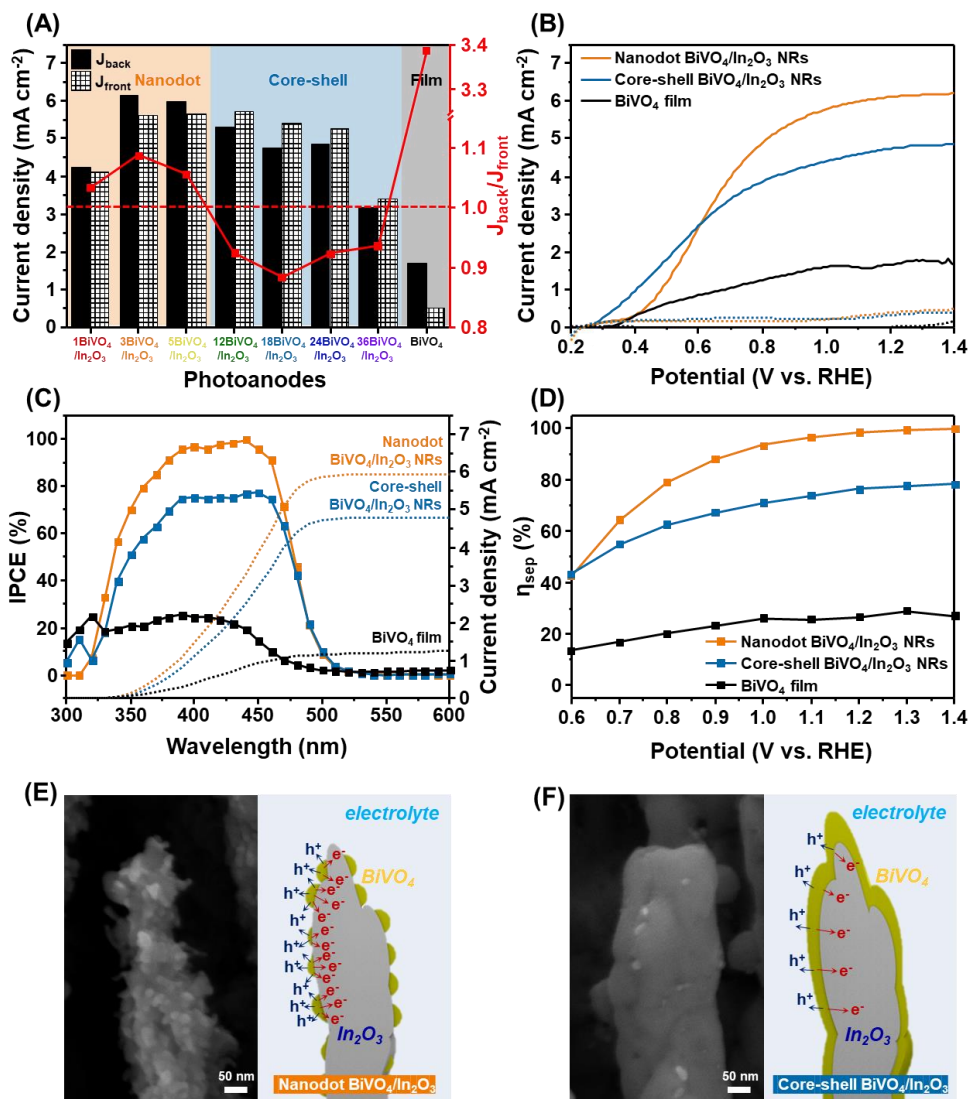
Figure 3.9 PEC sulfite oxidation performances in 0.5 M K-P$_i$ buffer with 1 M Na$_2$SO$_3$ under 1 sun illumination. (A) J_{back}, J_{front}, and their ratio of BiVO$_4$/In$_2$O$_3$ NRs with different deposition cycles of BiVO$_4$ (SOR at 1.23 V$_{RHE}$). (B) J-V curves of nanodot BiVO$_4$/In$_2$O$_3$ NRs, core-shell BiVO$_4$/In$_2$O$_3$ NRs, and BiVO$_4$ film. (C) IPCE at 1.23 V$_{RHE}$ and integrated current density of nanodot BiVO$_4$/In$_2$O$_3$ NRs, core-shell BiVO$_4$/In$_2$O$_3$ NRs, and BiVO$_4$ film. (D) Charge separation efficiencies of nanodot BiVO$_4$/In$_2$O$_3$ NRs, core-shell BiVO$_4$/In$_2$O$_3$ NRs, and BiVO$_4$ film. Cross-sectional SEM images and schematic illustrations about electron-hole transport of (E) nanodot BiVO$_4$/In$_2$O$_3$ NRs and (F) core-shell BiVO$_4$/In$_2$O$_3$ NRs.

113

To scrutinize the photoactivity in the new heterojunction of $BiVO_4$/In_2O_3 NRs with a focus on the nanostructure, an in-depth study for 3 types of photoanodes was processed: (i) nanodot $BiVO_4$/In_2O_3 NRs ($3BiVO_4$/In_2O_3 with highest J_{Back}/J_{Front} ratio), (ii) core-shell $BiVO_4$/In_2O_3 NRs ($18BiVO_4$/In_2O_3 with lowest J_{Back}/J_{Front} ratio), and (iii) $BiVO_4$ film ($600BiVO_4$ as a control group). First, I compared the J-V curves of three photoanodes in 0.5 M K-P_i buffer with 1 M Na_2SO_3 under back-side illumination, as shown in Figure 3.9B. Compared to $BiVO_4$ film, the introduction of In_2O_3 NRs as the ETL for $BiVO_4$ contribute to the significant increase in the photocurrent density of $BiVO_4$/In_2O_3 NRs photoanode regardless of their morphologies. This is because 1D vertical nanorods are favorable to the electron transport to the axial direction and hole transport to the radial direction, resulting in significantly suppressed charge recombination [17,36,37]. Especially, the nanodot $BiVO_4$/In_2O_3 NRs appeared to have a high photocurrent density of 6.1 mA cm^{-2} at 1.23 V_{RHE}, which is 1.2-fold higher than that of core-shell $BiVO_4$/In_2O_3 NRs (4.9 mA cm^{-2} at 1.23 V_{RHE}) and 3.6-fold higher than that of $BiVO_4$ films (1.7 mA cm^{-2} at 1.23 V_{RHE}).

These distinctions were also confirmed by the IPCE at 1.23 V_{RHE}, as shown in Figure 3.9C. Compared to $BiVO_4$ film, both nanodot and core-shell

BiVO$_4$/In$_2$O$_3$ NRs photoanodes show significant enhancement of conversion efficiency. Reliable IPCE values were measured up to 500 nm for BiVO$_4$ film as well as BiVO$_4$/In$_2$O$_3$ NRs, which indicated that BiVO$_4$ has a band gap of 2.48 eV regardless of the morphology. Also, the IPCE trends are well-matched with the photoactivity of the nanostructures. The integrated photocurrent densities of nanodot BiVO$_4$/In$_2$O$_3$ NRs, core-shell BiVO$_4$/In$_2$O$_3$ NRs, and BiVO$_4$ film are 6.0 mA cm^{-2}, 4.8 mA cm^{-2}, and 1.3 mA cm^{-2}, respectively, which correspond the photocurrent density in J-V curves (Figure 3.9B). I estimated that the superior PEC performance of nanodot BiVO$_4$/In$_2$O$_3$ NRs was imparted by improved charge separation and light absorption efficiency [17,36-38]. As shown in Figure 3.9D, the nanodot BiVO$_4$/In$_2$O$_3$ NRs showed a higher charge separation efficiency compared to that of the core-shell BiVO$_4$/In$_2$O$_3$ NRs photoanode. At near the 1.23 V$_{RHE}$, it appeared to be a near-complete charge separation (η_{sep} = 99%), unlike that of core-shell BiVO$_4$/In$_2$O$_3$ NRs photoanode (η_{sep} = 77%). It can be said that distinct morphology differences between nanodot and core-shell structures affect PEC characteristics. So, I analyzed cross-sectional FESEM images with a high resolution and illustrated the schematics of nanodot BiVO$_4$/In$_2$O$_3$ NRs (Figure 3.9E) and core-shell BiVO$_4$/In$_2$O$_3$ NRs (Figure 3.9F). Compared to core-shell structure, BiVO$_4$ nanodots conformally coated on In$_2$O$_3$ NRs can expand the specific surface area and increase the active

surface sites, extending the contact with the electrolyte. Furthermore, in nanodots below 50 nm, the diffusion paths to the electrolyte/$BiVO_4$ and the $BiVO_4$/In_2O_3 interfaces are reduced below the charge diffusion length of $BiVO_4$ (~70 nm), contributing to preventing charge recombination. In other words, the $BiVO_4$ nanodots in intimate contact with In_2O_3 NRs are favorable to have higher charge collection efficiency than the core-shell structure [30,31,38,39].

3.3.3. Charge carrier dynamics and band structures of BiVO$_4$/In$_2$O$_3$ NRs photoanodes

To more clearly demonstrate the charge carrier dynamics for BiVO$_4$-based photoanodes, I calculated the charge carrier concentrations of BiVO$_4$-based photoanodes from M-S plots in light off, as shown in Figure 3.10A. The carrier concentration can be calculated from the slopes of the M-S plots. As the slope gets gradual, the carrier concentration increases [39,40]. Even though the flat band potentials of the BiVO$_4$/In$_2$O$_3$ NRs photoanodes are more negatively shifted than that of the BiVO$_4$ film photoanode, their slopes are more gradual than that of the BiVO$_4$ film photoanode. I calculated the carrier concentrations of BiVO$_4$-based photoanodes, as listed in Table 3.1. The introduction of vertical 1D In$_2$O$_3$ NRs as the ETL surged the carrier density of BiVO$_4$/In$_2$O$_3$ NRs photoanodes compared to that of the BiVO$_4$ film (2.694×10^{19} cm^{-3}).[21] The M-S plots also manifest that the carrier concentration of 4.085×10^{22} cm^{-3} in the nanodot BiVO$_4$/In$_2$O$_3$ NRs is higher than that of 9.804×10^{21} cm^{-3} in the core-shell BiVO$_4$/In$_2$O$_3$ NRs. These results have a thread of connection with the structural characterization of BiVO$_4$/In$_2$O$_3$ NRs photoanodes in Figures 3.6E-F. In order to quantitatively understand these differences, I conducted a double-layer capacitance (C_{dl})

measurement through the CV of the BiVO₄-based photoanodes, as shown in
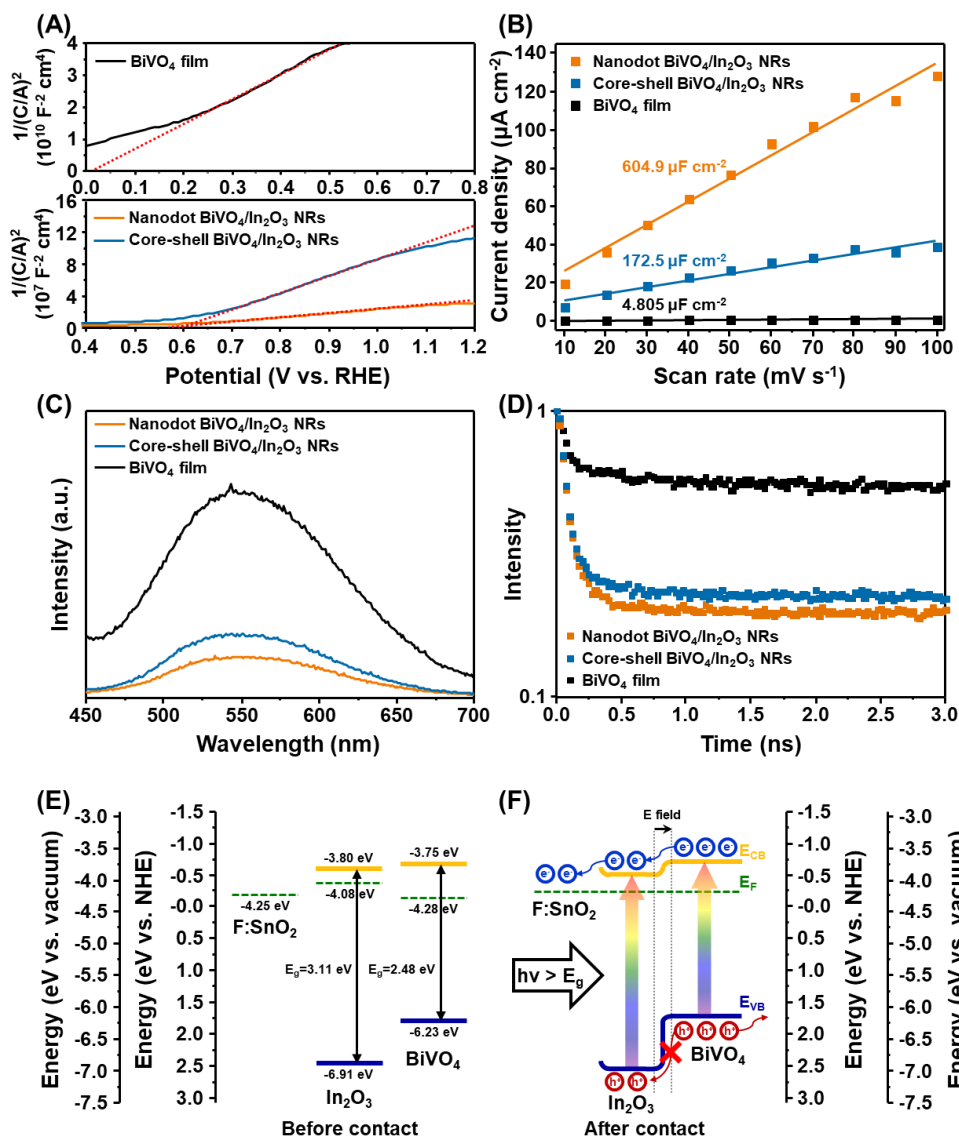
Figure 3.10 Charge carrier dynamics and band structures. (A) M-S plots and (B) ECSA plots of nanodot BiVO₄/In₂O₃ NRs, core-shell BiVO₄/In₂O₃ NRs, and BiVO₄ film in 0.5 M K-P$_i$ buffer with 1 M Na₂SO₃ under dark condition. (C) PL spectra and (D) TRPL at 550 nm of nanodot BiVO₄/In₂O₃ NRs, core-shell BiVO₄/In₂O₃ NRs, and BiVO₄ film. Energy band diagrams of BiVO₄/In₂O₃ NRs (E) before and (F) after contact.

Figure 3.11. The ECSA is regarded as an estimation of active sites, and it is proportional to C_{dl}. At the fitted lines in Figure 3.10B, the C_{dl} of nanodot $BiVO_4/In_2O_3$ NRs (604.9 µF cm^{-2}) showed the highest value compared to those of core-shell $BiVO_4/In_2O_3$ NRs (172.5 µF cm^{-2}) and $BiVO_4$ film (4.805 µF cm^{-2}). This result represents that the nanodot $BiVO_4/In_2O_3$ NRs provide a larger electrochemically active surface area than the core-shell $BiVO_4/In_2O_3$ NRs and that the increased surface area has a crucial role in enhancing the PEC performances.

Table 3.1 Carrier concentrations of photoanodes calculated by M-S plots.

Photoanodes	N_D [10^{19} cm^{-3}]
$BiVO_4$ film	2.694
Nanodot $BiVO_4/In_2O_3$ NRs	4085
Core-shell $BiVO_4/In_2O_3$ NRs	980.4
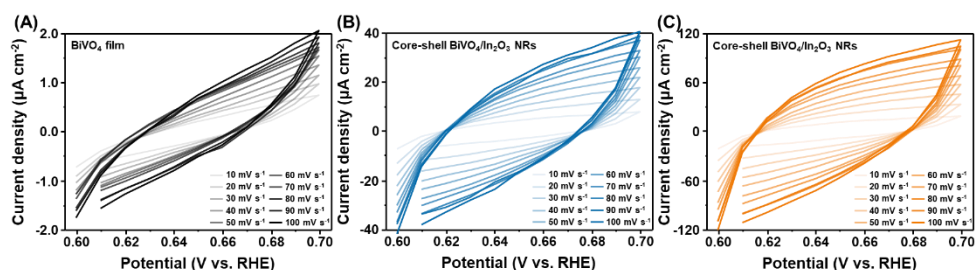
Figure 3.11 CV curves according to scan rates of (A) $BiVO_4$ film, (B) core-shell $BiVO_4/In_2O_3$ NRs, and (C) nanodot $BiVO_4/In_2O_3$ NRs in 0.5 M K-P$_i$ buffer with 1 M Na_2SO_3 under dark condition.

To further examine charge separation and recombination behaviors of BiVO$_4$-based photoanodes, I investigated by steady-state photoluminescence (PL) spectra (Figure 3.10C). The PL emissions of BiVO$_4$-based photoanodes were observed at 543 nm regardless of catalyst types, and this wavelength was close to the absorption edge of BiVO$_4$ (Figure 3.12A). Therefore, this emission peak represents radiative recombination from holes in the O 2p band to electrons in V 3d band [41], which correlates to the charge recombination ability. Especially, the pristine BiVO$_4$ film exhibited a very strong PL peak, demonstrating the high electron-hole recombination. However, after introducing the In$_2$O$_3$ NRs, the intensity of the PL peak was evidently reduced. It indicates that the heterojunction of BiVO$_4$/In$_2$O$_3$ NRs enables spontaneous electron transport and hole blocking (hole mirror) [12,42-45]. Of note, the PL intensity in the
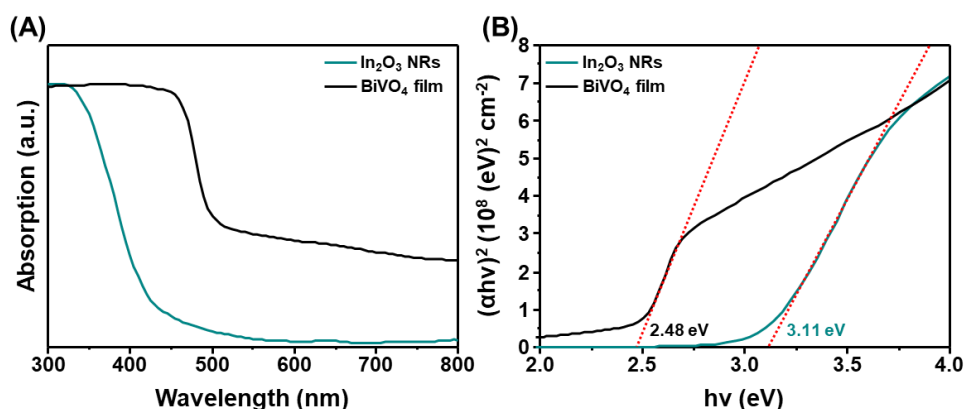
Figure 3.12 (A) UV-vis absorption spectra and (B) Tauc plots of In$_2$O$_3$ NRs and BiVO$_4$ film.

nanodot structure nanodot showed a lower value than that in the core-shell structure, suggesting that the charge recombination was further inhibited in the nanodot $BiVO_4/In_2O_3$ NRs photoanode. This result was in line with the morphological analysis, as mentioned in the previous contents (Figures 3.9E-F). Then, I further evaluated charge carrier lifetimes of nanodot $BiVO_4/In_2O_3$ NRs, core-shell $BiVO_4/In_2O_3$ NRs, and $BiVO_4$ film by the time-resolved PL (TRPL) at 543 nm, which was attributed to carrier dynamics, as shown in Figure 3.10D. The decay curves were matched with the bi-exponential fitting model, as shown in Table 3.2. The faster decay constant (τ_1) is attributed to non-radiative recombination, while the slower decay constant (τ_2) originated from radiative recombination [46]. Specifically, the non-radiative recombination lifetime (τ_1) is generally determined from the surface recombination by the trap sites. Since $BiVO_4$-based photoanodes have the same $BiVO_4$ that the part in contact with the electrolyte on the band structures, they have similar τ_1 values (0.11-0.12 ns). However, the radiative recombination lifetime (τ_2) largely decreased from 4.55 ns to 2.61 ns after introducing the In_2O_3 NRs as the ETL since it enables efficient extraction of photoexcited electrons by In_2O_3 NRs. Notably, the shorter lifetime of nanodot $BiVO_4/In_2O_3$ NRs demonstrates the more enhanced charge transport, which is ascribed to the small dimension of

BiVO$_4$ nanodots (Figures 3.9E-F) [42,47]. These results are consistent with the charge separation efficiency, as shown in Figure 3.9D.

Table 3.2. Non-radiative TRPL lifetime (τ_1) and radiative TRPL lifetime (τ_2) of photoanodes.

Photoanodes	τ_1 [ns]	τ_2 [ns]
BiVO$_4$ film	0.12	4.55
Nanodot BiVO$_4$/In$_2$O$_3$ NRs	0.12	2.61
Core-shell BiVO$_4$/In$_2$O$_3$ NRs	0.11	3.26

Combining the morphological analysis and charge carrier dynamics, the smaller diffusion path of the nanodot structure compared to the core-shell structure caused higher charge separation, which in turn led to a higher carrier concentration leading to superior photocurrent density of nanodot BiVO$_4$/In$_2$O$_3$ NRs photoanode. That is, it emphasizes that optimizing the nanostructure is essential to promoting PEC performances.

To further elucidate the effect of the In$_2$O$_3$ NRs and subsequently confirm the crucial reason for the improved PEC activity of BiVO$_4$/In$_2$O$_3$ NRs, I analyzed the band structures based on ultraviolet-visible (UV-vis) spectroscopy and ultraviolet photoelectron spectroscopy (UPS). Here, the core-shell structure was used to obtain exact values of BiVO$_4$ on In$_2$O$_3$ NRs, since the surface is completely covered with BiVO$_4$. According to Tauc plots

(Figure 3.12B) derived from UV-vis absorption spectra (Figure 3.12A), $BiVO_4$ film and In_2O_3 NRs have optical band gaps of 2.48 eV and 3.11 eV, respectively. As shown in Figure 3.13, I analyzed the UPS of In_2O_3 NRs, $BiVO_4$ film, and $BiVO_4/In_2O_3$ NRs and listed the Fermi energy (E_F) and the energy difference between Fermi level and valence band (E_F-E_{VBM}) at Table 3.3. Based on these values, I derived flat band energy diagrams of $BiVO_4/In_2O_3$ NRs (Figure 3.10E). I first discovered that the $BiVO_4$ and In_2O_3 formed type II heterojunction with a cascade band alignment, which is favorable for electron transport and hole blocking, as shown in Figure 3.10F. Moreover, the impressive role of In_2O_3 NRs for $BiVO_4$ was confirmed by comparing with other type II band structures, which were previously reported in our group, as shown in Figure 3.14 [17,20,21,48].
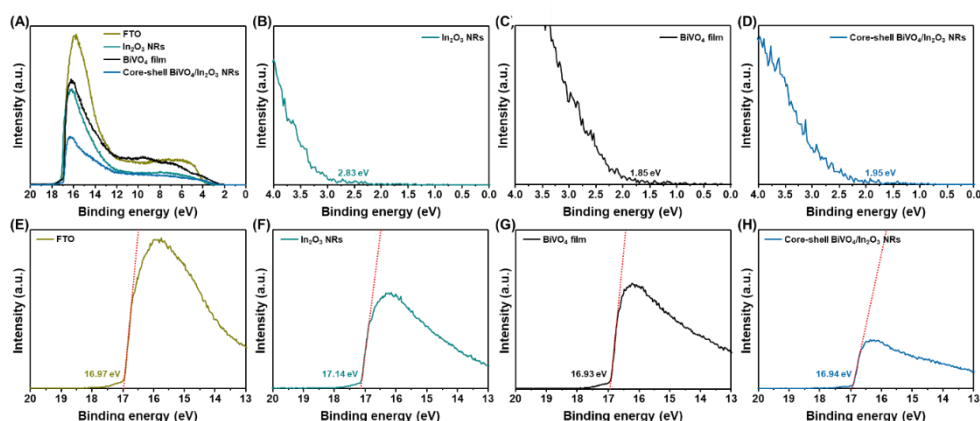
Figure 3.13 (A) The wide scan of ultraviolet photoelectron spectra (UPS). The valence band (VB) spectra of (B) In_2O_3 NRs, (C) $BiVO_4$ film, and (D) $18BiVO_4/In_2O_3$ NRs. $E_{VBM} = E_F–E_{edge}$. The secondary electron emission (SEE) spectra and cut-off energy of (E) FTO, (F) In_2O_3 NRs, (G) $BiVO_4$ film, and (H) $18BiVO_4/In_2O_3$ NRs. $E_F = E_{cut-off}$ -21.22 eV (He I photon source).

123

Among three ETLs, In_2O_3 NRs contribute to generating the highest photocurrent density at 1.23 V_{RHE}. These results can also be supported by the PEC properties of film-type photoanodes, as shown in Figure 3.15. Despite the absence of nanostructures, $BiVO_4/In_2O_3$ film photoanodes recorded 1.5 and 5.3 times enhanced photocurrent density at 1.23 V_{RHE} compared to $BiVO_4$ film photoanode under back-side and front-side 1 sun illumination, respectively. It indicates that In_2O_3 has excellent potential to replace the current ETLs for $BiVO_4$, such as WO_3 and SnO_2.

Table 3.3 (A) Fermi energy (E_F) and the energy difference between Fermi level and valence band (E_F-E_{VBM}) of photoanodes. (B) Optical band gaps of photoanodes.

(A)

Materials	E_F [eV]	E_F-E_{VBM} [eV]
FTO	4.25	N/A
In_2O_3 NRs	4.08	2.83
$BiVO_4$ film	4.29	1.95
$BiVO_4/In_2O_3$ NRs	4.28	1.85

(B)

Materials	E_g [eV]
In_2O_3 NRs	3.11
$BiVO_4$ film	2.48
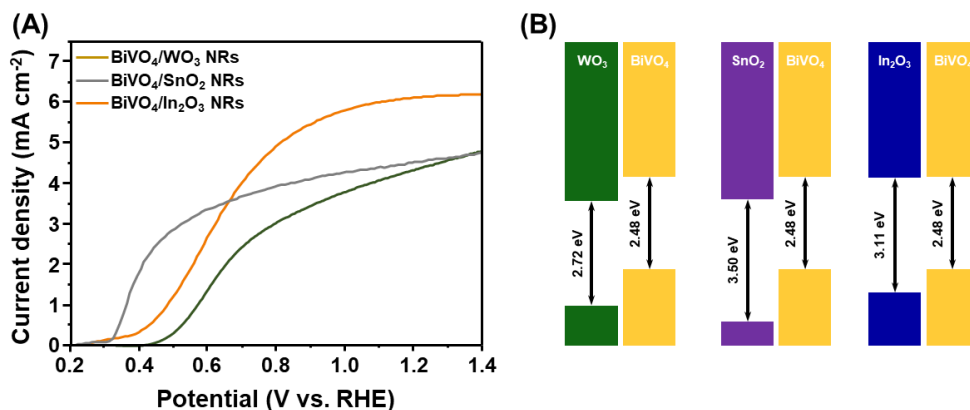
Figure 3.14 Comparison with different electron transport layers for BiVO$_4$. (A) *J-V* curves of BiVO$_4$/WO$_3$ NRs, BiVO$_4$/SnO$_2$ NRs, and BiVO$_4$/In$_2$O$_3$ NRs in 0.5 M K-P$_i$ buffer with 1 M Na$_2$SO$_3$ under 1 sun illumination. (Our groups' records) (B) Flat band structures of BiVO$_4$/WO$_3$ NRs, BiVO$_4$/SnO$_2$ NRs, and BiVO$_4$/In$_2$O$_3$ NRs.
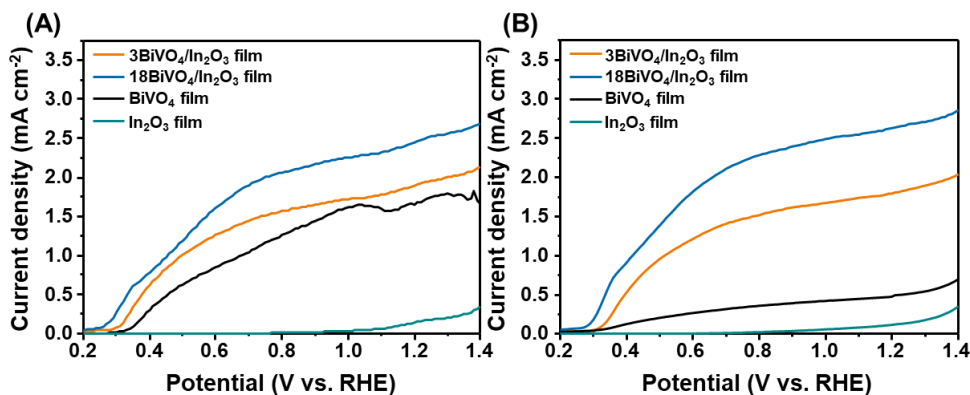
Figure 3.15 *J-V* curves of In$_2$O$_3$ film, BiVO$_4$ film, BiVO$_4$/In$_2$O$_3$ film in 0.5 M K-P$_i$ buffer with 1 M Na$_2$SO$_3$ under (A) back-side and (B) front-side 1 sun illumination.

3.3.4. Photoelectrochemical Performances of TANF/BiVO$_4$/In$_2$O$_3$ NRs Photoanodes

To further improve the PEC performances of nanodot BiVO$_4$/In$_2$O$_3$ NRs by expediting the interfacial hole transfer of BiVO$_4$ into the water, I introduced a transition metal-based OEC composed of tannic acid (TA), Ni, and Fe ions (denoted as TANF). As shown in STEM image and EDS mappings (Figure 3.16), TANF enables the intact and uniform coating on the entire surface of nanodot BiVO$_4$/In$_2$O$_3$ NRs, and it forms a triple junctional photoanode denoted as TANF/BiVO$_4$/In$_2$O$_3$ NRs. As a chelating agent, TA can bind to diverse metal ions and form uniform and intimate film, which effectively protects the surface of the photoanode [24,49].
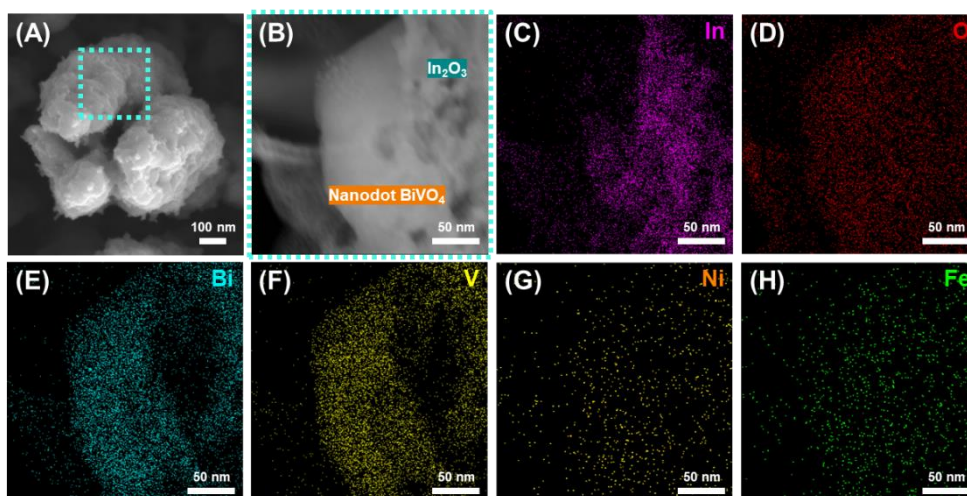
Figure 3.16 Structural characterization of TANF/BiVO$_4$/In$_2$O$_3$ NRs. (A) Top SEM image and (B) STEM image of TANF/BiVO$_4$/In$_2$O$_3$ NRs. EDS mappings of (C) In, (D) O, (E) Bi, (F) V, (G) Ni, and (H) Fe.

As shown in Figure 3.17, I first evaluated the photoactivities of TANF/BiVO$_4$/In$_2$O$_3$ NRs according to the dipping time in the TANF solution. Beyond the optimal coating time, thick TANF layer on the surface block the light absorption to BiVO$_4$/In$_2$O$_3$ NRs, causing the current drops. In sulfite oxidation, the optimized TANF/BiVO$_4$/In$_2$O$_3$ NRs photoanode with a dipping time of 2 h showed a remarkable photocurrent density of 7.1 mA cm^{-2} at 1.23 V$_{RHE}$, which is a 15% increase over that of BiVO$_4$/In$_2$O$_3$ NRs photoanode (Figure 3.18A). Also, the TANF/BiVO$_4$/In$_2$O$_3$ NRs photoanode showed good reproducibility with consistent photocurrent densities of 7.1 $\pm$ 0.3 mA cm^{-2} at 1.23 V$_{RHE}$, as shown in Figure 3.18B.
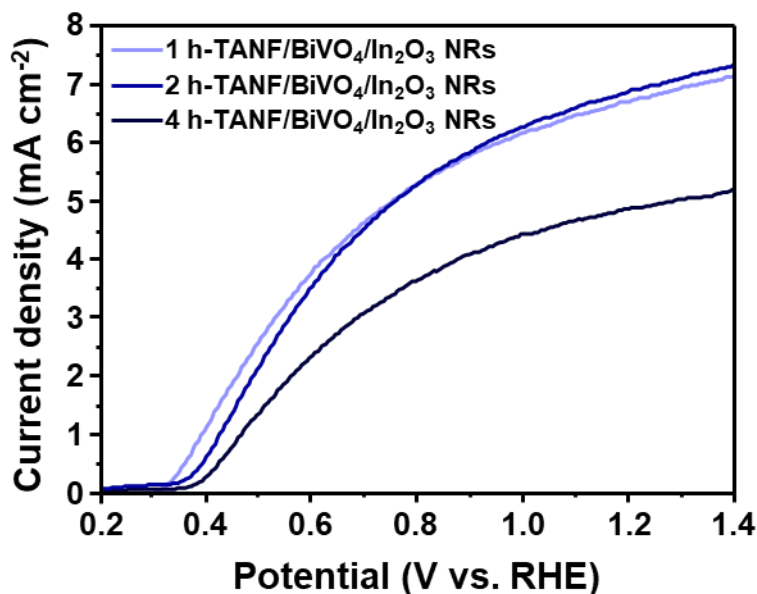
Figure 3.17 *J-V* curves of TANF/BiVO$_4$/In$_2$O$_3$ NRs with different dipping times in TANF solution in 0.5 M K-P$_i$ buffer with 1 M Na$_2$SO$_3$ under back-side 1 sun illumination.

Furthermore, the TANF/BiVO₄/In₂O₃ NRs photoanode exhibits outstanding stability since TANF enables intact and uniform coating at the surface and effectively prevents the direct contact of BiVO₄/In₂O₃ NRs with electrolyte. As shown in Figure 3.19, the photocurrent density was consistent in 10 hour-running test without change in crystal structure and morphology, unlike
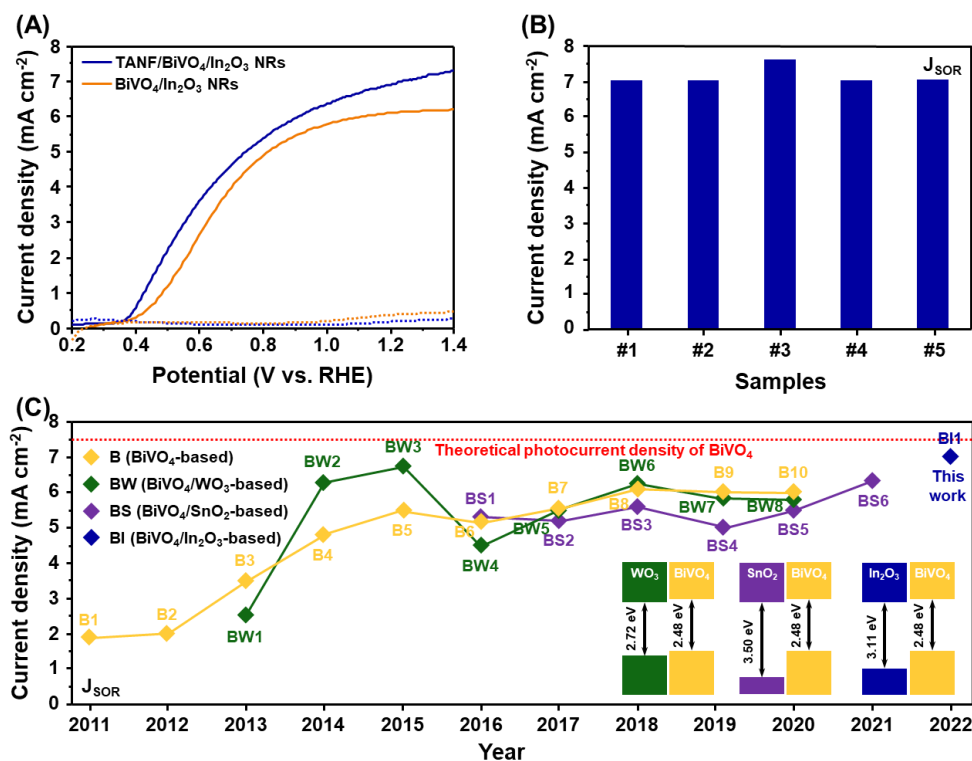
Figure 3.18 PEC sulfite oxidation performances in 0.5 M K-P$_i$ buffer with 1 M Na₂SO₃ under 1 sun illumination. (A) *J-V* curves of TANF/BiVO₄/In₂O₃ NRs and BiVO₄/In₂O₃ NRs. (B) Reproducibility of TANF/BiVO₄/In₂O₃ NRs (SOR at 1.23 V$_{RHE}$). (C) Photocurrent density benchmark of BiVO₄-based photoanodes reported over the past 10 years (SOR at 1.23 V$_{RHE}$, reference lists: B1 [52], B2 [53], B3 [54], B4 [23], B5 [55], B6 [3], B7 [56], B8 [57], B9 [18], B10 [58], BW1 [59], BW2 [60], BW3 [61], BW4 [17], BW5 [62], BW6 [21], BW7 [63], BW8 [28], BS1 [64], BS2 [8], BS3 [48], BS4 [65], BS5 [66], and BS6 [51]).

agglomerated BiVO$_4$/In$_2$O$_3$ NRs without TANF. According to the photocurrent density benchmark of BiVO$_4$-based photoanodes reported over the past 10 years (Figure 3.18C), the photocurrent densities of not only single BiVO$_4$-based photoanodes but also BiVO$_4$-based heterojunction photoanodes with the ETL have been saturated below the limiting value. I anticipate that the introduction of In$_2$O$_3$ as a new and effective ETL will become a breakthrough in achieving the photocurrent density of 7 mA cm^{-2} or more since I already recorded this value under sulfite oxidation. As a
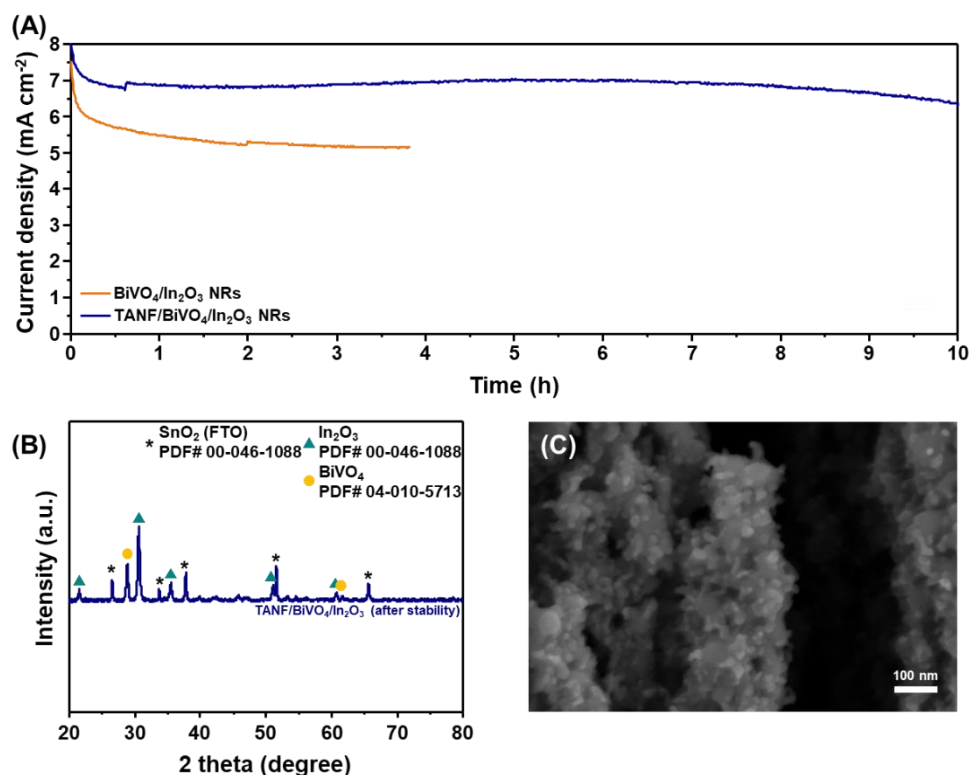
Figure 3.19 (A) *J-t* curves of BiVO$_4$/In$_2$O$_3$ NRs with and without TANF at 1.23 V$_{RHE}$ in 0.5 M K-P$_i$ buffer with 1 M Na$_2$SO$_3$ under back-side 1 sun illumination. (B) XRD and (C) cross-sectional SEM of TANF/BiVO$_4$/In$_2$O$_3$ NRs after 10 hour-running test.

starting point of In_2O_3-based ETL, by researching the ETL based on ternary oxides with additional doping, photoanodes with a photocurrent density nearly close to the theoretical value of $BiVO_4$ will be developed.

To further verify the effect of TANF as an OEC, I evaluated the PEC water oxidation performances of $BiVO_4/In_2O_3$ NRs photoanode with and without TANF in 1 M K-B_i buffer. In water oxidation, PEC properties such as onset potential, photocurrent, and stability deteriorated due to the poor OER kinetics of $BiVO_4$. However, after uniform coating of TANF, the TANF/$BiVO_4/In_2O_3$ NRs photoanode cathodically shifts the onset potential and generates a photocurrent density of 4.2 mA cm^{-2} at 1.23 V_{RHE}, which is a 16.6 times improvement over that of $BiVO_4/In_2O_3$ NRs photoanode, as shown in Figure 3.20A. I also evaluated the STH conversion efficiency, which is a practical standard for accessing PEC performance. Considering a half-cell OER in photoanode (three-electrode configuration), the ABPE was applied to $BiVO_4$-based photoanodes. To characterize the ABPE, I first check the Faradaic efficiency of around 100%, indicating that the photogenerated charges are effectively used in the oxygen evolution without dominant charge loss. The ABPE of the TANF/$BiVO_4/In_2O_3$ NRs photoanode was considerably higher than that of the $BiVO_4/In_2O_3$ NRs

photoanode regardless of the voltage, and it reached a maximum value of 1.43% at 0.72 V, as shown in Figure 3.20B.

To further examine the effect of TANF on improved water oxidation activity, I employed EIS to evaluate the charge transfer ability during the water splitting reaction, as shown in Figure 3.20C. The measured EIS Nyquist plots were fitted to the equivalent circuit (Figure 3.21A). Since the charges generated in the photoanode undergo bulk recombination and surface recombination, the equivalent circuit with several resistors was used to distinguish them. R_s is a series resistance at the interface between FTO and photoanodes. R_{sc} is a bulk resistance in photoanodes, and CPE_{sc} means
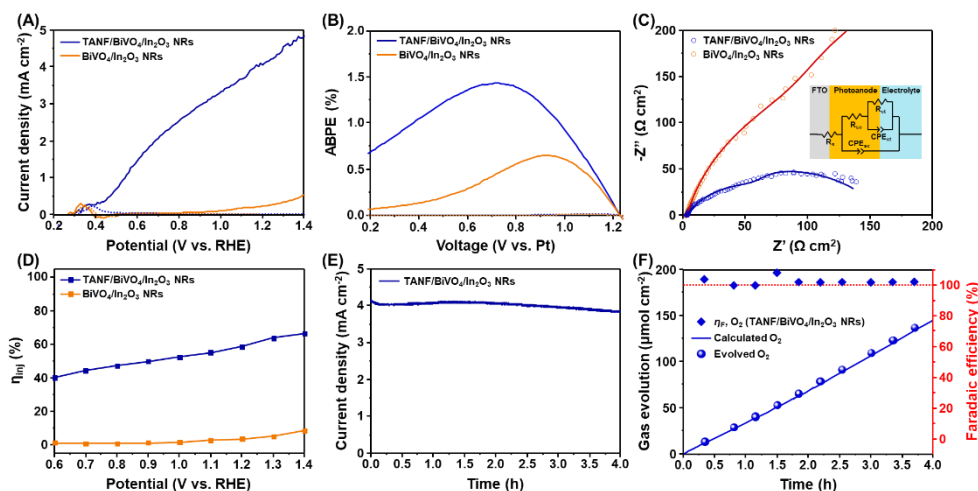
Figure 3.20 PEC water oxidation performances in 1 M K-B$_i$ buffer under 1 sun illumination. (A) *J-V* curves of TANF/BiVO$_4$/In$_2$O$_3$ NRs and BiVO$_4$/In$_2$O$_3$ NRs. (B) ABPE of TANF/BiVO$_4$/In$_2$O$_3$ NRs and BiVO$_4$/In$_2$O$_3$ NRs. (C) EIS Nyquist plots at 1.23 V$_{RHE}$ of TANF/BiVO$_4$/In$_2$O$_3$ NRs and BiVO$_4$/In$_2$O$_3$ NRs. (D) Charge injection efficiencies of TANF/BiVO$_4$/In$_2$O$_3$ NRs and BiVO$_4$/In$_2$O$_3$ NRs. (E) *J-t* curve, (F) Faradaic efficiency and gas evolution at 1.23 V$_{RHE}$ of TANF/BiVO$_4$/In$_2$O$_3$ NRs.

their accompanying capacity. Also, R_{ct} is a charge transfer resistance at the interface between photoanodes and electrolytes, and CPE_{ct} is the constant phase element that represents the dielectrics of the electrical double layer at the electrode/electrolyte interfaces. The smaller semicircle of the EIS Nyquist plot represents the better charge carrier kinetics [39,50].

The EIS Bode plots are represented in Figure 3.21B. TANF/BiVO$_4$/In$_2$O$_3$ NRs showed a lower resistance and phase angle than BiVO$_4$/In$_2$O$_3$ NRs. As listed in Table 3.4, TANF/BiVO$_4$/In$_2$O$_3$ NRs had the lower R_{sc} of 112.8 Ω
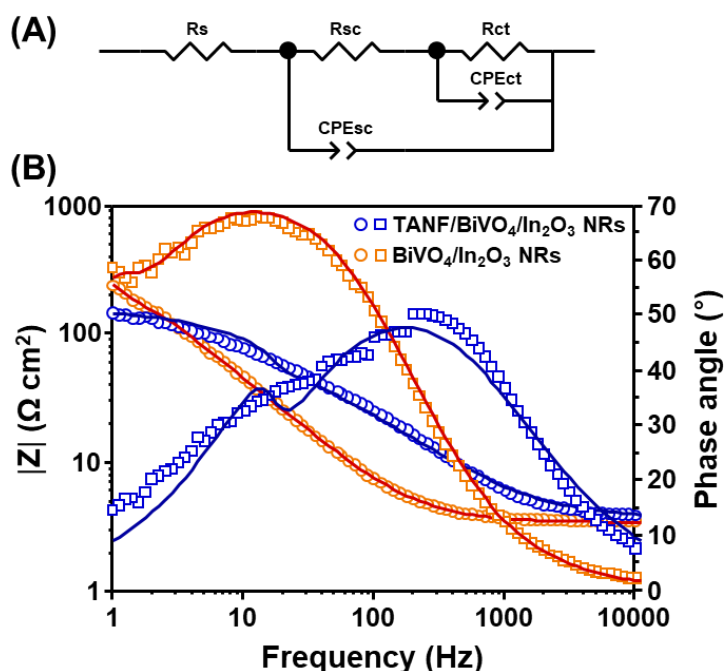
Figure 3.21 EIS equivalent circuits for (A) BiVO$_4$/In$_2$O$_3$ NRs and TANF/BiVO$_4$/In$_2$O$_3$ NRs. (B) EIS Bode plots at 1.23 V$_{RHE}$ of TANF/BiVO$_4$/In$_2$O$_3$ NRs and BiVO$_4$/In$_2$O$_3$ NRs: modulus plots (circle symbols) and phase angle plots (square symbols).

cm^2, compared to that of BiVO$_4$/In$_2$O$_3$ NRs (438.2 Ω cm^2), which means more favorable charge transport. Also, for the charge transfer resistance, TANF/BiVO$_4$/In$_2$O$_3$ NRs had the lower R_{ct} of 44.77 Ω cm^2, compared to that of BiVO$_4$/In$_2$O$_3$ NRs (207.2 Ω cm^2). This result represents the effective charge transfer in the TANF/BiVO$_4$/In$_2$O$_3$ photoanode by suppressing the charge recombination and reducing the charge transfer resistance between the semiconductor and electrolyte [50].

Table 3.4 Series resistances (R_s), bulk resistances (R_{sc}), charge transfer resistances (R_{ct}), and chi-squared values (X^2) fitted from EIS curves.

Materials	R_s [Ω cm^2]	R_{sc} [Ω cm^2]	R_{ct} [Ω cm^2]	X^2
BiVO$_4$/In$_2$O$_3$ NRs	3.373	438.2	207.2	5.113E-3
TANF/BiVO$_4$/In$_2$O$_3$ NRs	2.914	112.8	44.77	9.131E-3

I also calculated the charge injection efficiency for BiVO$_4$/In$_2$O$_3$ NRs and TANF/BiVO$_4$/In$_2$O$_3$ NRs, as shown in Figure 3.20D. In the entire range of potential, the charge injection efficiency is significantly increased from 4% to 60% at 1.23 V$_{RHE}$, demonstrating that the more efficient hole transfer to the surface after the introduction of TANF as an OEC layer. The uniform coating of TANF contributes to suppressing the photocorrosion by preventing the dissolution of V^{5+} to the electrolyte. As shown in chronoamperometry at 1.23 V$_{RHE}$, the TANF/BiVO$_4$/In$_2$O$_3$ NRs photoanode

showed an operation duration of 4 h without the performance decay (Figure 3.20E). To directly confirm the OER, I measured the gas evolution and Faradaic efficiency of TANF/BiVO$_4$/In$_2$O$_3$ NRs at 1.23 V$_{RHE}$ by using gas chromatography. As shown in Figure 3.20F, oxygen gas were continuously detected at the TANF/BiVO$_4$/In$_2$O$_3$ NRs photoanode. The Faradaic efficiencies approaching 100% represent the complete conversion of the photogenerated charge carriers to the evolution of oxygen gas.

3.3.5. Unbiased solar water splitting PV-PEC tandem cell

Finally, I implement unbiased PEC water splitting by fabricating an "artificial leaf" consisting of the TANF/BiVO$_4$/In$_2$O$_3$ NRs photoanode and a perovskite/Si solar cell, as illustrated in Figure 3.22A. The performances of the perovskite/Si solar cell are represented in Figure 3.23 and Table 3.5. The two-electrode J-V curve for TANF/BiVO$_4$/In$_2$O$_3$ photoanode was measured under the 1 sun illumination, and that of the perovskite/Si solar
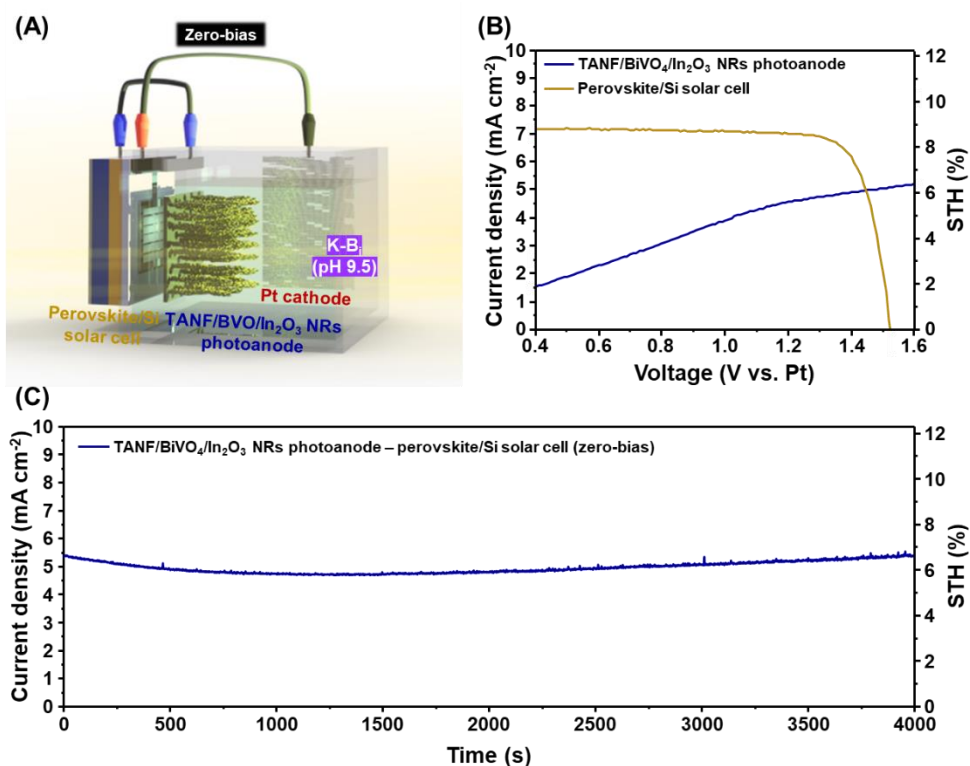
Figure 3.22 Unbiased solar water splitting PV-PEC tandem cell in 1 M K-B$_i$ buffer under 1 sun illumination. (A) Schematic illustration of the PV-PEC tandem cell with TANF/BiVO$_4$/In$_2$O$_3$ NRs photoanode and perovskite/Si solar cell. (B) J-V curves of TANF/BiVO$_4$/In$_2$O$_3$ NRs photoanode and perovskite/Si solar cell (behind photoanode). (C) The unbiased chronoamperometric curve of the PV-PEC tandem cell.

cell was obtained under identical illumination filtered by the front photoanode. Independently measured J-V curves for TANF/BiVO$_4$/In$_2$O$_3$ NRs photoanode and perovskite/Si solar cell were intersected, and operating photocurrent density (J_{OP}) and voltage (V_{OP}) of the PV-PEC tandem cell are defined as the intersection point [2,9,13-15,51].
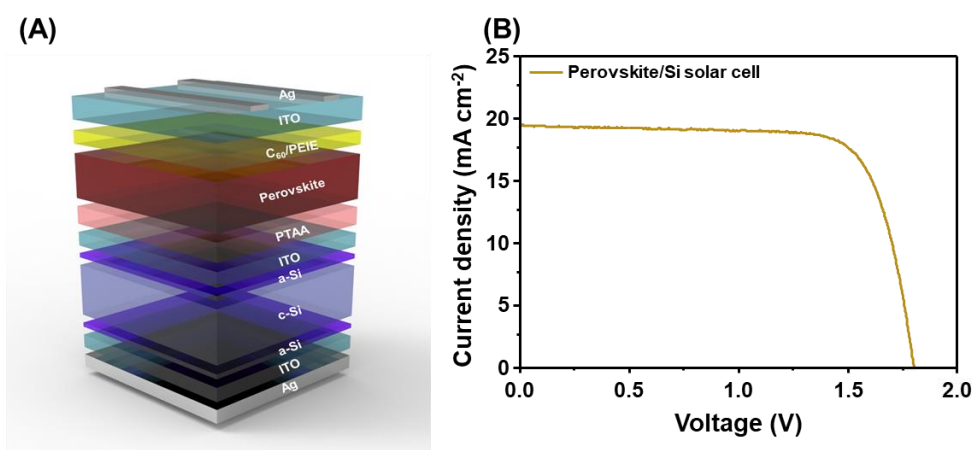
Figure 3.23 (A) Schematic illustration and (B) J-V curve of the perovskite/Si tandem solar cell.

Table 3.5 Parameters of a perovskite/Si solar cell.

Solar cell	J_{SC} [mA cm^{-2}]	V_{OC} [V]	FF	PCE [%]
Perovskite/ Si solar cell	19.31	1.80	0.76	26.55

As shown in Figure 3.22B, a high J_{OP} of 5 mA cm^{-2} at the V_{OP} of 1.45 V corresponds to the STH conversion efficiency of around 6.2%. Also, in an unbiased condition, I conducted chronoamperometry of the PV-PEC tandem cell for 4000 s, as shown in Figure 3.22C. The average current density was well-matched with the J_{OP} without external bias, indicating spontaneous water oxidation. To further reveal the practical PV-PEC tandem cell, I also evaluated STH conversion efficiency under different light intensities, as shown in Figure 3.24. Even though the efficiency decreased under weak light intensity (0.5 sun), it still showed a STH conversion efficiency of 3.4%.
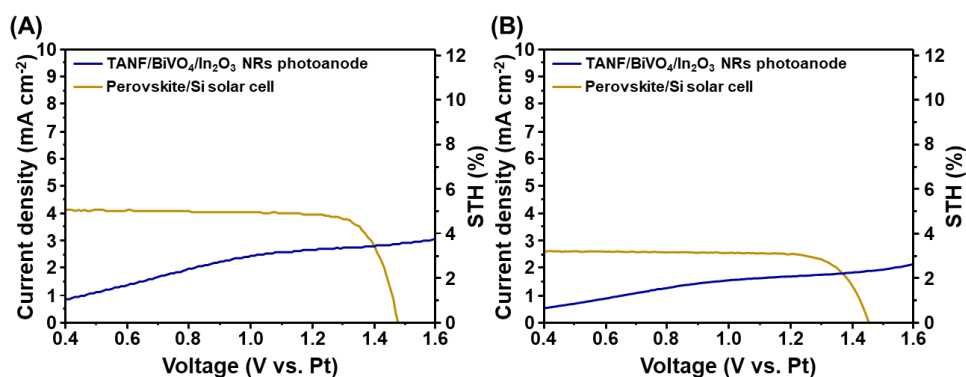
Figure 3.24 *J-V* curves of TANF/BiVO$_4$/In$_2$O$_3$ NRs photoanode and perovskite/Si tandem solar cell (behind photoanode) in 1 M K-B$_i$ buffer under (A) 0.5 sun and (B) 0.25 sun illumination.

3.4. Conclusion

In summary, I has demonstrated a novel configuration of TANF/BiVO$_4$/In$_2$O$_3$ NRs as an archetype that boosted the photoelectrochemical performance by exploiting the synergistic combination of heterojunction construction and morphology modification. I firstly disclosed that the introduction of In$_2$O$_3$ NRs as the ETL created an optimized type II heterojunction with BiVO$_4$, which enhanced charge separation by enabling favorable electron transport and hole blocking. Also, the architectures of BiVO$_4$, such as nanodot structure and core-shell structure on In$_2$O$_3$ NRs, have proven to have a significant impact on PEC performances. These two engineering strategies of heterostructure and nanostructuring are supported by analysis for charge carrier dynamics such as M-S, ECSA, and TRPL. Furthermore, as an OEC, uniform coating with TANF on BiVO$_4$/In$_2$O$_3$ NRs improved charge injection and expedited OER kinetics. The bespoke TANF/BiVO$_4$/In$_2$O$_3$ NRs photoanodes showed remarkable photocurrent densities of 7.1 mA cm^{-2} in sulfite oxidation and 4.2 mA cm^{-2} in water oxidation. Finally, the unbiased PV-PEC tandem cell comprising TANF/BiVO$_4$/In$_2$O$_3$ NRs photoanode and perovskite/Si solar cell generated the STH conversion efficiency of 6.2% without any external bias. I anticipates that this study will pave the way for the next generation of renewable energy applications.

3.5. References

[1]   J. H. Kim, D. Hansora, P. Sharma, J. W. Jang, J. S. Lee, *Chem. Soc. Rev.*, **2019**, 48, 1908.

[2]   X. Shi, H. Jeong, S. J. Oh, M. Ma, K. Zhang, J. Kwon, I. T. Choi, I. Y. Choi, H. K. Kim, J. K. Kim, J. H. Park, *Nat. Commun.*, **2016**, 7, 11943.

[3]   J. H. Kim, J. W. Jang, Y. H. Jo, F. F. Abdi, Y. H. Lee, R. van de Krol, J. S. Lee, *Nat. Commun.*, **2016**, 7, 13380.

[4]   J. H. Kim, Y. Jo, J. H. Kim, J. W. Jang, H. J. Kang, Y. H. Lee, D. S. Kim, Y. Jun, J. S. Lee, *ACS Nano*, **2015**, 9, 11820.

[5]   P. Chakthranont, T. R. Hellstern, J. M. McEnaney, T. F. Jaramillo, *Adv. Energy Mater.*, **2017**, 7, 1701515.

[6]   W. Yang, R. R. Prabhakar, J. Tan, S. D. Tilley, J. Moon, *Chem. Soc. Rev.*, **2019**, 48, 4979.

[7]   C. Jiang, S. J. A. Moniz, A. Wang, T. Zhang, J. Tang, *Chem. Soc. Rev.*, **2017**, 46, 4645.

[8]   K. Zhang, M. Ma, P. Li, D. H. Wang, J. H. Park, *Adv. Energy Mater.*, **2016**, 6, 1600602.

[9]   J. L. Young, M. A. Steiner, H. Döscher, R. M. France, J. A. Turner, T. G. Deutsch, *Nat. Energy*, **2017**, 2, 17028.

[10]   Y. Chen, X. Feng, Y. Liu, X. Guan, C. Burda, L. Guo, *ACS Energy Lett.*, **2020**, 5, 844.

[11]   B. Lamm, B. J. Trześniewski, H. Döscher, W. A. Smith, M. Stefik, *ACS Energy Lett.*, **2018**, 3, 112.

[12]   J. H. Kim, J. S. Lee, *Adv. Mater.*, **2019**, 31, 1806938.

[13]   Y. Qiu, W. Liu, W. Chen, G. Zhou, P. C. Hsu, R. Zhang, Z. Liang, S. Fan, Y. Zhang, Y. Cui, *Sci. Adv.*, **2016**, 2,1501764.

[14]   X. Shi, K. Zhang, K. Shin, M. Ma, J. Kwon, I. T. Choi, J. K. Kim, H. K. Kim, D. H. Wang, J. H. Park, *Nano Energy*, **2015**, 13, 182.

[15]   S. Wang, P. Chen, Y. Bai, J. H. Yun, G. Liu, L. Wang, *Adv. Mater.*, **2018**, 30, 1800486.

[16]   J. H. Baek, B. J. Kim, G. S. Han, S. W. Hwang, D. R. Kim, I. S. Cho, H. S. Jung, *ACS Appl. Mater. Interfaces*, **2017**, 9, 1479.

[17]   M. G. Lee, D. H. Kim, W. Sohn, C. W. Moon, H. Park, S. Lee, H. W. Jang, *Nano Energy*, **2016**, 28, 250.

[18]   K. H. Ye, H. Li, D. Huang, S. Xiao, W. Qiu, M. Li, Y. Hu, W. Mai, H. Ji, S. Yang, *Nat. Commun.*, **2019**, 10, 3687.

[19]   S. Xiao, C. Hu, H. Lin, X. Meng, Y. Bai, T. Zhang, Y. Yang, Y. Qu, K. Yan, J. Xu, Y. Qiu, S. Yang, *J. Mater. Chem. A*, **2017**, 5, 19091.

[20]   B. R. Lee, M. G. Lee, H. Park, T. H. Lee, S. A. Lee, S. S. M. Bhat, C. Kim, S. Lee, H. W. Jang, *ACS Appl. Mater. Interfaces*, **2019**, 11, 20004.

[21]   M. G. Lee, K. Jin, K. C. Kwon, W. Sohn, H. Park, K. S. Choi, Y. K. Go, H. Seo, J. S. Hong, K. T. Nam, H. W. Jang, *Adv. Sci.*, **2018**, 5, 1800727.

[22]   J. W. Yang, S. H. Ahn, H. W. Jang, *Curr. Opin. Green Sustainable Chem.*, **2021**, 29, 100454.

[23]   T. W. Kim, K. S. Choi, *Science*, **2014**, 343, 990.

[24]   Y. Shi, Y. Yu, Y. Yu, Y. Huang, B. Zhao, B. Zhang, *ACS Energy Lett.*, **2018**, 3, 1648.

[25]   S. Wang, T. He, J. H. Yun, Y. Hu, M. Xiao, A. Du, L. Wang, *Adv. Funct. Mater.*, **2018**, 28, 1802685.

[26]   D. Kim, H. J. Jung, I. J. Park, B. W. Larson, S. P. Dunfield, C. Xiao, J. Kim, J. Tong, P. Boonmongkolras, S. G. Ji, F. Zhang, S. R. Pae, M. Kim, S. B. Kang, V. Dravid, J. J. Berry, J. Y. Kim, K. Zhu, D. H. Kim, B. Shin, *Science*, **2020**, 368, 155.

[27]   I. J. Park, J. H. Park, S. G. Ji, M. A. Park, J. H. Jang, J. Y. Kim, *Joule*, **2019**, 3, 807.

[28]   U. Prasad, J. Prakash, A. M. Kannan, *Sustainable Energy Fuels*, **2020**, 4, 1496.

[29]   B. Jin, E. Jung, M. Ma, S. Kim, K. Zhang, J. il Kim, Y. Son, J. H. Park, *J. Mater. Chem. A*, **2018**, 6, 2585.

[30]   H. Sun, W. Hua, Y. Li, J. G. Wang, *ACS Sustainable Chem. Eng.*, **2020**, 8, 12637.

[31]   S. Bera, S. A. Lee, C. M. Kim, H. Khan, H. W. Jang, S. H. Kwon, *Chem. Mater.*, **2018**, 30, 8501.

[32]   J. Resasco, H. Zhang, N. Kornienko, N. Becknell, H. Lee, J. Guo, A. L. Briseno, P. Yang, *ACS Cent. Sci.*, **2016**, 2, 80.

[33]   C. Chen, J. Moir, N. Soheilnia, B. Mahler, L. Hoch, K. Liao, V. Hoepfner, P. O'Brien, C. Qian, L. He, G. A. Ozin, *Nanoscale*, **2015**, 7, 3683.

[34]   M. D. Sharma, C. Mahala, M. Basu, *ACS Appl. Nano Mater.*, **2020**, 3, 11638.

[35]   W. T. Liu, B. H. Wu, Y. T. Lai, N. H. Tai, T. P. Perng, L. J. Chen, *Nano Energy*, **2018**, 47, 18.

[36]   C. X. Kronawitter, L. Vayssieres, S. Shen, L. Guo, D. A. Wheeler, J. Z. Zhang, B. R. Antoun, S. S. Mao, *Energy Environ. Sci.*, **2011**, 4, 3889.

[37]   F. E. Osterloh, *Chem. Soc. Rev.*, **2013**, 42, 2294.

[38]   S. Kment, F. Riboni, S. Pausova, L. Wang, L. Wang, H. Han, Z. Hubicka, J. Krysa, P. Schmuki, R. Zboril, *Chem. Soc. Rev.*, **2017**, 46, 3716.

[39]   P. Zhang, T. Wang, J. Gong, *Chem*, **2018**, 4, 223.

[40]   K. Zhang, B. Jin, C. Park, Y. Cho, X. Song, X. Shi, S. Zhang, W. Kim, H. Zeng, J. H. Park, *Nat. Commun.*, **2019**, 10, 2001.

[41]   Y. Ma, S. R. Pendlebury, A. Reynal, F. le Formal, J. R. Durrant, *Chem. Sci.*, **2014**, 5, 2964.

[42]   W. Yang, J. H. Kim, O. S. Hutter, L. J. Phillips, J. Tan, J. Park, H. Lee, J. D. Major, J. S. Lee, J. Moon, *Nat. Commun.*, **2020**, 11, 861.

[43]   J. Park, W. Yang, J. Tan, H. Lee, J. W. Yun, S. G. Shim, Y. S. Park, J. Moon, *ACS Energy Lett.*, **2020**, 5, 136.

[44]   H. Wang, Y. Xia, H. Li, X. Wang, Y. Yu, X. Jiao, D. Chen, *Nat. Commun.*, **2020**, 11, 3078.

[45] A. Li, X. Chang, Z. Huang, C. Li, Y. Wei, L. Zhang, T. Wang, J. Gong, *Angew. Chem. Int. Ed.*, **2016**, 55, 13734.

[46] W. Yang, S. Lee, H. C. Kwon, J. Tan, H. Lee, J. Park, Y. Oh, H. Choi, J. Moon, *ACS Nano*, **2018**, 12, 11088.

[47] L. Zhang, Y. Li, C. Li, Q. Chen, Z. Zhen, X. Jiang, M. Zhong, F. Zhang, H. Zhu, *ACS Nano*, **2017**, 11, 12753.

[48] S. S. M. Bhat, J. M. Suh, S. Choi, S. P. Hong, S. A. Lee, C. Kim, C. W. Moon, M. G. Lee, H. W. Jang, *J. Mater. Chem. A*, **2018**, 6, 14633.

[49] Y. Shi, Y. Yu, Y. Liang, Y. Du, B. Zhang, *Angew. Chem. Int. Ed.*, **2019**, 58, 3769.

[50] Y. Dai, J. Yu, C. Cheng, P. Tan, M. Ni, *J. Mater. Chem. A*, **2020**, 8, 6984.

[51] J. W. Yang, I. J. Park, S. A. Lee, M. G. Lee, T. H. Lee, H. Park, C. Kim, J. Park, J. Moon, J. Y. Kim, H. W. Jang, *Appl. Catal. B*, **2021**, 293, 120217.

[52] J. A. Seabold, K. S. Choi, *J. Am. Chem. Soc.*, **2012**, 134, 2186.

[53] K. J. McDonald, K. S. Choi, *Energy Environ. Sci.*, **2012**, 5, 8553.

[54]   F. F. Abdi, L. Han, A. H. M. Smets, M. Zeman, B. Dam, R. van de Krol, *Nat. Commun.*, **2013**, 4, 2195.

[55]   X. Chang, T. Wang, P. Zhang, J. Zhang, A. Li, J. Gong, *J. Am. Chem. Soc.*, **2015**, 137, 8356.

[56]   D. K. Lee, K. S. Choi, *Nat. Energy*, **2018**, 3, 53.

[57]   H. S. Han, S. Shin, D. H. Kim, I. J. Park, J. S. Kim, P. S. Huang, J. K. Lee, I. S. Cho, X. Zheng, *Energy Environ. Sci.*, **2018**, 11, 1299.

[58]   S. Wang, T. He, P. Chen, A. Du, K. Ostrikov, W. Huang, L. Wang, *Adv. Mater.*, **2020**, 32, 2001385.

[59]   S. K. Pilli, R. Janarthanan, T. G. Deutsch, T. E. Furtak, L. D. Brown, J. A. Turner, A. M. Herring, *Phys. Chem. Chem. Phys.*, **2013**, 15, 14723.

[60]   X. Shi, I. Y. Choi, K. Zhang, J. Kwon, D. Y. Kim, J. K. Lee, S. H. Oh, J. K. Kim, J. H. Park, *Nat. Commun.*, **2014**, 5, 4775.

[61]   Y. Pihosh, I. Turkevych, K. Mawatari, J. Uemura, Y. Kazoe, S. Kosar, K. Makita, T. Sugaya, T. Matsui, D. Fujita, M. Tosa, M. Kondo, T. Kitamori, *Sci. Rep.*, **2015**, 5, 11141.

[62]   Y. Zhou, L. Zhang, L. Lin, B. R. Wygant, Y. Liu, Y. Zhu, Y. Zheng, C. B. Mullins, Y. Zhao, X. Zhang, G. Yu, *Nano Lett.*, **2017**, 17, 8012.

[63] K. Kim, S. K. Nam, J. H. Park, J. H. Moon, *J. Mater. Chem. A*, **2019**, 7, 4480.

[64] L. Zhou, C. Zhao, B. Giri, P. Allen, X. Xu, H. Joshi, Y. Fan, L. v. Titova, P. M. Rao, *Nano Lett.*, **2016**, 16, 3463.

[65] Q. Pan, A. Li, Y. Zhang, Y. Yang, C. Cheng, *Adv. Sci.*, **2020**, 7, 1902235.

[66] K. Kim, J. Yang, J. H. Moon, *ACS Appl. Mater. Interfaces*, **2020**, 12, 21894.

Chapter 4

Multifunctional Nano-Heterogeneous Ni(OH)$_2$/NiFe Catalysts on Silicon Photoanode toward Efficient Water and Urea Oxidation

4.1. Introduction

Harnessing the sunlight to convert carbon-free and energy-rich hydrogen by photoelectrochemical (PEC) water splitting is one of the solutions to provide clean electricity [1–3]. The semiconductors with moderate bandgap are used as photoelectrodes for light absorption. Under solar illumination, photogenerated electron-hole pairs are separated and transported to the solid/electrolyte interfaces. The electrons are consumed for hydrogen evolution reaction (HER), and holes are employed for oxygen evolution reaction (OER) at the anode. The reaction in alkaline aqueous solution is expressed as the following equation:

$$\text{Anode (OER): } 4OH^- \rightarrow O_2 + 4e^- + 2H_2O$$

$$\text{Cathode (HER): } 2H_2O + 2e^- \rightarrow H_2 + 2OH^-$$

$$\text{Overall: } 2H_2O \rightarrow 2H_2 + O_2$$
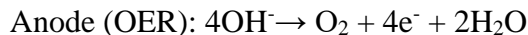
The OER, which is a 4-electron-transfer process, is challenging because of sluggish reaction and the requirement of substantial energy of 1.23 V [4], and thus determines the overall PEC efficiency. To deal with it, OER can be conducted with other favorable (photo)electrochemical reactions, which can be triggered at a lower potential. In this regard, urea oxidation reaction (UOR) is a promising reaction since its thermodynamic potential is 0.37 V and the utility of pollutant urea to valuable fuels [5,6]. Various electrocatalysts for

urea oxidation have been reported and introduced to photoanodes as cocatalysts to enhance the photocatalytic activity toward urea oxidation [6,7].

An n-type silicon, 2nd abundant element in the earth crust, has been widely utilized in photovoltaics and microelectronics because of its long carrier lifetime and high crystallinity [8]. Considering the required aspects for the photoelectrode material (i.e., absorption of the solar spectrum, cost-effectiveness, and long carrier diffusion length), Si is a prime candidate to be employed for PEC devices. However, exploiting Si as photoanode is challenging because of its instability in aqueous electrolytes and low catalytic activity [9,10]. The valence band position of silicon is more negative than the oxidation potential (H_2O/O_2), requiring a large applied potential. Also, its theoretical photovoltage is ~750 mV [11], which is insufficient for driving water splitting reaction. In the past decades, many efforts have been devoted to preventing Si from being corroded by introducing protection layers with chemical stability and catalytic activity in alkaline electrolytes [12–15]. Especially, metal-insulator-semiconductor (MIS) architecture is a promising candidate for Si photoanodes. Because MIS structure prevents the surface recombination originating from the metal-induced gap states compared to the direct metal-semiconductor Schottky junction and increase barrier height, leading to the large

photovoltage output [16]. To maximize the barrier height, which is the driving force for generating photovoltage, interface engineering of MIS photoanodes has been conducted by inserting ultrathin tunneling oxide layer (e.g., HfO_x, Al_2O_3, TiO_2, SiO_x) using high-vacuum types of equipment [17–21]. The introduction of efficient co-catalysts with optical transparency on MIS photoanode can accelerate the PEC activity at low overpotential. Loget *et al*. reported the $Si/SiO_x/Ni$ MIS structures with Ni-Prussian blue derivative (NiFePB) [22]. Similar work was done using CoFePB and NiRuPB with inhomogeneity of metal thin film for OER and UOR [23]. Recently, amorphous Ni-Mo-O coatings with the optically adaptive property were introduced on n-$Si/SiO_x/Ni$ MIS photoanodes as UOR catalysts [24]. From an integrated point of view, however, studies on the integrated analysis of MIS photoanodes by engineering each layer, such as the effects of physical/chemical properties of the insulating layer and metal composition on OER and UOR performance, are still intriguing.

In this article, I reports the tailored MIS photoanodes for water and urea oxidation and investigate their properties by manipulating the insulating SiO_x layer using chemical etching methods, the composition of Ni_xFe_{1-x} metal thin films, and incorporation of additional $Ni(OH)_2$ catalyst via electrodeposition. I shows that the status of the SiO_x layer has a huge effect

on the properties of MIS photoanodes. With the native SiO_x insulating layer, composition control of Ni_xFe_{1-x} metal thin film improves the photovoltages and exhibits catalytic activity. A systematic study reveals that introducing additional $Ni(OH)_2$ catalysts on $Ni_{0.5}Fe_{0.5}/SiO_x/n$-Si leads to a higher fill factor of over 25% and enhances the charge transfer kinetics and stability. With the aids of perovskite/Si tandem solar cell, wired photovoltaic (PV)-PEC tandem device generates a photocurrent of 8.8 mA cm^{-2}, corresponding to the solar-to-hydrogen (STH) conversion efficiency of 10.8% under zero bias. I finally demonstrates that optimized $Ni(OH)_2/Ni_{0.5}Fe_{0.5}/SiO_x/n$-Si generates high performance toward OER and shows a low onset potential of 0.83 V vs. RHE for UOR. These results indicate the design of efficient MIS photoanodes consisting of abundant materials toward clean H_2 production using urea-containing wastewater.

4.2. Experimental procedures

4.2.1. Preparation of substrates

An Phosphorous-doped n-Si wafer ((100) oriented, single-side polished, 1-5 $\Omega \cdot cm$) was cut into 1.5 cm × 1.5 cm pieces. All wafer pieces were cleaned with acetone, isopropanol alcohol, and ultrapure water by ultrasonication. The Si wafers without any etching process were denoted as SiO_x/n-Si. To further control the SiO_x layer, first, I conducted a conventional RCA-2 etching process (denoted as $SiO_{x,RCA}$/n-Si); Si pieces were soaked in 3/1 v/v concentrated H_2SO_4/H_2O_2 solution for 10 min, immersed in a buffered HF etchant for 30 sec, and cleaned with DI water. Then wafers were soaked in 5/1/1 (by volume) concentrated H_2O, hydrochloric acid, and hydrogen peroxide at 80 °C for 30 min. Finally, the Si pieces were rinsed with ultrapure water and dried under a flow of N_2. Second, n-Si wafers were soaked in buffered oxide etchant (7:1, J. T. Baker) for 30 seconds to remove the residual SiO_x layer (denoted as $SiO_{x,BOE}$/n-Si).

4.2.2. E-beam deposition of transition metals

Transition metal thin layers were deposited on silicon substrate by electron beam evaporator (Rocky Mountain Vacuum Tech.). Applied e-beam voltage was set at 7.5 kV, and a base pressure was maintained in the range of 10^{-6} Torr. All transition metal thin film layers were deposited with the rate of 0.1-0.2 Å s^{-1}. Ni (Taewon Scientific Co., 99.999%) and Fe (Taewon Scientific Co., 99.999%) evaporation targets were used, and the NiFe alloy targets with various compositions (wt%) were prepared by using an arc furnace.

4.2.3. Electrodeposition of Ni(OH)$_2$

To conduct electrodeposition of Ni(OH)$_2$, back side of silicon was scratched and InGa eutectic alloy (Sigma Aldrich) was applied to form an ohmic contact. Then, copper wire was attached on top of the InGa alloy using conductive silver paste. After the silver paste dried, the Si surface except for the deposition area (1 cm $\times$ 1 cm) was completely sealed with an adhesive Kapton tape to prevent contact with the electrolyte. Electrodeposition of Ni(OH)$_2$ was conducted in a standard three-electrode system; an encapsulated Si electrode as the working electrode, a Pt mesh as the counter electrode, and a saturated calomel electrode (SCE) as the reference electrode. Electrolytes were prepared by dissolving 0.004 M nickel nitrate hydrate (NiNO$_3$·6H$_2$O, Daejung) and 0.01 M potassium nitrate (KNO$_3$, Daejung) and kept at the temperature of 40 °C. Electrodeposition of Ni(OH)$_2$ was conducted by applying -0.15 mA for 10 s. After electrodeposition, Si pieces were rinsed with deionized water, dried under nitrogen gases, and Kapton tapes were removed.

4.2.4. Fabrication of perovskite/Si tandem solar cell

For the rear side of the Si cell, 80-nm-thick ITO films were deposited using sputter, and 300-nm-thick Ag electrode was deposited using a thermal evaporator. For the front side of Si cell, 20-nm-thick ITO films were formed as the recombination layer. On top of the ITO/silicon bottom cell, PTAA/perovskite/C_{60} layer was deposited sequentially. PTAA solution (5 mg mL^{-1} in toluene) was spin-coated at 6,000 rpm for 25 s, followed by annealing at 100 °C for 10 min. For the preparation of 3D perovskites, solutions were prepared by dissolving formamidinium (FAI), methylammonium bromide (MABr), CsI, PbI_2, and $PbBr_2$. The molar ratio was adjusted to form stoichiometric $FA_{0.65}MA_{0.20}Cs_{0.15})Pb(I_{0.8}Br_{0.2})_3$ in mixed solvent system (DMF:NMP = 4:1 (v/v)). 2D additive perovskite solution was prepared by adding 2 mol% $Pb(SCN)_2$ and 2 mol% PEAX (=I, SCN) to the 3D perovskite solution. The prepared solution was spin-coated at 4,000 rpm for the 20 s on PTAA film. To fully crystallize the spin-coated films, it was immersed in diethyl ether (DE) for 30s. After immersing in DE, the color of the film changed to dark brown, indicating the formation of crystallized perovskite films. The crystallized film was annealed at 100 °C for 10 min. On top of the perovskite, C_{60} layers (C60, bathocuproine (BCP), Ag electrode) were deposited using a thermal evaporator. A 0.2 wt% of PEIE (80% ethoxylated solution) in methyl alcohol was spin-coated at 6,000 rpm

for 30 s. ITO films were deposited on the C_{60}/PEIE layer using sputtering at room temperature. A 150-nm-thick Ag metal grid was deposited using a thermal evaporator on the ITO film to fabricate final monolithic perovskite/Si tandem cells.

4.2.5. Characterization

The morphologies and microstructures of samples were analyzed by field emission scanning microscopy (MERLIN Compact, JEISS) and transmission electron microscopy (JEM-2100F, JEOL). GIXRD (X'pert Pro, PANalytical) analysis was conducted to confirm the phase of Ni_xFe_{1-x}. X-ray photoelectron spectroscopy (AXIS-His, KRATOS) analysis was performed to investigate the surface bonding of samples. The narrow spectrums were analyzed using CASAXPS software. The reflectance of the sample was determined by UV-Vis (V-770, JASCO). ICP-MS (NexION 350D, Perkin-Elmer) analysis was conducted to confirm the dissolution of Ni_xFe_{1-x} films.

4.2.6. PEC measurements

PEC measurements were carried out in a three-electrode system using a potentiostat (Ivium nStat, Ivium Technologies) with Pt mesh as a counter electrode and Ag/AgCl (KCl sat.) as a reference electrode. A light source was Xe arc lamp (LS 150, Abet Technologies), and the intensity of the light from the solar simulator with AM 1.5G filter was calibrated using a reference photodiode (S300, McScience) to be 1 sun (100 mW cm^{-2}). The incident photon-to-current conversion efficiency was measured using a monochromator (MonoRa150) and solar simulator by applying 1.23 V and 1.5 V (vs. RHE). Electrochemical impedance spectroscopy (EIS) was carried out by using the alternating current with an amplitude of 10 mV and applying the onset potential of the samples. The sweeping frequency ranged from 250 kHz to 1 Hz. The Nyquist plots were fit to the equivalent circuit using the Z plot 2.x software. According to the Nernst equation, the measured potential (vs. Ag/AgCl) was converted to the reversible hydrogen electrode (RHE) scale:

$$E_{RHE} = E_{Ag/AgCl} + E^{\circ}_{Ag/AgCl} + 0.059 \times \text{pH}$$

, where E_{RHE} is the potential versus RHE, $E_{Ag/AgCl}$ is the experimentally measured potential versus Ag/AgCl (KCl sat.), $E^{\circ}_{Ag/AgCl}$ is 0.198 V at 25 °C, and the pH of the 1 M NaOH electrolyte is 14.

The charge injection efficiency (Φ_{inj}) of the sample was calculated using LSV curves in 1 M NaOH with or without 0.5 M Na_2SO_3, where Na_2SO_3 was used as a hole scavenger:

$$J_{PEC} = J_{abs} \times \Phi_{sep} \times \Phi_{inj}$$

$$J_{Na_2SO_3} = J_{abs} \times \Phi_{sep}$$

,where J_{PEC} is the measured photocurrent density and J_{abs} is an ideal photocurrent density, assuming that all absorbed photons are converted to current.

4.3. Results and discussion

4.3.1. SiO$_x$ control

I prepared three types of SiO$_x$ layers (SiO$_x$, SiO$_{x,RCA}$, SiO$_{x,BOE}$) to investigate the effects of controlling SiO$_x$ on photoelectrochemical (PEC) properties of Si photoanodes. Further details of preparing SiO$_x$ layers are provided in the Experimental Section. Contact angle measurements were conducted to investigate the surface wetting properties of Si substrates with controlled SiO$_x$. As shown in Figure 4.1(a)-(c), contact angles of SiO$_x$/n-Si, SiO$_{x,RCA}$/n-Si, and SiO$_{x,BOE}$/n-Si were 47°, 20°, and 83°, respectively. It has been reported that Si completely covered with oxides or –OH terminated Si is hydrophilic and stable while Si-H surface or Si-CH$_x$ is hydrophobic [25,26]. By using chemical etching methods, I obtained Si with different surface termination: SiO$_x$ has oxide cover, SiO$_{x,RCA}$ has –OH terminated surface, and SiO$_{x,BOE}$ has Si-H surface.

Fe thin films were deposited on n-Si substrates with a distinctive SiO$_x$ layer using an e-beam evaporator to form metal-insulator-semiconductor (MIS) structured photoanodes. Figure 4.2 shows the x-ray photoelectron spectroscopy (XPS) spectra of Fe thin films on Si, where Fe 2p$_{3/2}$ peak consists of Fe^{3+} (710.3 eV and 713.2 eV) peaks and Fe^{3+} satellite peak (718.8 eV). O 1s peak can be deconvoluted into three peaks which represent Fe–O (529.6 eV), Fe–O–H (531.4 eV), and H–O–H (533.2 eV) bonding [27–31].

Figure 4.1(d)-(f) shows a high-resolution cross-sectional transmission electron microscope (HRTEM) images of Fe/SiO$_x$/n-Si, Fe/SiO$_{x,RCA}$/n-Si, and Fe/SiO$_{x,BOE}$/n-Si interface. Fe thin films were uniformly deposited on the substrates, having a thickness of ~4 nm. The Fe/SiO$_x$/n-Si and Fe/SiO$_{x,RCA}$/n-Si showed a similar SiO$_x$ thickness of 1.5 nm between the Si substrate and Fe film, while Fe/SiO$_{x,BOE}$/n-Si showed damaged interface
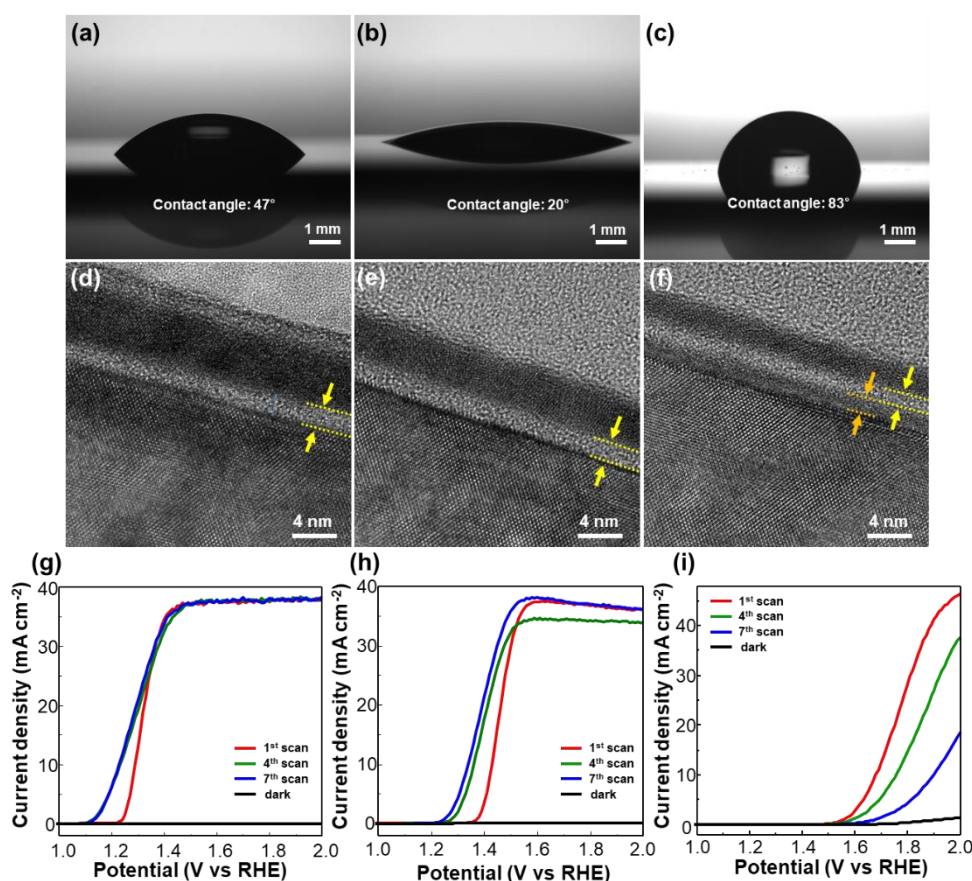
**Figure 4.1** Effect of controlling SiO$_x$ layer. Contact angles of the silicon substrates; (a) SiO$_x$/n-Si, (b) SiO$_{x,RCA}$/n-Si, and (c) SiO$_{x,BOE}$/n-Si. Cross-sectional TEM images of the deposited thin films on silicon substrates; (d) Fe/SiO$_x$/n-Si, (e) Fe/SiO$_{x,RCA}$/n-Si, and (f) Fe/SiO$_{x,BOE}$/n-Si. *J-V* curves of (g) Fe/SiO$_x$/n-Si, (h) Fe/SiO$_{x,RCA}$/n-Si and (i) Fe/SiO$_{x,BOE}$/n-Si.

between Fe layer and Si (orange). It has been reported that HF-treated Si can have a rough silicon surface [32], and the obtained cross-sectional HRTEM image of Fe/SiO$_{x,BOE}$/n-Si shows the increase in roughness of the surface and two distinctive layers compared to SiO$_x$ and SiO$_{x,RCA}$.

The PEC performances of insulating SiO$_x$-controlled photoanodes were investigated by measuring linear sweep voltammetry curves in 1 M NaOH electrolyte under 1sun illumination (100 mW cm^{-2}). All PEC measurements were conducted under the AM 1.5G using a solar simulator (ABET Technologies). The spectral irradiances of the solar simulator and AM 1.5G are shown in Figure 4.3. Considering the 100% of external quantum efficiency of the system, the integrated current density based on the spectral irradiance of the solar simulator showed a slightly higher current density than AM 1.5G system. Figure 4.1(g) and 1(h) show the *J-V* curves of
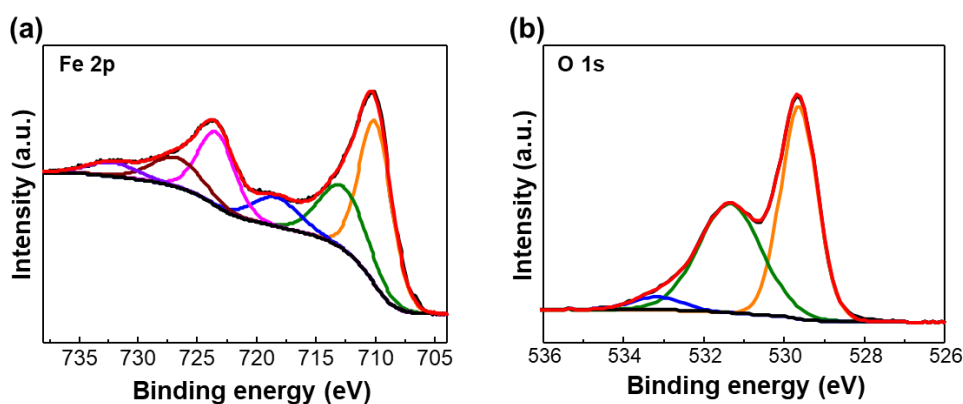
Figure 4.2 XPS spectra of (a) Fe 2p and (b) O 1s for the Fe/SiO$_x$/n-Si.
Fe/SiO$_x$/n-Si and Fe/SiO$_{x,RCA}$/n-Si, respectively. I defines the onset potential

as a potential which is required to reach the photocurrent of 1 mA cm^{-2}.

Fe/SiO$_x$/n-Si showed an onset potential of 1.14 V vs. RHE, while that of

Fe/SiO$_{x,RCA}$/n-Si was 1.26 V vs. RHE, which shifted to the anodic direction.

In the case of Fe/SiO$_{x,BOE}$/n-Si, drastic degradation of *J-V* performance was

observed, as shown in Figure 4.1(i), which might have originated from the

presence of a defective SiO$_x$ layer as shown in Figure 4.1(f). Therefore, it

can be observed that the native SiO$_x$ layer can form a proper MIS junction

by separating metal and Si, preventing surface recombination.
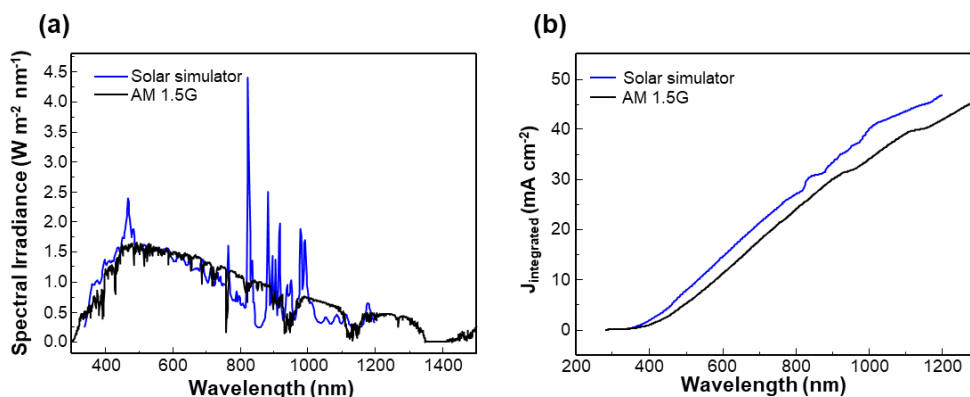
Figure 4.3 Comparison of (a) spectral irradiance and (b) integrated photocurrent density assuming EQE of 100% between solar simulator (ABET Technologies) and AM 1.5G.

4.3.2. Composition control of Ni_xFe_{1-x} metal thin film

To evaluate the catalytic effects of the composition of metal thin films on MIS photoanodes for photoelectrochemical water oxidation, the Ni/Fe ratio of metal thin films was controlled by an e-beam evaporator. The performance of MIS photoanode is significantly affected by the thickness of the insulator and metal film, changing the extent of band bending [20]. Therefore, the same thickness of the composition-controlled Ni_xFe_{1-x} thin films was introduced to exclude the thickness-dependent characteristics in MIS photoanodes. The thickness of native SiO_x was fixed to ~ 2 nm, and the metallic Ni_xFe_{1-x} thin films were deposited with ~4 nm thickness. As shown in Figure 4.4, introducing Ni_xFe_{1-x} thin layers on silicon substrates increased the light reflection due to the nature of reflecting light. Targets with Ni/Fe
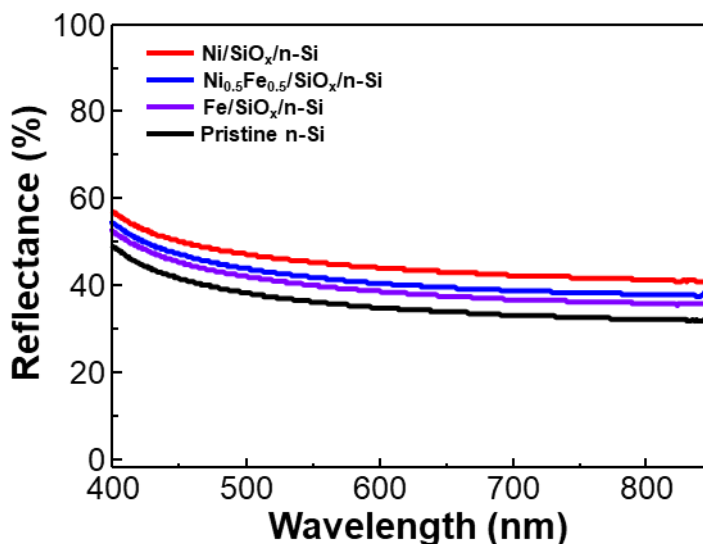
Figure 4.4 Reflectances of pristine Si and Ni_xFe_{1-x} thin films on Si substrate.

ratio of 1:0. 9:1, 3:1, 1:1, 1:9, and 0:1 were used to control the composition of NiFe thin films on SiO_x/n-Si photoanodes. Grazing incidence x-ray diffraction (GIXRD) analysis revealed that e-beam deposited metal thin films on silicon were an amorphous phase (Figure 4.5). An n-type
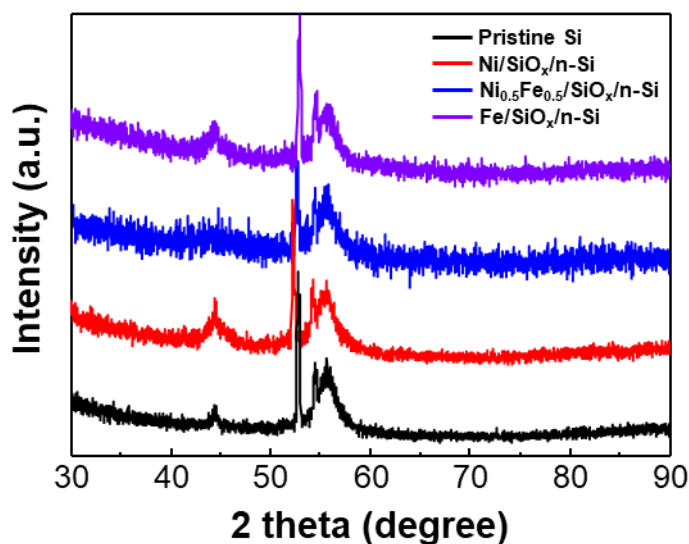
Figure 4.5 GIXRD patterns of pristine Si and Ni_xFe_{1-x}/SiO_x/n-Si.
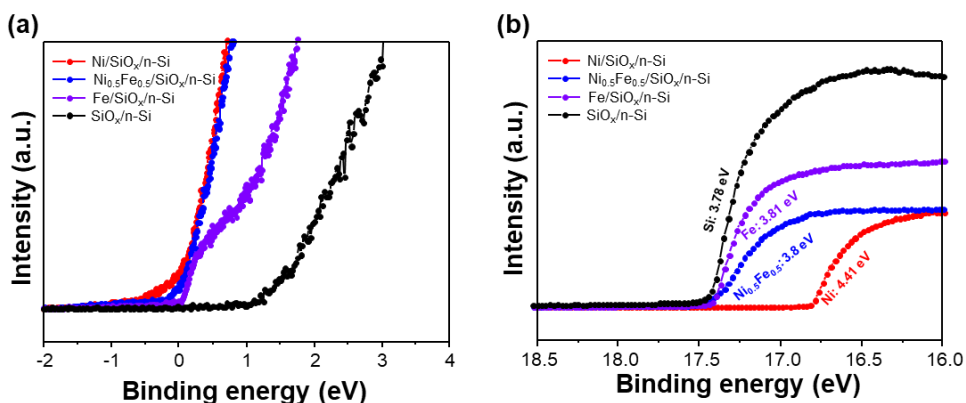
Figure 4.6 (a) Ultraviolet photoemission spectroscopy (UPS) and (b) X-ray photoemission valence spectra of n-Si with metal thin films.

semiconductor can form a Schottky junction with high work-function metals [15]. As shown in Figure 4.6, the metal's work function was derived by ultraviolet photoelectron spectroscopy (UPS). Ni has a work function of 4.41 eV, $Ni_{0.5}Fe_{0.5}$ of 3.8 eV, and Fe of 3.81 eV. As the metal's work function is close to the Fermi level of n-Si, the onset potential shifted to the cathodic direction. I conducted XPS analysis to figure out the chemical states of the metal thin films. As shown in Figure 4.7, deconvoluted narrow Ni 2p spectra revealed the presence of metallic Ni^0 peak (852.2 eV) and partial Ni^{2+} peak (854.5 eV) for Ni thin film, and Ni 2p and Fe 2p spectra showed metallic Ni^0 peak (852.5 eV) and Ni^{2+} peak (855 eV) and Fe^{3+} peaks (710.3 eV and 712.4 eV) for $Ni_{0.5}Fe_{0.5}$ thin film [33–37].
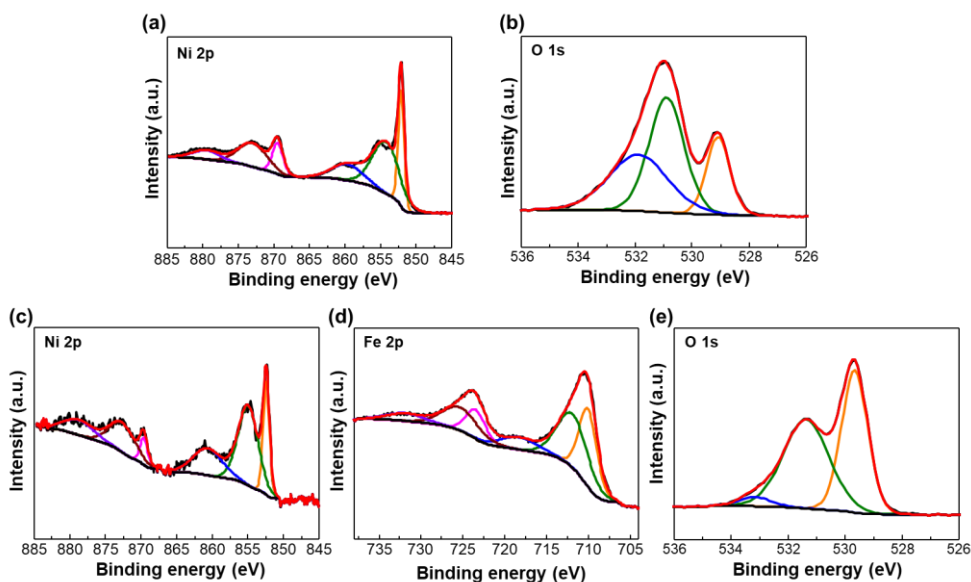
Figure 4.7 XPS spectra of (a) Ni 2p and (b) O 1s for the $Ni/SiO_x/n$-Si and (c) Ni 2p, (d) Fe 2p, and (e) O 1s for the $Ni_xFe_{1-x}/SiO_x/n$-Si.

I prepared Ni_xFe_{1-x} thin films on metallic p^{++}-Si and semiconducting n-Si, respectively, to evaluate electrochemical/photoelectrochemical characteristics. The overpotential of p^{++}-Si was calculated using the potential difference between the required potential to reach 10 mA cm^{-2} and water oxidation potential (1.23 V vs. RHE). As shown in Figure 4.8(a), Fe thin films on p^{++}-Si showed a high overpotential of 420 mV compared to that of 300 mV for Ni/SiO$_x$/p^{++}-Si. Through the J-V curves, Ni-rich thin films
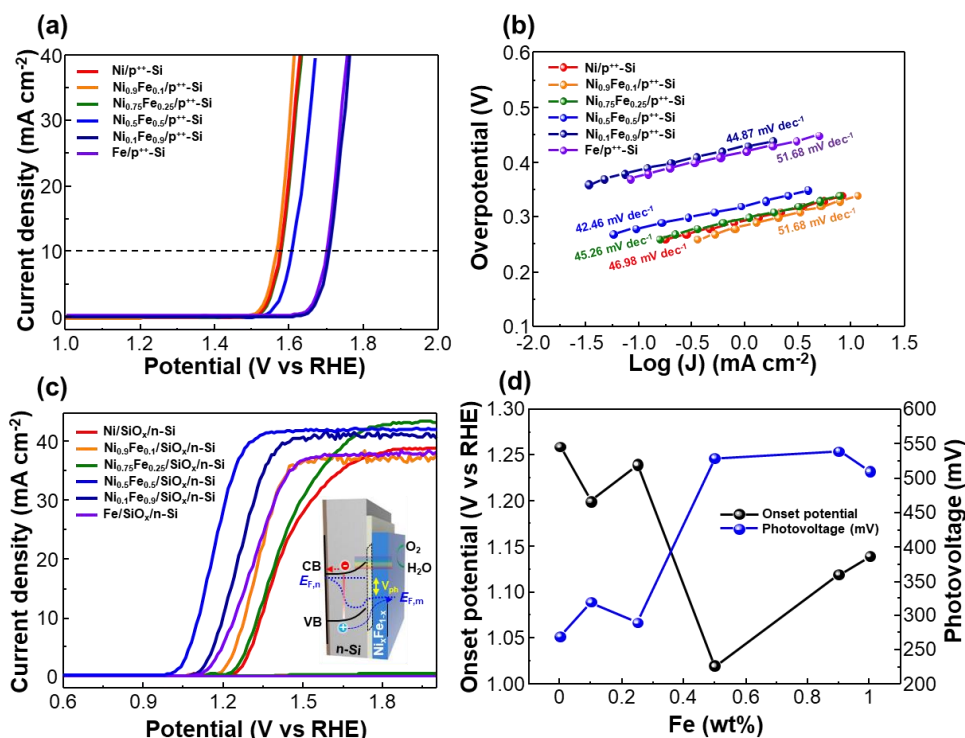
Figure 4.8 Electrochemical and photoelectrochemical performances of the Ni_xFe_{1-x} thin film/Si electrodes. (a) Electrochemical performances of the deposited Ni_xFe_{1-x} thin films on p^{++}-Si. (b) Tafel plots of Ni_xFe_{1-x} thin films obtained from the curves in (a). (c) Linear sweep voltammetry curves of Si photoanodes with Ni_xFe_{1-x} thin film catalysts. (d) Comparison of onset potential and photovoltage between Ni_xFe_{1-x}/SiO$_x$/n-Si photoanodes.

showed more favorable electrochemical properties for water oxidation than Fe-rich thin films. I converted the polarization curves to Tafel plots to investigate the catalytic activity of Ni_xFe_{1-x} thin films. Figure 4.8(b) shows the Tafel slopes of Ni_xFe_{1-x} thin films, in which the linear portion of the curves was used. $Ni_{0.5}Fe_{0.5}/SiO_x/p^{++}$-Si showed the lowest Tafel slope of 42.46 mV dec^{-1}.

Figure 4.8(c) shows the *J-V* curves of composition-controlled $Ni_xFe_{1-x}/SiO_x/$n-Si under 1 sun illumination. Contrary to the *J-V* curves of $Ni_xFe_{1-x}/SiO_x/p^{++}$-Si, the $Ni_xFe_{1-x}/SiO_x/$n-Si photoanodes showed different tendency regarding the onset potential (V at 1 mA cm^{-2}). $Fe/SiO_x/$n-Si showed a lower onset potential of 1.14 V vs. RHE compared to that of 1.26 V vs. RHE for $Ni/SiO_x/$n-Si. By manipulating the composition of Ni_xFe_{1-x}, the lowest onset potential of 1.02 V vs. RHE was achieved for $Ni_{0.5}Fe_{0.5}/SiO_x/$n-Si. MIS junction photoanodes can offer sufficient photovoltages by using thin tunnel oxides and appropriate metal with high work function [38]. Photovoltage is defined as the difference between the quasi-Fermi level of electrons and holes. I compared the photovoltages of $Ni_xFe_{1-x}/SiO_x/$n-Si by calculating the onset potential (V at 1 mA cm^{-2}) differences between n-Si and p^{++}-Si. As shown in Figure 4.8(d), the photovoltage of $Ni/SiO_x/$n-Si was 270 mV, while

that of Fe/SiO$_x$/n-Si was 510 mV. By controlling the ratio of Ni and Fe, photovoltage of 530 mV was achieved for Ni$_{0.5}$Fe$_{0.5}$/SiO$_x$/n-Si.

The charge injection efficiency, representing the efficiency of photogenerated holes at the semiconductor-electrolyte interfaces consumed for water oxidation, was derived by the ratio of photocurrent density in 1 M NaOH with and without 0.5 M Na$_2$SO$_3$. As shown in Figure 4.9, Ni$_{0.5}$Fe$_{0.5}$/SiO$_x$/n-Si showed the highest charge injection efficiency over 90% at 1.23 V vs. RHE. The stability of MIS-structured Si photoanodes was investigated by conducting chronoamperometry measurements at a potential of 1.5 V versus RHE in 1 M NaOH electrolyte in AM 1.5G condition. As shown in Figure 4.10, Ni/SiO$_x$/n-Si was able to stand 80 hours without any
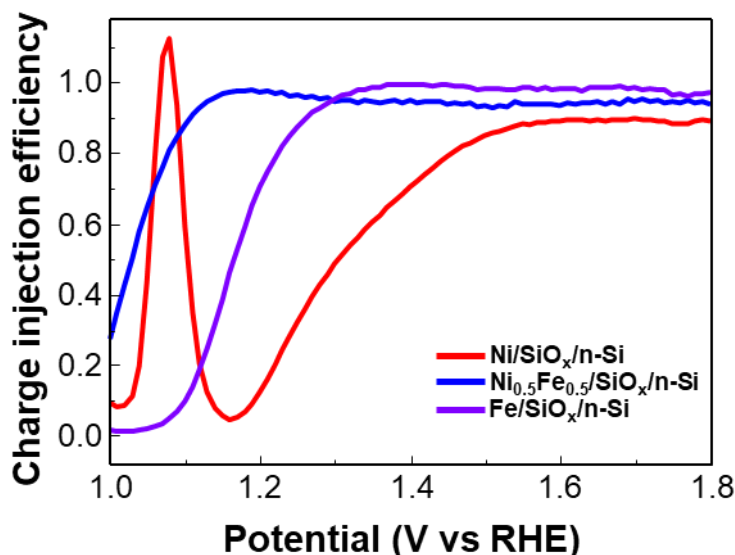
Figure 4.9 Charge injection efficiencies of Ni/SiO$_x$/n-Si, Ni$_{0.5}$Fe$_{0.5}$/SiO$_x$/n-Si, and Fe/SiO$_x$/n-Si.

remarkable decay of photocurrent density, while $Fe/SiO_x/n$-Si became drastically degraded within 1-hour measurement. $Ni_{0.5}Fe_{0.5}/SiO_x/n$-Si withstood for 1 hour and showed continuous photocurrent decay. Chung *et al.* reported the activity-stability trend of Fe-M hydr(oxy)oxides and showed the quick dissolution of Fe from the electrolytes, which is well-matched with our results [39]. I performed inductively coupled plasma mass spectroscopy (ICP-MS) analysis to figure out the changes in the Ni_xFe_{1-x} layer before and after stability measurements. I used diluted 1 M NaOH electrolytes before and after stability tests. As shown in Table 4.1, compared to $Ni/SiO_x/n$-Si with the negligible change of Ni content, the Fe amount of electrolytes were increased after the stability test of $Fe/SiO_x/n$-Si. Through the stability test and ICP-MS results, it was turned out that Fe itself cannot endure in high alkaline electrolytes. Integrated results showed a trade-off between the onset potential and the stability as adjusting the Ni_xFe_{1-x} composition.

Table 4.1. Concentration of elements in samples (ppb).

	Ref. electrolytes	$Ni/SiO_x/n$-Si	$Ni_{0.5}Fe_{0.5}/SiO_x/n$-Si	$Fe/SiO_x/n$-Si
Ni	0.2	0.2	0.2	-
Fe	5.2	-	6.1	9.5
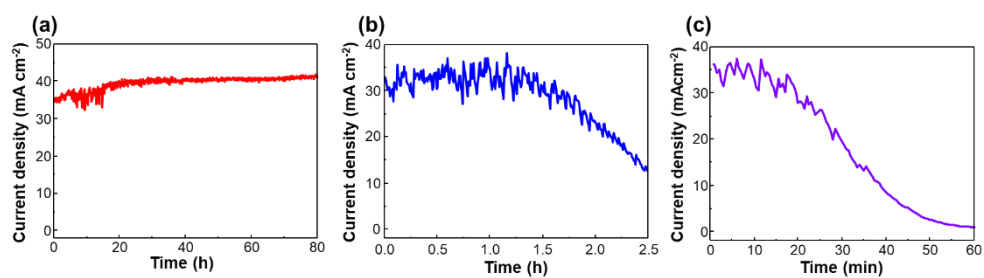
Figure 4.10 Stability test of (A) Ni/SiO$_x$/n-Si, (B) Ni$_{0.5}$Fe$_{0.5}$/SiO$_x$/n-Si, and (C) Fe/SiO$_x$/n-Si.

4.3.3. Electrodeposition of Ni(OH)$_2$ catalysts for water oxidation

Additional Ni(OH)$_2$ catalysts were introduced on Ni$_{0.5}$Fe$_{0.5}$/SiO$_x$/n-Si via cathodic electrodeposition method to expedite water oxidation reaction. I denotes the photoanodes as x-Ni(OH)$_2$/Ni$_{0.5}$Fe$_{0.5}$/SiO$_x$/n-Si, where x is the deposition time (seconds). As shown in the photographs of the MIS
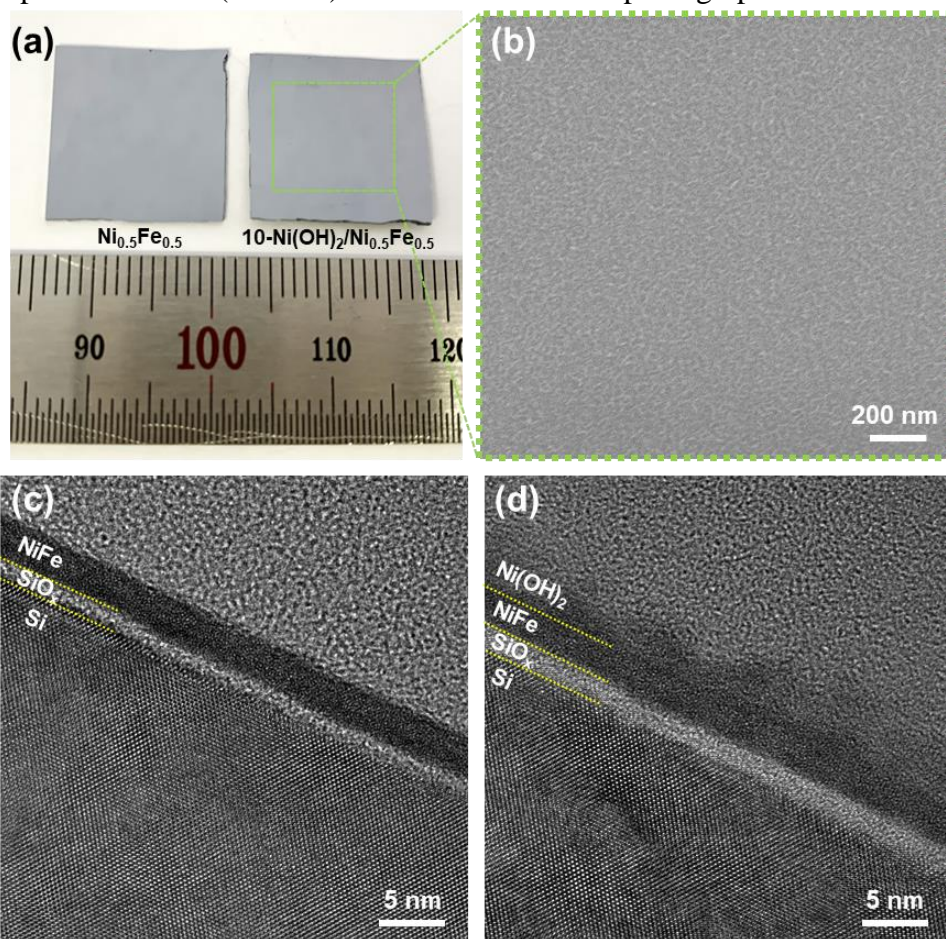
Figure 4.11 Morphology of the Si photoanodes. (a) Optical image of Ni$_{0.5}$Fe$_{0.5}$/SiO$_x$/n-Si and 10-Ni(OH)$_2$/Ni$_{0.5}$Fe$_{0.5}$/SiO$_x$/n-Si photoanodes. (b) FESEM image of 10-Ni(OH)$_2$/Ni$_{0.5}$Fe$_{0.5}$/SiO$_x$/n-Si. TEM images of (c) Ni$_{0.5}$Fe$_{0.5}$/SiO$_x$/n-Si and (d) 10-Ni(OH)$_2$/Ni$_{0.5}$Fe$_{0.5}$/SiO$_x$/n-Si photoanodes.

photoanodes with/without catalysts, the difference was indistinguishable by

the naked eyes (Figure 4.11(a)). The surface morphology of $Ni(OH)_2$ was analyzed by field emission scanning electron microscopy (FESEM). The faint morphology of $10-Ni(OH)_2$ was confirmed as shown in Figure 4.11(b). As the deposition time increases, the shape of the $Ni(OH)_2$ becomes distinct (Figure 4.12). To further characterize the structure of MIS samples, cross-section TEM analysis was conducted. As shown in Figure 4.11(c), conformal $Ni_{0.5}Fe_{0.5}$ thin film was formed on top of the SiO_x/Si. The thickness of $Ni_{0.5}Fe_{0.5}$ thin film and SiO_x were 3.5 nm and 1.5 nm, respectively. After the electrodeposition, 3 nm-thick $Ni(OH)_2$ was formed uniformly on $Ni_{0.5}Fe_{0.5}/SiO_x/n-Si$, and the thickness of the SiO_x layer was slightly
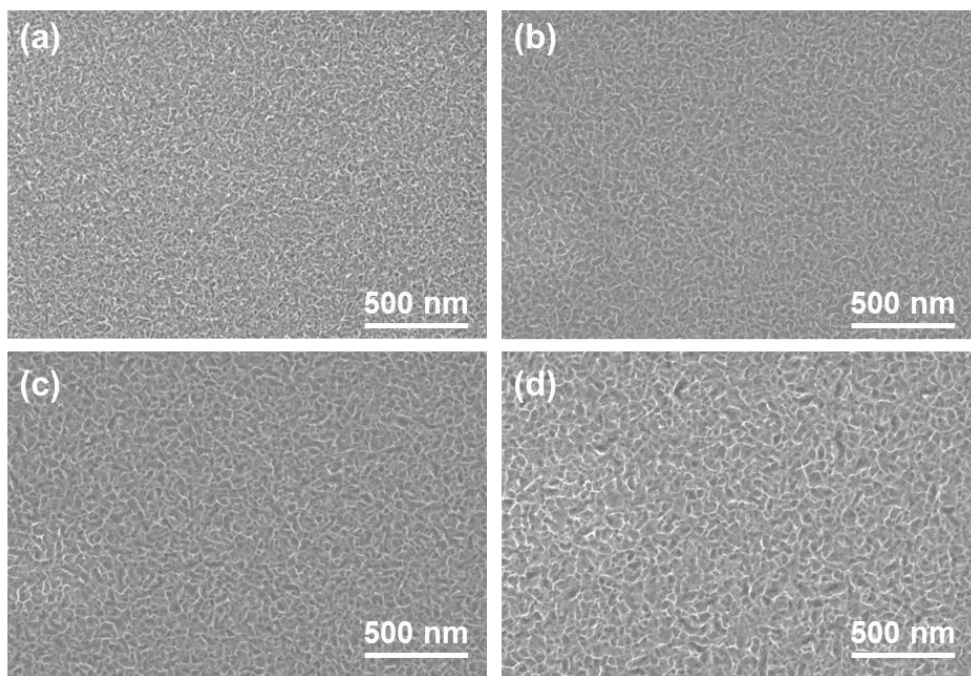
Figure 4.12 FESEM images of $x-Ni(OH)_2/Ni_{0.5}Fe_{0.5}/SiO_x/n-Si$. (a) 20s. (b) 40 s. (c) 60 s. (d) 80 s.

173

increased up to 1.8 nm (Figure 4.11(d)). A TEM equipped with an energy dispersive spectroscopy (EDS) was conducted to discriminate the elemental distributions of MIS photoanodes. The cross-sectional TEM images and EDS mappings show uniform thin film and Ni, Fe, and O distributions (Figure 4.13). The increase of Ni and O signals of $10\text{-}Ni(OH)_2/Ni_{0.5}Fe_{0.5}/SiO_x/n\text{-}Si$ indicates the presence of $Ni(OH)_2$. The formation of
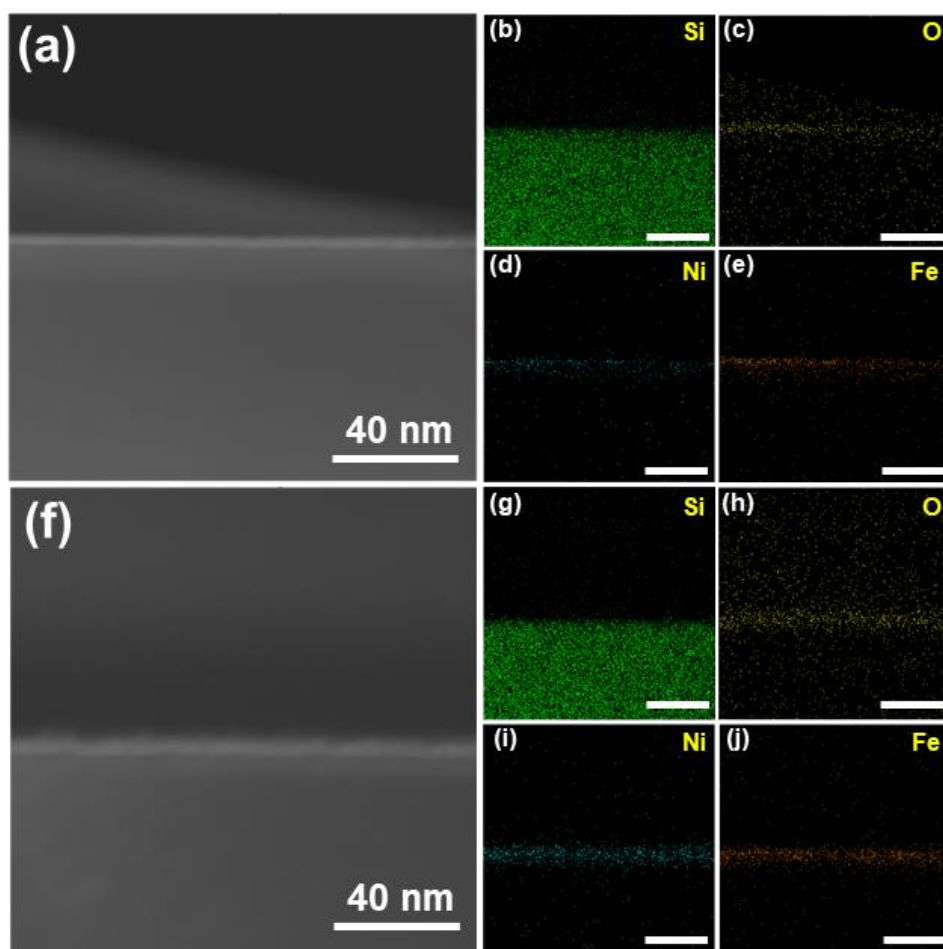
Figure 4.13 Cross-sectional TEM images of (a) $Ni_{0.5}Fe_{0.5}/SiO_x/n\text{-}Si$ and (f) $10\text{-}Ni(OH)_2/Ni_{0.5}Fe_{0.5}/SiO_x/n\text{-}Si$. Corresponding EDS maps of (b), (g) Si, (c), (h) O, (d), (i) Ni, and (e), (j) Fe.

Ni(OH)$_2$ on Ni$_{0.5}$Fe$_{0.5}$/SiO$_x$/n-Si was confirmed by XPS analysis, as shown in Figure 4.14(a-c). Compared to the XPS spectra of Ni$_{0.5}$Fe$_{0.5}$/SiO$_x$/n-Si, the metallic Ni 2p peak disappeared, and only the Ni^{2+} peak was observed at 855.5 eV. In the case of O 1s spectra, a significant M-OH peak was found at 530.9 eV.

The PEC performances of the MIS photoanodes with or without catalysts were evaluated in 1 M NaOH electrolyte under simulated 1 sun illumination in the three-electrode system. Figure 4.14(a) shows the *J-V* characteristics of the Ni$_{0.5}$Fe$_{0.5}$/SiO$_x$/n-Si photoanode with/without catalysts. The onset
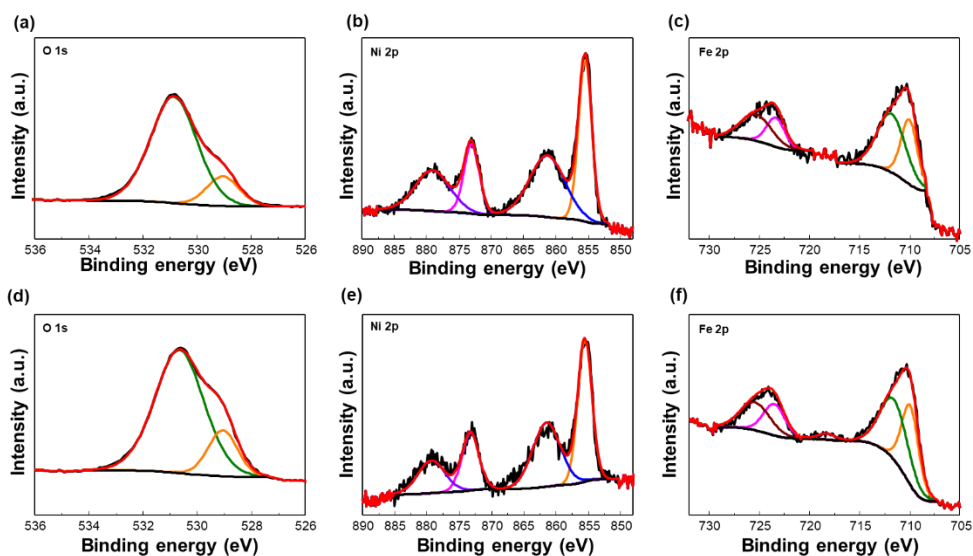
Figure 4.14 XPS spectra of 10-Ni(OH)$_2$/Ni$_{0.5}$Fe$_{0.5}$/SiO$_x$/n-Si before and after LSV measurements in 1 M NaOH. (a) O 1s, (b) Ni 2p, and (c) Fe 2p spectra of 10-Ni(OH)$_2$/Ni$_{0.5}$Fe$_{0.5}$/SiO$_x$/n-Si before LSV measurements. (d) O 1s, (e) Ni 2p, and (f) Fe 2p spectra of Ni(OH)$_2$/Ni$_{0.5}$Fe$_{0.5}$/SiO$_x$/n-Si after LSV measurements.

potential of $Ni_{0.5}Fe_{0.5}/SiO_x/n$-Si photoanode was 1.02 V vs. RHE, and

photocurrent density of 33.3 mA cm^{-2} was recorded at 1.23 V vs. RHE. After

introducing 10-Ni(OH)$_2$ catalysts on $Ni_{0.5}Fe_{0.5}/SiO_x/n$-Si photoanode, the

10-Ni(OH)$_2$/$Ni_{0.5}Fe_{0.5}/SiO_x/n$-Si showed 220 mV negative onset potential

than the water oxidation potential and the saturated current density of 41 mA

cm^{-2}, which reveals that thickness of the Ni(OH)$_2$ is adequate to display the

catalytic property without disturbing light absorption of silicon. After the

LSV measurements, Ni(OH)$_2$/$Ni_{0.5}Fe_{0.5}$ catalysts on SiO_x/n-Si maintained

the same chemical status as shown in Figure 4.14(d-f). I calculated the half-

cell solar-to-hydrogen conversion efficiencies (HC-STH) of photoanodes

from their LSV curves. As shown in Figure 4.16(a), the maximum HC-STH
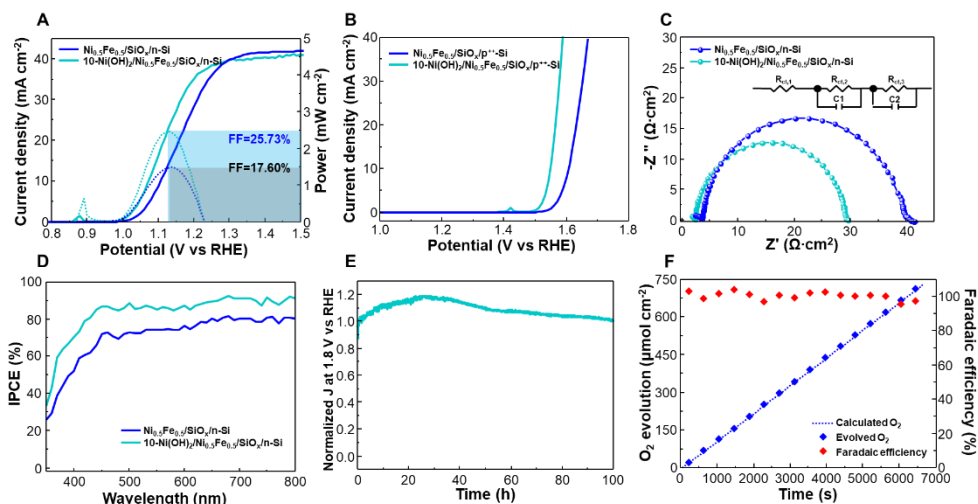
Figure 4.15 Water oxidation performances. LSV curves of (a) n-Si photoanodes and (b) p^{++}-Si anodes for water oxidation. (c) Nyquist plots of photoanodes. Inset shows the equivalent circuit. (d) IPCEs of Si photoanodes. (e) Stability test of 10-Ni(OH)$_2$/$Ni_{0.5}Fe_{0.5}/SiO_x/n$-Si in 1 M K-borate. (f) Faradaic efficiency and O$_2$ evolution of 10-Ni(OH)$_2$/$Ni_{0.5}Fe_{0.5}/SiO_x/n$-Si.

176

of 10-Ni(OH)$_2$/Ni$_{0.5}$Fe$_{0.5}$/SiO$_x$/n-Si photoanode reaches 2.5% at 1.13 V vs. RHE without buried junction, which exceeds the MIS photoanode without Ni(OH)$_2$ catalysts (1.5% at 1.14 V vs. RHE). As the thickness of Ni(OH)$_2$ increased, the height of the oxidation peak increased (Figure 4.16(b)). Since the thick Ni(OH)$_2$ layer disturbs the light absorption of Si, the saturated current density of x-Ni(OH)$_2$/Ni$_{0.5}$Fe$_{0.5}$/SiO$_x$/n-Si decreased from 40 mA cm^{-2} to 27 mA cm^{-2} while a slight change of onset potential was observed.

A factor indicating the cell's power efficiency is represented as a fill factor (FF). Fill factor is a concept used in photovoltaic and refers to the ratio of the product of current and voltage at the maximum output point to the product of short circuit current and open circuit voltage. From the rectangularity at the maximum power point, I calculated the FF of the
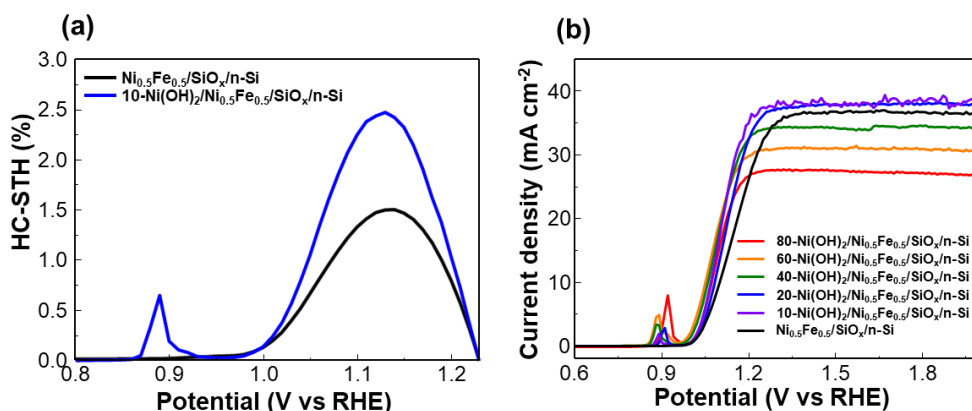
Figure 4.16 (a) HC-STHs of Ni$_{0.5}$Fe$_{0.5}$/SiO$_x$/n-Si and 10-Ni(OH)$_2$/Ni$_{0.5}$Fe$_{0.5}$/SiO$_x$/n-Si. (b) *J-V* curves of x-Ni(OH)$_2$/Ni$_{0.5}$Fe$_{0.5}$/SiO$_x$/n-Si in 1 M NaOH under 1sun illumination (100 mW cm^{-2}).

photoanodes by deriving the rectangularity of the *J-V* property, followed by the equation:

$$FF = \frac{I_{MP} \times (1.23 - V_{MP})}{I_{SC} \times (1.23 - V_{ON})}$$

, where the I_{MP} and V_{MP} are the current density and potential at the maximum power point, I_{SC} is the photocurrent density at 1.23 V vs RHE and E_{ON} is the onset potential. The power efficiency of the photoanode produced by applying FF to the photoelectrode was calculated. When the $Ni(OH)_2$ catalysts were introduced on $Ni_{0.5}Fe_{0.5}/SiO_x/n\text{-}Si$, FF was about 25.73%, showing an increase in efficiency by about 8% compared to the $Ni_{0.5}Fe_{0.5}/SiO_x/n\text{-}Si$. The increase of FF is advantageous in view of shifting the working potential toward a cathodic direction, leading to the construction of efficient pn PEC cells [40].

To investigate the electrochemical activity of the catalysts, I prepared the same catalysts on metallic p^{++}-Si, as shown in Figure 4.15(b). Prepared $Ni(OH)_2/Ni_{0.5}Fe_{0.5}/SiO_x/p^{++}\text{-}Si$ showed the overpotential (at 10 mA cm^{-2}) of 320 mV, which was 60 mV lower than that of $Ni_{0.5}Fe_{0.5}/SiO_x/p^{++}\text{-}Si$, expediting the OER activity. To investigate charge transport properties, electrochemical impedance spectroscopy (EIS) measurement was conducted near the onset potential of each photoanode (Figure 4.15(c)). In the Nyquist plot, small semicircles represent the fast charge transfer kinetics of the

178

photoanodes at the interface. The equivalent circuit which was used to fit the measured EIS spectra is shown in the inset. The equivalent circuit components are charge transfer resistance (R_{ct}) and capacitance element (C). The $R_{ct,1}$ represents the contact resistance of silicon, $R_{ct,2}$ the resistance between silicon and catalysts, and $R_{ct,3}$ the resistance between catalysts and electrolytes. The fitted values of resistance and capacitance of MIS photoanodes with/without catalysts are summarized in Table 4.2. By introducing catalysts, the smaller charge transfer resistance ($R_{ct,3}$) of the 10-$Ni(OH)_2/Ni_{0.5}Fe_{0.5}/SiO_x/n$-Si resulted in enhanced interfacial charge transfer.

Table 4.2. Charge transfer resistance of Si photoanodes.

Photoanodes	$R_{ct,1}$ ($\Omega \cdot cm^2$)	$R_{ct,2}$ ($\Omega \cdot cm^2$)	$R_{ct,3}$ ($\Omega \cdot cm^2$)
	Contact/n-Si	n-Si/catalysts	Catalysts/electrolyte
$Ni_{0.5}Fe_{0.5}/SiO_x/n$-Si	2.264	1.400	33.605
10-$Ni(OH)_2/$ $Ni_{0.5}Fe_{0.5}/SiO_x/n$-Si	0.196	2.205	26.701

Incident photon-to-current conversion efficiencies (IPCE) of MIS photoanodes with/without catalysts were conducted to investigate the effect of introducing $Ni(OH)_2$ catalysts. The IPCEs of the Si photoanodes were measured in 1 M NaOH electrolyte at an applied bias of 1.5 V vs. RHE, where photoanodes reach the saturated current density. As shown in Figure

179

4.15(d), both Si photoanodes showed the photo-response over the visible wavelength, which is well matched to the bandgap of silicon. By introducing $Ni(OH)_2$ catalysts, 10-$Ni(OH)_2$/$Ni_{0.5}Fe_{0.5}$/SiO_x/n-Si photoanode reached a value up to 90%, indicating high responsivity to the visible lights. The stability of the 10-$Ni(OH)_2$/$Ni_{0.5}Fe_{0.5}$/SiO_x/n-Si photoanode was evaluated under 1 sun illumination (100 mW cm^{-2}) in 1 M NaOH (pH 14) and 1 M K-borate (pH 9.5) electrolytes. Compared to the stability of MIS photoanode without $Ni(OH)_2$ catalysts (Figure 4.10(b)), 10-$Ni(OH)_2$/$Ni_{0.5}Fe_{0.5}$/SiO_x/n-Si photoanode showed improved stability up to 5 hours (Figure 4.17(a)). However, the rapid photocurrent drop was observed after 5 h, which is attributed to the instability of Fe in the alkaline electrolytes (Figure 4.10(c)). The fast photocurrent decay of 10-$Ni(OH)_2$/$Ni_{0.5}Fe_{0.5}$/SiO_x/n-Si photoanode
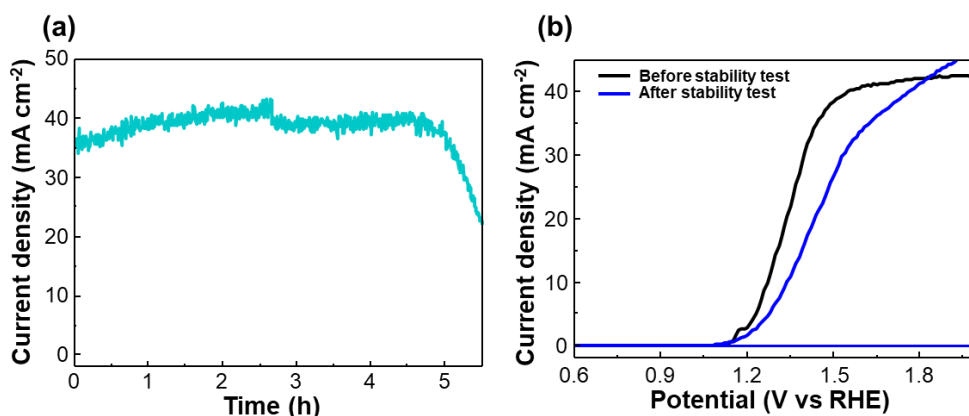

Figure 4.17 (a) Chronoamperometry curve of 10-$Ni(OH)_2$/$Ni_{0.5}Fe_{0.5}$/SiO_x/n-Si measured at 1.5 V vs. in 1 M K-borate electrolyte under 1sun illumination. (b) LSV curves of 10-$Ni(OH)_2$/$Ni_{0.5}Fe_{0.5}$/SiO_x/n-Si before and after stability test.

was significantly alleviated in mild alkaline 1 M K-borate electrolyte. As shown in Figure 4.15(e), the decrease in photocurrent was not observed for 100 h operation at a constant potential of 1.8 V vs. RHE. After a continuous 100 h chronoamperometric measurement, slight degradation in PEC performance was confirmed (Figure 4.17(b)). By comparing the stability in alkaline electrolytes with different pH, it can be derived that corrosion of $Ni(OH)_2/Ni_{0.5}Fe_{0.5}$ can be largely suppressed in the mild electrolyte. To further investigate whether photogenerated charge carriers are consumed for oxygen evolution reaction, the oxygen evolution of 10-$Ni(OH)_2/Ni_{0.5}Fe_{0.5}/SiO_x/n$-Si photoanode was measured by gas chromatography at 1.8 V vs. RHE. As shown in Figure 4.15(f), the Faradaic efficiency value was close to 100% during the measurements, which indicates that all photogenerated holes are consumed for water oxidation without any side reactions. A few points showed higher than 100%, attributed to the generated O_2 bubbles attached to the photoanode surface. The measured amount of oxygen increased in proportion to time, consistent with the calculated theoretical amount of oxygen generation.

The photovoltage is a driving force to induce spontaneous PEC water splitting without an external bias. Through a series of experiments, optimized MIS photoanodes with oxygen evolving catalysts, generating a

photovoltage of 500 mV. However, still, the generated photovoltage is not ample for spontaneous water splitting reaction. The design of devices such as PV-electrolyzer (EC), PV-PEC, and PEC-PEC tandem cells has been considered as a promising approach to achieve clean hydrogen without applying bias [41–45]. To make up for insufficient photovoltage output of Si photoanodes, I fabricated wired perovskite/Si tandem solar cell with the photoanode to supply ample photo-induced voltage. The schematic shown in Figure 4.18(a) demonstrated that both solar cell and photoanode were in parallel light illumination with an area ratio of 1:1. The structure of the monolithic perovskite/Si tandem solar cell is illustrated in Figure 4.19(a). By designing an optimal bandgap configuration of 1.7 eV/1.12 eV as light absorbers, perovskite/Si tandem solar cell showed the open circuit voltage (V_{oc}) of 1.8 V and the short circuit current of 19.3 mA cm^{-2} (Figure 4.19(b)) [46]. Under the two-electrode system, J-V curves of perovskite/Si tandem
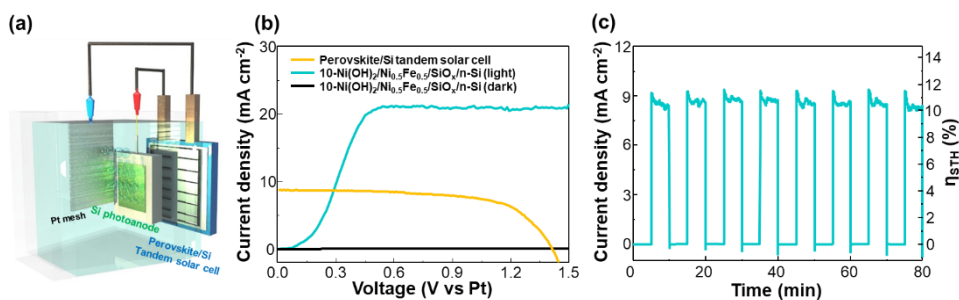
Figure 4.18 PV-PEC tandem cell configuration and PEC performance. (a) Schematic of wire-connected tandem cell. (b) 2-electrode J-V curves of the 10-Ni(OH)$_2$/Ni$_{0.5}$Fe$_{0.5}$/SiO$_x$/n-Si photoanode and perovskite/Si tandem solar cell under AM 1.5G irradiation. (c) Chronoamperometry of unassisted water splitting under 1 sun illumination.

solar cell and 10-Ni(OH)$_2$/Ni$_{0.5}$Fe$_{0.5}$/SiO$_x$/n-Si photoanode are shown in Figure 4.18(b). The intersection of *J-V* curves indicates achievable photocurrent (operating current, J$_{op}$) without applying external bias. I can estimate the solar-to-hydrogen (STH) conversion efficiency (η_{STH}) of the PV-PEC tandem device using this point by the following equation:

$$\eta_{STH} = \frac{1.23\,V\,\times\,J_{op}\,(mA\,cm^{-2})}{100\,mW\,cm^{-2}}$$

The expected η_{STH} of PV-PEC tandem device is 10.77% by using J$_{op}$ of 8.75 mA cm^{-2}. The actual unassisted water splitting performance of the PV-PEC tandem device was characterized by chronoamperometry measurements at zero bias with chopped light. As shown in Figure 4.18(c), the current density of 8.8 mA cm^{-2} is achieved without external bias and practical η_{STH} matches to 10.8% during operation for 80 min.
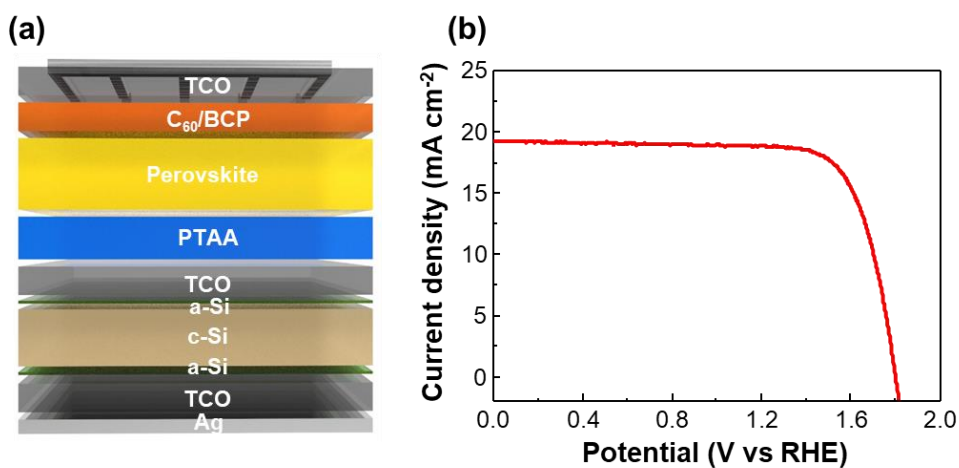
Figure 4.19 (a) Schematic of the perovskite/Si tandem cell. (b) *J-V* curve of the perovskite tandem device.

4.3.4. Catalysts of urea oxidation reaction

Urea oxidation reaction (UOR) is one of the promising reactions in the view of hydrogen production and pollutant treatment [47]. Similar to the water electrolysis, urea electrolysis produces H_2 at the cathode using the electrical current. At the anode side, the urea oxidation reaction produces CO_2 and N_2 instead of O_2 evolution. The overall urea electrolysis reaction is presented as the following equation:

$$\text{Anode: } Co(NH_2)_2 + 6OH^- \rightarrow CO_2 + N_2 + 5H_2O + 6e^-$$

$$\text{Cathode: } 6H_2O + 6e- \rightarrow 3H_2 + 6OH^-$$

$$\text{Overall: } Co(NH_2)_2 + H_2O \rightarrow CO_2 + N_2 + 3H_2$$
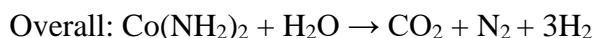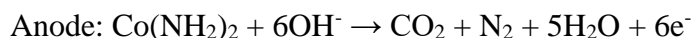
The theoretically required voltage for urea splitting is 0.37 V which is quite lower than that of water splitting (1.23 V) [48]. Urea is a naturally abundant source, originating from fertilizers, urines, industrial production wastes, and so on. The oxidation of urea is advantageous for its relatively low volatility, high energy density (16.9 mJ L^{-1}) in liquid fuels, and high solubility [49]. Although UOR is a complicated 6-electron transfer process [6], urea can be used as sacrificial agents and more easily oxidized species in the water electrolysis electrolytes to overcome sluggish water oxidation reaction [5]. The inclusion of urea in the electrolytes can be considered as natural electrolytes. I investigated the EC/PEC UOR performance of

fabricated MIS photoanodes. Figure 4.20(a) shows J-V curves of p^{++}-Si

electrodes for UOR in 1 M NaOH + 0.33 M urea, where 0.33 M of urea is

approximately the average molar concentration of urea in human urine [5].

Similar to the activity of OER, $Ni/SiO_x/p^{++}$-Si showed a large urea oxidation

peak, while $Fe/SiO_x/p^{++}$-Si didn't show any UOR property. The CV curves

of p^{++}-Si demonstrated the (Figure 4.20(b)). Figure 4.20(c) shows the LSV

curves of n-Si photoanodes in the same electrolytes (1 M NaOH + 0.33 M

urea). Compared to the electrochemical UOR properties of p^{++}-Si, 10-
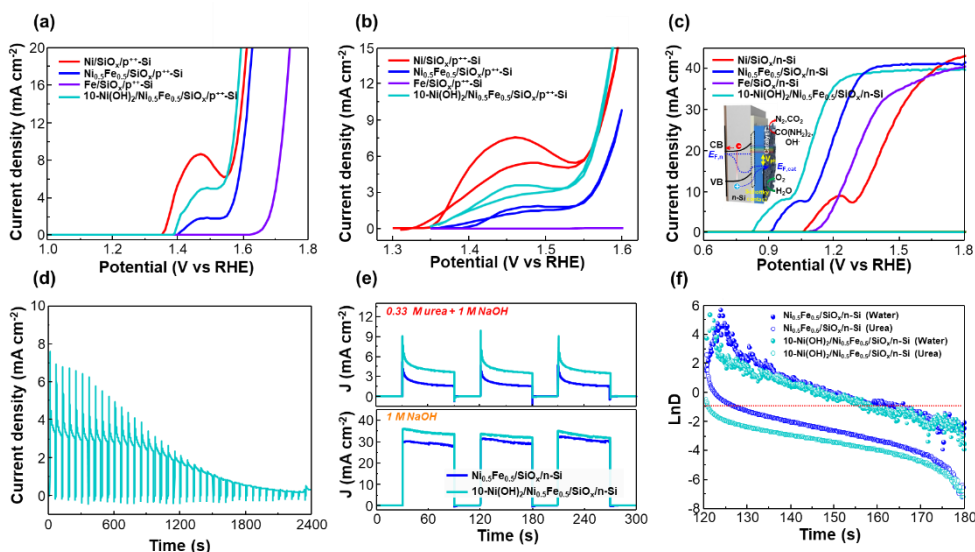
Figure 4.20 Electrochemical and photoelectrochemical urea oxidation performances. (a) J-V curves and (b) CV curves of p^{++}-Si anodes for urea oxidation in 1 M NaOH + 0.33 M urea. (c) LSV curves of n-Si photoanodes and (d) Chronoamperometry curve of 10-$Ni(OH)_2/Ni_{0.5}Fe_{0.5}/SiO_x/n$-Si measured at 1 V vs RHE in 0.33 M urea + 1 M NaOH electrolyte under 1 sun illumination with chopped light. (e) Comparison of chronoamperometry of photoanodes with chopped light under AM 1.5G. (f) ln D-time curve. The transient time constant is defined as the time when ln D = -1.

Ni(OH)$_2$/Ni$_{0.5}$Fe$_{0.5}$/SiO$_x$/n-Si showed the lowest onset potential of 0.83 V vs RHE, which indicates that additional Ni(OH)$_2$ catalyst is efficient not only for OER but also for UOR. Fe/SiO$_x$/n-Si showed the onset potential of 1.13 V vs. RHE, similar to that of water oxidation (1.14 V vs. RHE). From the results, it can be estimated that Fe is not the appropriate catalyst for UOR. HC-STH conversion efficiencies for UOR were calculated based on the *J-V* curves of Si photoanodes. As shown in Figure 4.20(d), the stability of 10-Ni(OH)$_2$/Ni$_{0.5}$Fe$_{0.5}$/SiO$_x$/n-Si gradually decreased within 30 minutes, while 5 h stability was recorded in 1 M NaOH electrolytes as shown in Figure 4.17(a). I compared the chronoamperometric curves of UOR (at 1 V vs. RHE in 1 M NaOH + 0.33 M urea) and OER (at 1.23 V vs. RHE in 1 M NaOH) of Si photoanodes to evaluate transient photocurrent decay. When the light was switched on, Si photoanodes showed a photocurrent spike and exponentially decayed to the steady-state during UOR, while the overshoots were not observed during OER (Figure 4.20(e)). The presence of a photocurrent spike was the result of photogenerated electron-hole recombination. From the results, the UOR activity of Si photoanodes was hindered by charge recombination, which accelerates the degradation of the stability. I calculated the transient decay time from a logarithmic plot of parameter D, following by the equation:

$$D = \frac{(I_t - I_s)}{(I_m - I_s)}$$

, where I_t is the photocurrent at a time (t), I_m and I_s are the photocurrent spike and steady-state photocurrent, respectively. The transient decay time is defined when $\ln D = -1$. Figure 4.20(f) shows that both Si photoanodes showed similar transient decay times for water oxidation reaction. However, in the case of UOR, the transient decay time decreased compared to that of OER, and introducing $Ni(OH)_2$ contributes to the charge recombination, although it shifted the onset potential of 90 mV compared to the $Ni_{0.5}Fe_{0.5}/SiO_x/n$-Si.

By integrating the OER and UOR performances of Si photoanodes in the view of photovoltages and onset potentials, composition controlled $Ni_{0.5}Fe_{0.5}$ and electrodeposited $Ni(OH)_2$ catalysts are active toward both reactions, as shown in Figure 4.21.
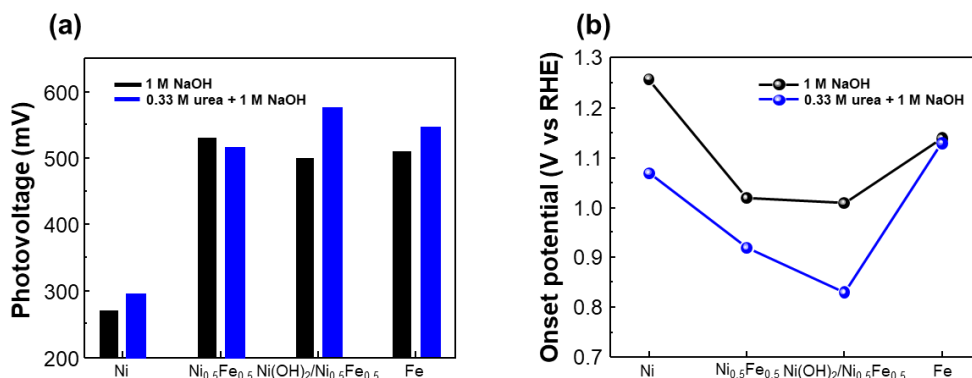

Figure 4.21 Comparison of (a) photovoltage and (b) onset potentials of $Ni/SiO_x/n$-Si, $Ni_{0.5}Fe_{0.5}/SiO_x/n$-Si, $Fe/SiO_x/n$-Si, and 10-$Ni(OH)_2/Ni_{0.5}Fe_{0.5}/SiO_x/n$-Si.

4.4. Conclusion

I demonstrated the interface engineering of MIS photoanodes and investigated their PEC water and urea oxidation performances. First, I prepared different insulating SiO_x layers by chemical etching method ($SiO_{x,RCA}$, $SiO_{x,BOE}$) and showed that control of SiO_x layer between a metal layer and semiconducting n-Si affected the surface status and interface properties, influencing the PEC performances. Second, I showed that composition control of metallic Ni_xFe_{1-x} thin films shows opposite properties with electrochemical properties and photoelectrochemical properties, where Ni-rich films showed lower overpotentials for EC water oxidation. However, Fe-rich films showed lower onset potentials for PEC water oxidation. There was a trade-off between the stability and the onset potentials depending on the presence of Fe. The optimized $Ni_{0.5}Fe_{0.5}/SiO_x$/n-Si photoanodes showed a high photocurrent density of 33.3 mA cm^{-2} at 1.23 V vs. RHE. By introducing additional $Ni(OH)_2$ catalysts on $Ni_{0.5}Fe_{0.5}/SiO_x$/n-Si photoanodes, enhanced fill factor over 25% and external quantum efficiency of 90% was achieved. By introducing perovskite/Si tandem solar cell as a voltage supplier, wired tandem cell device generated an operating photocurrent density of 8.8 mA cm^{-2}, corresponding to the STH conversion efficiency of 10.8%. Lastly, I also investigated PEC urea oxidation properties of Si photoanodes. The heterogeneous $Ni(OH)_2/Ni_{0.5}Fe_{0.5}/SiO_x$/n-

Si photoanode showed a highly active urea oxidation property, showing the potential of Si photoanodes for an additional utility of anodic reactions. Although some issues such as stability that must be solved still remain in view of adjusting for industrial applications, these findings suggest the design of efficient MIS photoanodes to produce hydrogen in polluted water.

4.5. References

[1]   D. Bae, B. Seger, P. C. K. Vesborg, O. Hansen, I. Chorkendorff, *Chem. Soc. Rev.*, **2017**, 46, 1933.

[2]   M. S. Prévot, K. Sivula, *J. Phys. Chem. C*, **2013**, 117, 17879.

[3]   S. S. M. Bhat, S. A. Lee, T. H. Lee, C. Kim, J. Park, T. W. Lee, S. Y. Kim, H. W. Jang, *ACS Appl. Energy Mater.*, **2020**, 3, 5646.

[4]   T. H. Lee, S. A. Lee, H. Park, M. J. Choi, D. Lee, H. W. Jang, *ACS Appl. Energy Mater.*, **2020**, 3, 1634.

[5]   B. Zhu, Z. Liang, R. Zou, *Small*, **2020**, 16, 1906133.

[6]   D. Xu, Z. Fu, D. Wang, Y. Lin, Y. Sun, D. Meng, T. Feng Xie, *Phys. Chem. Chem. Phys.*, **2015**, 17, 23924.

[7]   J. Liu, J. Li, M. Shao, M. Wei, *J. Mater. Chem. A*, **2019**, 7, 6327.

[8]   S. A. Lee, S. Choi, C. Kim, J. W. Yang, S. Y. Kim, H. W. Jang, *ACS Mater. Lett.*, **2020**, 2, 107.

[9]   G. Loget, *Curr. Opin. Colloid Interface Sci.*, **2019**, 39, 40.

[10]   S. A. Lee, T. H. Lee, C. Kim, M. G. Lee, M. J. Choi, H. Park, S. Choi, J. Oh, H. W. Jang, *ACS Catal.*, **2018**, 8, 7261.

[11]   L. M. Peter, *Electroanalysis*, **2015**, 27, 864.

[12]   X. Zhou, R. Liu, K. Sun, K. M. Papadantonakis, B. S. Brunschwig, N .S. Lewis, *Energy Environ. Sci.*, **2016**, 9, 892.

[13]   S. A. Lee, T. H. Lee, C. Kim, M. J. Choi, H. Park, S. Choi, J. Lee, J. Oh, S. Y. Kim, H. W. Jang, *ACS Catal.*, **2020**, 10, 420.

[14]   M. J. Kenney, M. Gong, Y. Li, J. Z. Wu, J. Feng, M. Lanza, H. Dai, *Science*, **2013**, 342, 836.

[15]   Y. Yu, C. Sun, X. Yin, J. Li, S. Cao, C. Zhang, P. M. Voyles, X. Wang, *Nano Lett.*, **2018**, 18, 5335.

[16]   A. G. Scheuermann, J. P. Lawrence, K. W. Kemp, T. Ito, A. Walsh, C. E. D. Chidsey, P. K. Hurley, P. C. McIntyre, *Nat. Mater.*, **2016**, 15, 99.

[17]   B. Liu, S. Feng, L. Yang, C. Li, Z. Luo, T. Wang, J. Gong, *Energy Environ. Sci.*, **2020**, 13, 221.

[18]   Z. Luo, B. Liu, H. Li, X. Chang, W. Zhu, T. Wang, J. Gong, *Small Methods*, **2019**, 3, 1900212.

[19]   Y. W. Chen, J. D. Prange, S. Dühnen, Y. Park, M. Gunji, C. E. D. Chidsey, P. C. McIntyre, *Nat. Mater.*, **2011**, 10, 539.

[20]   J. Hemmerling, J. Quinn, S. Linic, *Adv. Energy Mater.*, **2020**, 10, 1903354.

[21]   I. A. Digdaya, G. W. P. Adhyaksa, B. J. Trześniewski, E. C. Garnett, W. A. Smith, *Nat. Commun.*, **2017**, 8, 15968.

[22]   G. Loget, C. Mériadec, V. Dorcet, B. Fabre, A. Vacher, S. Fryars, S. Ababou-Girard, *Nat. Commun.*, **2019**, 10, 3522.

[23]   P. Aroonratsameruang, P. Pattanasattayavong, V. Dorcet, C. Mériadec, S. Ababou-Girard, S. Fryars, G. Loget, *J. Phys. Chem. C*, **2020**, 124, 25907.

[24]   J. Dabboussi, R. Abdallah, L. Santinacci, S. Zanna, A. Vacher, V. Dorcet, S. Fryars, D. Floner, G. Loget, *J. Mater. Chem. A*, **2022**, 10, 19769.

[25]   J. K. Bal, S. Kundu, S. Hazra, *Chem. Phys. Lett.*, **2010**, 500, 90.

[26]   G. Kissinger, W. Kissinger, *Phys. Status Solidi A*, **1991**, 123, 185.

[27]   X. F. Lu, X. Y. Chen, W. Zhou, Y. X. Tong, G. R. Li, *ACS Appl. Mater. Interfaces*, **2015**, 7, 14843.

[28]   L. Li, P. Ma, S. Hussain, L. Jia, D. Lin, X. Yin, Y. Lin, Z. Cheng, L. Wang, *Sustain. Energy Fuels*, **2019**, 3, 1749.

[29]   R. Pai, A. Singh, S. Simotwo, V. Kalra, *Adv. Engineering Mater.*, **2018**, 20, 1701116.

[30]   J. Liu, E. Lee, Y. T. Kim, Y. U. Kwon, *Nanoscale*, **2014**, 6, 10643.

[31] Y. Kumar, A. Sharma, M. A. Ahmed, S. S. Mali, C. K. Hong, P. M. Shirage, *New J. Chem.*, **2018**, 42, 15793.

[32] H. Yao, J. A. Woollam, S. A. Alterovitz, *Appl. Phys. Lett.*, **1993**, 62, 3324.

[33] H. Zhang, Y. Lu, C. D. Gu, X. L. Wang, J. P. Tu, *CrystEngComm*, **2012**, 14, 7942.

[34] X. Wang, B. Zhang, W. Zhang, M. Yu, L. Cui, X. Cao, J. Liu, *Sci. Rep.*, **2017**, 7, 1584.

[35] K. Zhang, X. Xia, S. Deng, Y. Zhong, D. Xie, G. Pan, J. Wu, Q. Liu, X. Wang, J. Tu, *Nano-Micro Lett.*, **2019**, 11, 21.

[36] N. Hao, Y. Wei, J. Wang, Z. Wang, Z. Zhu, S. Zhao, M. Han, X. Huang, *RSC Adv.*, **2018**, 8, 20576.

[37] X. L. Yang, Y. W. Lv, J. Hu, J. R. Zhao, G. Y. Xu, X. Q. Hao, P. Chen, M. Q. Yan, *RSC Adv.*, **2021**, 11, 17352.

[38] I. A. Digdaya, B. J. Trześniewski, G. W. P. Adhyaksa, E. C. Garnett, W. A. Smith, *J. Phys. Chem. C*, **2018**, 122, 5462.

[39]   D. Y. Chung, P. P. Lopes, P. Farinazzo Bergamo Dias Martins, H. He, T. Kawaguchi, P. Zapol, H. You, D. Tripkovic, D. Strmcnik, Y. Zhu, S. Seifert, S. Lee, V. R. Stamenkovic, N. M. Markovic, *Nat. Energy*, **2020**, 5, 222.

[40]   Y. Pihosh, T. Minegishi, V. Nandal, T. Higashi, M. Katayama, T. Yamada, Y. Sasaki, K. Seki, Y. Suzuki, M. Nakabayashi, M. Sugiyama, K. Domen, *Energy Environ. Sci.*, **2020**, 13, 1519.

[41]   J. W. Yang, I. J. Park, S. A. Lee, M. G. Lee, T. H. Lee, H. Park, C. Kim, J. Park, J. Moon, J. Y. Kim, H. W. Jang, *Appl. Catal. B*, 293, 2021, 120217.

[42]   H. Lee, J. W. Yang, J. Tan, J. Park, S. G. Shim, Y. S. Park, J. Yun, K. Kim, H. W. Jang, J. Moon, *Adv. Sci.*, **2021**, 2102458.

[43]   R. Fan, S. Cheng, G. Huang, Y. Wang, Y. Zhang, S. Vanka, G. A. Botton, Z. Mi, M. Shen, *J. Mater. Chem. A*, **2019**, 7, 2200.

[44]   S. A. Lee, I. J. Park, J. W. Yang, J. Park, T. H. Lee, C. Kim, J. Moon, J. Y. Kim, H. W. Jang, *Cell Rep. Phys. Sci.*, **2020**, 1, 100219.

[45]   H. Park, I. J. Park, M. G. Lee, K. C. Kwon, S. P. Hong, D. H. Kim, S. A. Lee, T. H. Lee, C. Kim, C. W. Moon, D. Y. Son, G. H. Jung, H. S. Yang, J. R. Lee, J. Lee, N. G. Park, S. Y. Kim, J. Y. Kim, H. W. Jang, *ACS Appl. Mater. Interfaces*, **2019**, 11, 33835.

[46] D. Kim, H. Joon Jung, I. Jae Park, B. W. Larson, S. P. Dunfield, C. Xiao, J. Kim, J. Tong, P. Boonmongkolras, S. Geun Ji, F. Zhang, S. R Pae, M. Kim, S. B. Kang, V. Dravid, J. J. Berry, J. Young Kim, K. Zhu, D. Hoe Kim, B. Shin, *Science*, **2020**, 368, 155.

[47] X. Hu, J. Zhu, J. Li, Q. Wu, *ChemElectroChem*, **2020**, 7, 3211.

[48] X. Ji, Y. Zhang, Z. Ma, Y. Qiu, *ChemSusChem*, **2020**, 13, 5004.

[49] W. Xu, Z. Wu, S. Tao, *Energy Technol.*, **2016**, 4, 1329.

Summary

First, a new photoanode comprising nanoporous $BiVO_4$ and SnO_2 nanorods was design to enhance the charge separation via structural and interfacial engineering. $BiVO_4/SnO_2$ photoanode exhibited not only remarkable charge separation efficiency of 97% but also, by loading NiFe as a co-catalyst for water oxidation, high photocurrent density of 5.61 mA cm^{-2} at 1.23 V versus the reversible hydrogen electrode under front-side 1 sun illumination. Consequently, a tandem cell comprising NiFe/$BiVO_4/SnO_2$ photoanode and perovskite/Si tandem solar cell generated an operating photocurrent density of 5.90 mA cm^{-2} with a solar-to-hydrogen conversion efficiency of 7.3% in zero-bias.

Second, first introduce In_2O_3 nanorods were firstly introduced as a novel electron transport layer for $BiVO_4$ with a short charge diffusion length. In_2O_3 NRs reinforced the electron transport and hole blocking of $BiVO_4$, surpassing the state-of-the-art photoelectrochemical performances of $BiVO_4$-based photoanodes. Also, a tannin-nickel-iron complex was used as an oxygen evolution catalyst to quicken the reaction kinetics. The final TANF/$BiVO_4/In_2O_3$ NRs photoanode generated photocurrent densities of 7.1 mA cm^{-2} in sulfite oxidation and 4.2 mA cm^{-2} in water oxidation at

1.23 V versus the reversible hydrogen electrode. Furthermore, the "artificial leaf," which is a tandem cell with a perovskite/silicon solar cell, exhibited a solar-to-hydrogen conversion efficiency of 6.2% for unbiased solar water splitting. It was revealed that significant advances in photoactivity of TANF/$BiVO_4$/In_2O_3 NRs came from the tailored nanostructure and band structure for charge dynamics.

Third, Si photoelectrodes were fabricated by using metal-insulator-semiconductor heterostructures for efficient charge separation and transfer to apply the photoelectrochemical water and urea oxidation. With controls of the native SiO_x insulator layer and catalytic NiFe metal layer, Si photoelectrode exhibited a photovoltage of 530 mV and a photocurrent density of 33.3 mA cm^{-2} at 1.23 V versus reversible hydrogen electrode. Further employed $Ni(OH)_2$ catalysts allowed Si photoanode to achieve fill factor of 25.73% and solar-to-hydrogen conversion efficiency of 10.8% with a perovskite/Si tandem solar cell. The fabricated $Ni(OH)_2$/NiFe/n-Si photoanode showed considerable performances toward urea oxidation.

List of Publications

[1]   S. A Lee, S. Choi, C. Kim, **J. W. Yang**, S. Y. Kim*, H. W. Jang, *ACS Mater. Lett.*, **2020**, 2, 107.

[2]   S. A Lee, I. J. Park, **J. W. Yang**, J. Park, T. H. Lee, C. Kim, J. Moon, J. Y. Kim, H. W. Jang, *Cell Rep. Phys. Sci.,* **2020**, 1, 100219.

[3]   H. Park, H. Ahn, T. H. Lee, J. Y. Lee, M. G. Lee, S. A Lee, **J. W. Yang**, S. J. Kim, S. H. Ahn, S. Y. Kim, C. H. Lee, E. S. Park, H. W. Jang, *Small Methods*, **2020**, 5, 2000755.

[4]   **J. W. Yang**, S. H. Ahn, H. W. Jang, *Curr. Opin. Green. Sustain. Chem.*, **2021**, 29, 100454.

[5]   S. E. Jun, S. Choi, S. Choi, T. H. Lee, C. Kim, **J. W. Yang**, W. O. Choe, I. H. Im, C. J. Kim, H. W. Jang, *Nano-Micro Lett.*, **2021**, 13, 81.

[6]   **J. W. Yang**, I. J. Park, S. A Lee, M. G. Lee, T. H. Lee, H. Park, C. Kim, J. Park, J. Moon, J. Y. Kim, H. W. Jang, *Appl. Catal. B*, **2021**, 293, 120217.

[7]   T. H. Eom, S. H. Cho, J. M. Suh, T. Kim, T. H. Lee, S. E. Jun, **J. W. Yang**, J. Lee, S. H. Hong, H. W. Jang, *J. Mater. Chem. A* **2021**, 9, 11168.

[8]   C. W. Lee, J. M. Suh, S. Choi, S. E. Jun, T. H. Lee, **J. W. Yang**, S. A Lee, B. R. Lee, D. Yoo, S. Y. Kim, H. W. Jang, *npj 2D Mater. Appl.*, **2021**, 5, 39.

[9]   J. Park, T. H. Lee, C. Kim, S. A Lee, M. J. Choi, H. Kim, **J. W. Yang**, J. Lim, H. W. Jang, *Appl. Catal. B*, **2021**, 295, 120276.

[10]   S. E. Jun, S. P. Hong, S. Choi, C. Kim, S. G. Ji, I. J. Park, S. A Lee, **J. W. Yang**, T. H. Lee, W. Sohn, J. Y. Kim, H. W. Jang, *Small*, **2021**, 17, 2103457.

[11]   H. Lee, **J. W. Yang**, J. Tan, J. Park, S. G. Shim, Y. S. Park, J. Yun, K. Kim, H. W. Jang, J. Moon, *Adv. Sci.*, **2021**, 8, 2102458.

[12]   S. A Lee, **J. W. Yang**, S. Choi, H. W. Jang, *Exploration*, **2021**, 1, 20210012.

[13]   S. J. Kim, T. H. Lee, J..M. Yang, **J. W. Yang**, Y. J. Lee, M.J. Choi, S. A Lee, J. M. Suh, K. J. Kwak, J. H. Baek, I. H. Im, D. E. Lee, J. Y. Kim, J. Kim, J. S. Han, S. Y. Kim, D. Lee, N. G. Park, H. W. Jang, *Mater. Today*, **2021**, 52, 19.

[14]   M. J. Choi, T. L. Kim, K. S. Choi, W. Sohn, T. H. Lee, S. A Lee, H. Park, S. Y. Jeong, **J. W. Yang**, S. Lee, H. W. Jang, *ACS Appl. Mater. Interfaces*, **2022**, 6, 7788.

[15]   H. Park, J. W. Bae, T. H. Lee, I. J. Park, C. Kim, M. G. Lee, S. A Lee, **<u>J. W. Yang</u>**, M. J. Choi, S. H. Hong, S. Y. Kim, S. H. Ahn, J. Y. Kim, H. W. Jang, *Small.*, **2022**, 18, 2105611.

[16]   T. H. Eom, S. H. Cho, J. M. Suh, T. Kim, **<u>J. W. Yang</u>**, T. H. Lee, S. E. Jun, S. J. Kim, J. Lee, S. H. Hong, H. W. Jang, *Small*, **2022**, 18, 2106613.

[17]   M. G. Lee, **<u>J. W. Yang</u>**, H. Park, C. W. Moon, D. M. Andoshe, J. Park, C. K. Moon, T. H. Lee, K. S. Choi, W. S. Cheon, J. J. Kim, H. W. Jang, *Nano-Micro Lett.*, **2022**, 14, 48.

[18]   B. R. Lee, S. Choi, W. S. Cheon, **<u>J. W. Yang</u>**, M. G. Lee, S. H. Park, H. W. Jang, *Electronic Mater. Lett.*, **2022**, 391.

[19]   S. A Lee, **<u>J. W. Yang</u>**, T. H. Lee, I. J. Park, C. Kim, S. H. Hong, H. Lee, S. Choi, J. Moon, S. Y. Kim, J. Y. Kim, H. W. Jang, *Appl. Catal. B*, **2022**, 317, 121765.

[20]   M. G. Lee, **<u>J. W. Yang</u>**, H. R. Kwon, H. W. Jang, *CrystEngComm*, **2020**, 24, 5838.

[21]   I. H. Im, S. J. Kim, J. H. Baek, K. J. Kwak, T. H. Lee, **<u>J. W. Yang</u>**, D. E. Lee, J. Y. Kim, H. R. Kwon, D. Y. Heo, S. Y. Kim, H. W. Jang, *Adv. Funct. Mater.*, **2022**, 24, 2211358.

[22]   S. Moon, J. Park, H. Lee, **J. W. Yang**, J. Yun, Y. S. Park, J. Lee, H. Im, H. W. Jang, W. Yang, J. Moon, *Adv. Sci.*, **2023**, 2206286.

[23]   M. G. Lee, **J. W. Yang**, I. J. Park, T. H. Lee, H. Park, W. S. Cheon, S. A. Lee, H. Lee, J. M. Suh, J. Moon, J. Y. Kim, H. W. Jang, *Carbon Energy*, **2023**, 24, e321.

Abstract (in Korean)

수소는 연소 시 탄소를 방출하지 않는다는 점에서 화석 연료의 대안 및 미래 에너지 캐리어로서 그 수요가 늘어나고 있다. 그러나 화석 연료 개질 방식의 현 수소 생산은 공정 중에 이산화탄소를 방출하는 회색 수소이다. 전과정에서 이산화탄소 방출이 없는 녹색 수소 생산을 위해서는 재생 에너지의 도입이 필요하며 그중 태양광 에너지를 이용한 광전기화학적 수전해는 가장 유망한 수소 생산 방식이다. 수전해 반응에 적절한 밴드구조를 가지는 비스무트 바나데이트는 가장 유망한 광양극 소재 중 하나이다. 그러나 짧은 정공 확산 거리로 인한 전하 재결합 문제와 느린 표면 반응 속도로 인한 광부식 문제가 존재한다. 고효율의 광양극으로 이용하기 위해서는 광양극의 나노구조화 및 조촉매의 도입이 요구된다. 실리콘 역시 유망한 광양극 재료 중 하나이다. 작은 밴드갭으로 인해 넓은 영역의 빛을 흡수할 수 있고, 긴 정공 확산 거리는 전하 재결합을 억제한다. 자체 촉매 특성이 현저히 낮으며, 산소발생반응 준위보다 낮은 자가 산화 준위로 인한 낮은 광 안정성 및 밴드 위치로 인해 광전류를 거의 발생시키지 않는다. 따라서, 실리콘을 고효율

물분해 광전극으로 응용하기 위해 산소발생반응 촉매 및 보호층의 도입이 필수적이며 이를 통해 높은 광전압 및 안정성 확보가 요구된다.

　본 논문에서는 비스무트 바나데이트 및 실리콘을 우수한 특성을 갖는 광양극 물질로 응용하기 위하여 나노구조, 이종접합, 산소발생조촉매 등을 도입하였다. 비보조 광전기화학적 수전해를 위해 이종접합 나노구조 광전극과 태양전지로 구성된 탠덤 소자를 제작하여 태양광-수소 변환 효율을 평가하였다.

　첫번째 연구에서는, 비스무트 바나데이트의 전하분리효율을 극대화시키기 위하여 나노막대 형태의 하부층을 도입하였다. 비스무트 바나데이트의 최적화된 성장 시간으로 표면의 다공정 구조를 제어하였다. 하부층의 도입으로 인한 수직 구조의 광전극은 비표면적과 전하분리를 극대화하였으며, 산화텅스텐에 비해 산화주석이 더욱 효과적임을 다양한 분석을 통해 밝혔다. 산화주석이 도입된 비스무트 바나데이트 광전극은 이론 특성에 84%에 해당하는 $6.31\ mA\ cm^{-2}$ 의 아황산염 산화 광전류밀도를 $1.23\ V$ 에서 기록하였다. 니켈철 조촉매 도입 후 $5.61\ mA\ cm^{-2}$ 의 물 산화 광전류밀도를 $1.23\ V$ 에서 기록하였다. 광전극과 페로브스카이트/실리콘 태양전지를 결합한 탠덤 소자는 $5.90\ mA\ cm^{-2}$ 의 구동 전류를 기록해 약 7.3%의 태양광-수소 변환 효율을

달성하였다. 본 연구는 자발적 수전해를 위한 고효율 광전극을 디자인하는 전략들에 대해 제시하였다.

두번째 연구에서는 산화인듐이 비스무트 바나데이트와 계단식의 2 형 이종접합 밴드구조를 가짐을 최초로 밝혔다. 산화인듐은 비스무트 바나데이트의 전자수송층으로서 전하 분리 및 정공 차단의 역할을 효과적으로 수행한다. 또한 비스무트 바나데이트의 전착 사이클을 조절하여 산화인듐 위에 나노점 구조와 코어쉘 구조로 합성하였고, 광전기화학적 특성에 큰 영향을 끼치는 것을 확인하였다. 조촉매로서 도입한 탄닌-니켈철은 표면 반응 속도를 촉진시켜 7.1 mA cm^{-2} 의 아황산염 산화 광전류밀도 및 4.2 mA cm^{-2} 의 물 산화 광전류밀도를 1.23 V 에서 기록하였다. 광전극과 페로브스카이트/실리콘 태양전지를 결합한 탠덤 소자는 5.0 mA cm^{-2} 의 구동 전류를 기록해 약 6.2%의 태양광-수소 변환 효율을 달성하였다.

세번째 연구에서는 금속-부도체-반도체 이종접합을 통해 실리콘 광전극의 수전해 및 요소산화 특성을 향상시켰다. 화학적 식각법을 통해 실리콘 표면의 산화실리콘을 제어하였고, 광전기화학적 특성에 끼치는 영향을 밝혔다. 조성이 제어된 니켈철 합금 촉매를 도입하였고, 조성 조절된 니켈철의 광전기화학적 특성과 전기화학적 특성이 반대의 경향을 가짐을 보였다. 철의

204

도입에 따라 안정성과 특성이 트레이드오프 관계가 있음을 밝혔다. 최적화된

$Ni_{0.5}Fe_{0.5}/SiO_x/n\text{-}Si$ 광전극은 33.3 mA cm^{-2} 의 물 산화 광전류밀도를 1.23 V 에서

기록하였다. 수산화니켈 조촉매를 도입하여 개시전압을 더욱 감소시켰고,

페로브스카이트/실리콘 태양전지를 결합해 탠덤 소자를 제작하여 8.8 mA cm^{-2}

의 구동 전류와 약 11%의 태양광-수소 변환 효율을 달성하였다. 이종촉매가

도입된 $Ni(OH)_2/Ni_{0.5}Fe_{0.5}/SiO_x/n\text{-}Si$ 광전극은 요소 산화 반응에서도 향상된

특성을 보였다. 본 연구에서는 폐수 처리 관점에서 실리콘 기반 이종접합

광전극이 효과적으로 응용될 수 있음을 보였다.

본 박사학위 논문은 위의 연구 결과들을 통해 나노구조, 이종접합, 조촉매

도입이 비스무트 바나데이트 및 실리콘 광전극의 광·전기·화학적 특성을

효과적으로 향상시킬 수 있음을 보였다. 또한, 본 연구들을 통해 밝혀진

결과들은 자가작동 물분해 시스템 개발의 가능성 및 태양광 수소 변환 효율

극대화를 위한 방향을 제시하는 바이다.

키워드: 나노구조, 이종접합, 광전기화학적 수전해, 전기전착, 산소 발생 조촉매

학번: 2018-29728

성명: 양 진 욱